

Optical Alignment and Characterization  
of FIFI-LS - the Far-Infrared Field  
Imaging Line Spectrometer for SOFIA

and

Spitzer IRS Observations of Active  
Galaxies

DISSERTATION

der Fakultät für Physik der Ludwig-Maximilians-Universität München  
zur Erlangung des Grades  
Doktor der Naturwissenschaften  
Dr. rer. nat.

vorgelegt von

Mario Schweitzer  
aus Birkesdorf

München, März 2008

1. Gutachter: Prof. Dr. Reinhard Genzel
  2. Gutachter: Prof. Dr. Andreas Burkert
- Datum der Einreichung: 27.03.2008  
Datum der mündlichen Prüfung: 17.06.2008

# Contents

<b>1</b>	<b>Summary / Zusammenfassung</b>	<b>7</b>
<b>I</b>	<b>Optical Alignment and Characterization of FIFI LS</b>	<b>13</b>
<b>2</b>	<b>Introduction</b>	<b>15</b>
2.1	Far-Infrared Astronomy . . . . .	15
2.2	The Development of Airborne Astronomy . . . . .	16
2.3	The SOFIA Observatory . . . . .	17
<b>3</b>	<b>The Far-Infrared Spectrometer</b>	
	<b>FIFI-LS</b>	<b>19</b>
3.1	Concept and Specification . . . . .	19
3.2	Imaging 3D-Spectroscopy . . . . .	20
3.3	The Optical System . . . . .	21
3.3.1	The Entrance Optics . . . . .	22
3.3.2	The Image Slicer Unit . . . . .	25
3.3.3	The Exit Optics . . . . .	25
3.3.4	The Calibration Optics . . . . .	27
3.3.5	The Internal Calibration Source . . . . .	27
<b>4</b>	<b>Optical Alignment</b>	<b>39</b>
4.1	K-Mirror Alignment . . . . .	39
4.2	Long Wavelength Spectrometer Alignment . . . . .	41
4.2.1	Image Slicer Unit Alignment . . . . .	42
4.2.2	Spectrometer Optics Alignment . . . . .	43
4.2.3	Cold Test of the Optical Alignment . . . . .	47
<b>5</b>	<b>The Telescope Simulator</b>	<b>51</b>
5.1	Design and Alignment of the Telescope Simulator . . . . .	51
5.2	Preparation of the Telescope Simulator . . . . .	57
<b>6</b>	<b>Characterizing FIFI-LS</b>	<b>61</b>
6.1	Measuring the PSF . . . . .	61
6.2	The Spectral Calibration . . . . .	66
6.3	The Spectral Resolution . . . . .	67

<b>II</b>	<b>AGN Studies with the Spitzer Space Telescope</b>	<b>71</b>
<b>7</b>	<b>Introduction</b>	<b>73</b>
7.1	The Spitzer Space Telescope . . . . .	73
7.1.1	Instruments . . . . .	74
7.2	Active Galaxies . . . . .	75
7.2.1	The AGN Unification Model . . . . .	77
7.3	The QUEST Project . . . . .	79
7.4	Data Reduction Tools . . . . .	79
7.4.1	Removing Outlying Pixel Values . . . . .	80
7.4.2	Template Fitting . . . . .	81
<b>8</b>	<b>Silicate Emissions in Active Galaxies - From LINERs to QSOs</b>	<b>83</b>
8.1	Introduction . . . . .	84
8.2	Observations and Data Processing . . . . .	84
8.3	Results and Discussion . . . . .	85
<b>9</b>	<b>Extended Silicate Dust Emission in PG QSOs</b>	<b>91</b>
9.1	Introduction . . . . .	91
9.2	The PG QSO Sample . . . . .	93
9.2.1	Data Reduction . . . . .	93
9.3	Modeling the PG QSO IRS Spectra . . . . .	95
9.3.1	Model Components . . . . .	95
9.3.2	Fitting Procedure . . . . .	99
9.3.3	Cloud Distances and Covering Factors . . . . .	101
9.3.4	Fit Components and Uncertainties . . . . .	102
9.4	Results . . . . .	104
9.5	Discussion . . . . .	112
9.5.1	Dust Cloud Distances . . . . .	117
9.5.2	Covering Factors . . . . .	117
9.5.3	Silicate Emission and NLR Properties . . . . .	118
9.5.4	Silicate Emission from Torus Models . . . . .	119
9.6	Conclusions . . . . .	121
<b>10</b>	<b><i>Spitzer</i> Quasar and ULIRG Evolution Study (QUEST):</b>	
	<b>I. The Origin of the Far Infrared Continuum of QSOs</b>	<b>123</b>
10.1	Introduction . . . . .	124
10.2	The QUEST PG QSO Sample: Observations and Reduction . . .	126
10.2.1	The Sample . . . . .	126
10.2.2	Data Reduction and Line and Continuum Measurements .	127
10.3	Results . . . . .	129
10.3.1	PAH Emission is Common in QSOs . . . . .	129
10.3.2	Trends with Level of PAH Emission . . . . .	132
10.4	Discussion . . . . .	135
10.4.1	Nature of the QSO Far-Infrared Emission and the Starburst- AGN Connection . . . . .	135

---

10.4.2	Mid-infrared Diagnostics and the Starburst-AGN Connection in QSOs . . . . .	145
10.4.3	Direct AGN Heating of Cold Dust and PAHs ? . . . . .	148
10.4.4	Comparison to QSO Star Formation Estimates Based on [OII] . . . . .	149
10.4.5	Implications for High Redshift QSOs . . . . .	150
10.5	Conclusions . . . . .	151
<b>11</b>	<b>Conclusions</b>	<b>153</b>



# Chapter 1

## Summary / Zusammenfassung

The best platforms for astronomical observations in the mid- and far-infrared (FIR) wavelength regime are satellites which are used to collect scientific data from outside the Earth's atmosphere. Satellite observations are unaffected by the atmospheric absorption and emission which prevent FIR observations from the ground. Infrared space telescopes like IRAS (Infrared Astronomical Satellite) or ISO (Infrared Space Observatory) have been very successful missions in the past and have led to the development of even more powerful space observatories, like Spitzer (launched 2003) and Herschel (expected launch in late 2008). One disadvantage of space observatories is, however, in addition to the enormous technical and financial expenditure, that once the observatory is launched, there is no possibility to maintain or update the observatory with new technologies. In addition, the continuous loss of cryogenic liquids limits the operation time of infrared space observatories on the long term ( $\sim$ few years). Thus for follow up observations, alternative platforms are needed. Therefore an airborne observatory, where a powerful wide-bodied aircraft carries a telescope into the lower stratosphere, is an excellent extension to space observatories. Such a platform is the NASA/DLR funded project SOFIA (Stratospheric Observatory for Infrared Astronomy), expected to start its scientific operation in 2009.

The Max-Planck-Institute for Extraterrestrial Physics (MPE) has developed one of the two German scientific instruments for SOFIA, the Far-Infrared Field Imaging Line Spectrometer (FIFI-LS). This instrument allows one to acquire spectral and spatial information simultaneously. Due to its high sensitivity and observing efficiency, FIFI-LS will be used to investigate distant sources, e.g. ultra luminous infrared galaxies (ULIRGs), but it will also demonstrate its power as an imaging spectrometer for nearby extended sources. The concept of integral field spectroscopy in the FIR was implemented for the first time for FIFI-LS with an image slicer system based on mirror optics.

The first part of this thesis is related to FIFI-LS. In Chapter 2 the SOFIA observatory is introduced. Chapter 3 presents the optical mode of operation of FIFI-LS. As an outcome of this work the optical design of the internal calibration source is presented in Chapter 3. Chapter 4 presents the optical alignment of the long wavelength channel of FIFI-LS. To characterize the imaging and spectral properties of the instrument in the FIR a telescope simulator was developed in

the context of this thesis. A description of this instrument is given in Chapter 5. Finally Chapter 6 summarizes the characterization of FIFI-LS.

The second part of this work will present three publications related to MIR observations of active galaxies obtained with the Infrared Spectrograph (IRS) onboard of the Spitzer Space Telescope. The investigation of active galaxies in the entire waveband from the radio to the gamma-ray regime is a very active field of modern astronomy that aims at an understanding of the physics of the active galactic nucleus (AGN), its relation to star formation and the evolutionary picture of galaxies. In this context the mid-infrared wavelength range is especially important, because in this region one can find AGN as well as starburst tracers. This opens the possibility to disentangle the energy sources in active galaxies (AGN versus star formation) and to investigate the nuclear dust properties since the dust surrounding the central, bright accretion disk reprocesses the direct nuclear emission into thermal mid-infrared radiation. The Spitzer Space Telescope, with its broad mid-infrared wavelength coverage and excellent sensitivity, was able to detect - for the first time - silicate dust emission features in AGN, which were predicted by theory but could not be detected prior to Spitzer. The first two publications in the second part of this work are related to the silicate dust emission in AGN. Chapter 7 will give an introduction to the Spitzer Space Telescope and to active galaxies. The data reduction tools developed in the context of this thesis are also described in Chapter 7.

The first publication (Chapter 8) presents the first detection of silicate dust emission in a LINER (Low Ionization Nuclear Emission line Region galaxy) (NGC 3998) and discusses its dust properties. This chapter demonstrates that silicate emission does not only arise in the very luminous AGN (QSOs) as had been suggested by other authors.

The second publication (Chapter 9) discusses the origin of silicate emission detected in a sample of Palomar-Green Quasars (PG QSOs). Our findings are consistent with the silicate dust emission arising from the Narrow Line Region (NLR). This result places the dust clouds at distances that are large compared to the expectations from torus models.

The third publication (Chapter 10) presents the detection of PAH (Polycyclic Aromatic Hydrocarbons) features in PG QSOs. The strength of the PAH emission is an indicator for the rate of star formation. The detection of weak PAH features in luminous AGN is challenging, since the bright central AGN dominates the short wavelength MIR emission. Using the high sensitivity of Spitzer we were able to detect PAH emission in PG QSOs. The paper discusses the origin of the FIR emission in these sources by comparing a sample of starburst dominated ULIRGs with the PG QSO sample. This comparison leads to the conclusion that the starburst properties in both type of sources are very similar and that most of the FIR continuum emission in the PG QSOs is reprocessed star light from dust in the host galaxy. Additional support for this interpretation comes from an investigation of the correlation between the FIR continuum emission with starburst (e.g. PAHs) and AGN tracers (e.g. [OIV] line emission). It is important to understand the origin of the FIR continuum emission in active galaxies, since

the FIR continuum emission is often used to derive the star formation rate. A significant AGN contribution to the FIR emission would lead to a wrong estimate of the star formation rate. Another focus of the paper is the so-called AGN-Starburst connection which implies a correlation between the AGN and the starburst strength. Using mid-infrared starburst and AGN tracers we were able to show that such a connection exists for local PG QSOs.

Die besten Plattformen für astronomische Beobachtungen im mittel- und ferninfraroten Spektralbereich stellen zweifelsfrei satellitengestützte Teleskope dar, mit deren Hilfe über einen längeren Zeitraum außerhalb der Erdatmosphäre wissenschaftliche Daten gesammelt werden können. Solche Weltraumteleskope wurden in der Vergangenheit auch mehrfach mit Experimenten wie IRAS (Infrared Astronomical Satellite) und ISO (Infrared Space Observatory) realisiert, die sich als so erfolgreich herausstellten, dass sie zur Entwicklung noch aufwendigerer Nachfolgemissionen wie zum Beispiel Spitzer (gestartet 2003) oder Herschel (voraussichtlicher Start Ende 2008) führten. Ein Nachteil beim Betrieb eines Satellitenobservatoriums ist jedoch neben dem enormen technischen Aufwand der Umstand, daß ein einmal gestartetes Instrument von der Erde aus nicht mehr direkt erreichbar ist und damit weder gewartet noch durch den Einsatz modernerer Technologien aufgerüstet werden kann. Außerdem stellen solche Weltraumteleskope, wegen des ständigen Verlustes der zur Kühlung der Instrumente mitgeführten kryogenen Flüssigkeiten, immer zeitlich begrenzte Missionen dar, so daß man für Nachfolgeuntersuchungen oder sehr langfristige Beobachtungsreihen auf den Einsatz alternativer Beobachtungsplattformen angewiesen ist. Eine solche Plattform ist das von der amerikanischen Weltraumbehörde NASA in Zusammenarbeit mit dem deutschen DLR entwickelte Stratosphärenobservatorium SOFIA, das Ende 2009 seinen wissenschaftlichen Betrieb aufnehmen soll.

Für das SOFIA-Observatorium wurde am Max-Planck-Institut für extraterrestrische Physik (MPE) das abbildende Ferninfrarot-Spektrometer FIFI-LS entwickelt, mit dem es möglich sein wird, räumlich hochaufgelöste Abbildungen astronomischer Quellen bei gleichzeitiger spektraler Abtastung zu erstellen. FIFI-LS ist auf Grund seiner hohen Empfindlichkeit und Beobachtungseffizienz zur Beobachtung weit entfernter Quellen wie zum Beispiel ultraleuchtkräftiger Infrarotgalaxien (ULIRGs) geeignet, kann aber seine Stärken als abbildendes Spektrometer ebenso bei der Beobachtung von ausgedehnten oder nahe gelegenen astronomischen Quellen ausspielen. Mit FIFI-LS ist es erstmals gelungen das Konzept eines auf Spiegeloptiken basierenden Bildfeldzerlegers für den Ferninfrarotbereich einzusetzen, der die Integral-Feld-Spektroskopie ermöglicht.

Der erste Teil dieser Arbeit befasst sich mit FIFI-LS: In Kapitel 2 wird das SOFIA Observatorium vorgestellt, während Kapitel 3 eine Einführung in die optische Funktionsweise von FIFI-LS gibt. Als ein Ergebnis dieser Arbeit wird ebenfalls in Kapitel 3 die Entwicklung der internen Kalibrationsquelle von FIFI-LS beschrieben. Kapitel 4 präsentiert die Justierung der optischen Komponenten des langwelligen Spektrometerkanals von FIFI-LS. Um sowohl die abbildenden als auch die spektralen Eigenschaften des Gerätes im ferninfraroten Wellenlängenbereich testen zu können, wurde ein Teleskopsimulator im Rahmen dieser Arbeit entwickelt der in Kapitel 5 vorgestellt wird. Kapitel 6 beschreibt die Charakterisierung von FIFI-LS im ferninfraroten Wellenlängenbereich.

Der zweite Teil der Arbeit stellt drei wissenschaftliche Veröffentlichungen vor. Diese beschäftigen sich mit der Untersuchung aktiver Galaxien mit Hilfe des Infrarotspektrographen (IRS) an Bord des Weltraumteleskops Spitzer. Die Untersuchung aktiver Galaxien in allen möglichen Wellenlängenbereichen vom Radio bis in den Gammastrahlen-Bereich ist ein sehr aktives Gebiet der modernen Astronomie welches zum Ziel hat, die Physik der aktiven galaktischen Kerne (AGN), deren Beziehung zur Sternentstehung und die Galaxienevolution zu verstehen. In diesem Zusammenhang spielt der mittlere infrarote Wellenlängenbereich eine besondere Rolle, da sich hier sowohl Indikatoren für AGN als auch für die Sternentstehung befinden. Der mittlere infrarote Wellenlängenbereich erlaubt die Energiequellen in aktiven Galaxien zu entschlüsseln und die zentrale Staubverteilung zu untersuchen. Dies ist möglich, da der zirkumnukleare Staub die einfallende primäre AGN Strahlung in thermische Infrarotstrahlung konvertiert. Mit seiner hohen Empfindlichkeit und seiner guten Abdeckung des mittleren infraroten Wellenlängenbereiches ermöglichte das Spitzer Weltraumteleskop zum ersten Mal die Detektion von Silikatstaubemission in aktiven Galaxien. Theoretisch war diese Staubemission vorhergesagt worden, konnte allerdings mit frühere Missionen nicht nachgewiesen werden. Kapitel 7 gibt eine Übersicht über das Spitzer Weltraum Teleskop und eine Einführung in das Thema der aktiven Galaxien. Die Software, die zur Datenreduktion im Rahmen dieser Arbeit entstanden ist, wird ebenfalls in Kapitel 7 vorgestellt.

Die erste Veröffentlichung (Kapitel 8) beschreibt die erste Detektion von Silikatstaub in einem LINER (Low Ionization Nuclear Emission line Region galaxy) (NGC 3998) und diskutiert dessen Staubeigenschaften. Es wird gezeigt, dass Silikatemission nicht nur in sehr leuchtkräftigen Quasaren vorkommen kann, so wie von einigen Autoren zuvor vermutet, sondern auch in weniger leuchtkräftigen Quellen zu finden ist.

In der zweiten Veröffentlichung (Kapitel 9) wird die Herkunft der Silikatemission in Palomar-Green Quasaren (PG QSOs) diskutiert. Für diese Quellen wird gezeigt, dass sich die Silikatstaubemission mit einem Ursprung in der Narrow Line Region (NLR) erklären lässt. Dies platziert die silikat-emittierende Region weiter vom Zentrum entfernt als Torusmodelle nahe legen.

Die dritte Veröffentlichung (Kapitel 10) präsentiert die Detektion von PAH-Emission (Polycyclic Aromatic Hydrocarbons) in PG QSOs. Die Detektion von PAH-Emission in Quasaren, welche einen Indikator für die Sternentstehungsrate darstellt, ist recht schwierig, da der zentrale AGN den kurzwelligen MIR-Bereich dominiert und damit die PAH-Emission überstrahlt. Trotzdem ist es uns gelungen, mit Hilfe der hohen Empfindlichkeit von Spitzer PAH-Emission in PG QSOs nachzuweisen. Die Herkunft der Ferninfrarot-Emission in PG QSOs wird durch den Vergleich mit einer Anzahl von lokalen, sternbildungsdominierten ULIRGs behandelt. Dieser Vergleich führt zu der Schlussfolgerung, dass die Sternbildungseigenschaften in beiden Quelltypen sehr ähnlich sind und resultiert in der Interpretation, dass der Hauptteil der Ferninfrarot-Emission aus durch Staub reprozessiertem Sternenlicht besteht. Eine weitere Unterstützung hierfür findet sich in einer genaueren Korrelationsanalyse zwischen AGN- (z.B. [OIV] Linienemission) und Sternbildungsindikatoren (z.B. PAH-Emission). Die Ferninfrarot-

Emission kann dazu benutzt werden die Sternbildungsrate in entfernten Galaxien zu bestimmen. Daher ist es wichtig die Energiequellen dieser Strahlung in aktiven Galaxien zu identifizieren. Ein wesentlicher Beitrag des AGN zu der im fernen Infrarot abgestrahlten Energie würde zu einer falschen Bestimmung der Sternbildungsrate führen. Ein weiterer Fokus liegt auf der so genannten AGN-Starburst Verbindung. Damit ist ein gemeinsames Skalieren von AGN-Helligkeit und der Sternbildungsrate in aktiven Galaxien gemeint. Unter Benutzung der im MIR zugänglichen AGN- und Sternbildungsindikatoren ist es uns gelungen, eine solche Korrelation zwischen AGN und Sternbildung in lokalen PG QSOs nachzuweisen.

# Part I

## Optical Alignment and Characterization of FIFI LS



# Chapter 2

## Introduction

### 2.1 Far-Infrared Astronomy

The infrared wavelength region spans the range from 750 nm to about 400  $\mu\text{m}$ . This relative large range is traditionally subdivided into the near infrared (1-5  $\mu\text{m}$ ), the mid-infrared (5-30  $\mu\text{m}$ ) and the far-infrared (30-400  $\mu\text{m}$ ) regions. The spectral range between 750 nm and 1  $\mu\text{m}$  is sometimes called “*photographical*” infrared. This quite arbitrary subdivision has grown historically and reflects the historical development of infrared detectors. The FIR spectral range covers multiple emission lines, which are produced by fine-structure transitions or transitions between rotational or vibrational molecular states. The temperatures necessary to collisionally excite these states range typically from 30 to 1000K. The efficiency of the excitation depends strongly on the local gas density and gas temperature, which is why an investigation of the emission lines delivers important information about the physical conditions in the interstellar medium (ISM).

The strongest emission lines in the FIR (e.g. [OI] or the [CII]-fine structure line) are especially important, since they contribute efficiently to the radiative cooling of the interstellar gas. Observations of these lines are therefore fundamental to understand the heat transfer and temperature structure of the ISM. Detailed studies show that the [CII] (158  $\mu\text{m}$ ) and [OI] (63  $\mu\text{m}$ , 145  $\mu\text{m}$ ) lines are mainly excited in photo dissociation regions (PDR) by the FUV-flux (FUV: ultraviolet radiation with photon energies between 6 eV and 13.6 eV). These FIR lines can thus be used to measure the FUV-flux. Considering the interaction between the radiation and the ISM (radiative transfer) and a model for the line emission, it is possible to derive important information about the emitting region such as the electron temperature, the column density of the emitting gas, or the hydrogen/electron density. Besides line emission, the FIR continuum emission is also important, because the reprocessed stellar emission from dust in star forming regions within galaxies peaks in the FIR. The FIR is in general important to study cold objects (e.g. cold dust clouds) which have their maximum thermal emission at these wavelengths. Another advantage of the FIR wavelength range is that the extinction is greatly reduced with respect to shorter wavelengths. Therefore objects normally obscured within dense, dusty clouds can still be investigated. For example, star forming regions, with intrinsically high gas and dust column den-

sities, can be especially studied in the FIR. Instead it is more difficult to observe objects which are covered within dusty regions in the optical, near infrared and ultraviolet range of the electromagnetic spectrum due to the increased opacity. In addition there are powerful tracers of star formation (e.g. transitions of  $H_2$  in the UV) in these wavelength ranges, too. But due to the higher sensitivity with respect to extinction a good knowledge of the extinction is required to achieve a proper correction. For example, this is why optical star formation tracers like [OII] tend to underestimate the star formation rate in PG QSOs as discussed in Section 10.4.4.

One can find multiple wavelength regions in the near as well as in the mid-infrared which have high atmospheric transmission, so called windows. Within these windows ground-based observations are possible. In the FIR such transmission windows do not exist; the FIR is completely absorbed, mainly due to the broad band absorption of water vapor. Even from the most favorable ground locations (dry and at high altitudes) the absorption is practically hundred percent. Thus astronomical observations in this spectral region have to be obtained from the high layers of the atmosphere with balloons or airplanes or even better from space with satellites. Above the tropopause ( $\sim 10$ - $12$  km) one is located above  $\sim 99\%$  of atmospheric water vapor. The average expected transmission for an airborne observatory operating in the lower stratosphere ( $\sim 14$  km) in a wavelength range between  $30$ - $200 \mu\text{m}$  is  $60$ - $80\%$  although the remaining water vapor and other absorbing constituents of the atmosphere (mainly carbon dioxide) can still affect the observation or even make it impossible at certain wavelengths.

## 2.2 The Development of Airborne Astronomy

Airborne astronomy as well as infrared astronomy are both relatively young fields. This has been mainly due to the lack of suitable infrared detectors, which were not developed until the second half of the twentieth century. Up to the mid-60s balloon observatories or sometimes rockets were used for short observations in the mid- and far-infrared regions. The first airborne astronomical infrared mission was initiated by G.K. Kuiper (1965) on a Convair VV-990 plane. Using near infrared observations he was able to measure the water content of clouds in the atmosphere of Venus for the first time. In 1968 F. Low used a 30-cm telescope on a Learjet to measure the FIR luminosity of Jupiter and Saturn as well as that of multiple galactic and extragalactic sources. However both of these planes were not especially designed to carry out astronomical observations. The first plane that was designed as a dedicated astronomical platform for infrared observations was the Kuiper Airborne Observatory (KAO), that had its first flight in 1974. The plane was a Lockheed C-141 Star lifter that had a 91cm reflector mounted in the fuselage in front of the wings. With this plane observations at altitudes up to  $14000$  m were carried out. The last flight of the KAO was 1995, and it became the most successful airborne observatory so far. Now, 15 years later, SOFIA (Fig. 2.1) will constitute the next generation airborne observatory.



Figure 2.1: SOFIA (Stratospheric Observatory for Infrared Astronomy)

## 2.3 The SOFIA Observatory

The Stratospheric Observatory For Infrared Astronomy (SOFIA) will start its scientific work in late 2009, and will be the most powerful operating airborne observatory for infrared astronomy. SOFIA is a wide-bodied aircraft, Boeing 747 SP, which was modified to carry a 2.5m Nasmyth/Cassegrain telescope. Its primary mirror is much larger than that of the KAO, and will enable it to achieve an increased spatial resolution as well as an increased sensitivity. The telescope is mounted between the wings and the rear of the plane. A disadvantage of this mounting position might be that the telescope is located behind the engines, so that exhaust gases may contaminate the environment of the telescope. However, aerodynamical simulations have shown that astronomical observations will not be affected at all. Figure 2.2 shows the internal setup of the SOFIA.

The attitude control of a telescope on a moving platform is a big challenge and is critical for the telescope pointing. The SOFIA telescope is stabilized by its own inertia. The entire setup has a dumbbell-shaped design which is suspended on its center of gravity. Any remaining motions of the telescope are measured by high precision laser gyroscopes and corrected via active positioning elements. In addition two guider cameras (for the fine and gross field of view), provided by the telescope, are used to correct for an intrinsic gyroscope-drift. An additional guider camera provided by FIFI-LS is used to correct for an optical offset caused by the mechanical bending of the telescope structure. The maximum absolute position accuracy possible with such a setup is 1.5 arcsec. Table 2.1 summarizes the main parameters of the SOFIA telescope.

Nine instruments were selected as first light instruments for SOFIA, which are categorized in two classes. Facility-instruments are operated by the observatory and will be accessible permanently, while PI (Principal Investigator)-instruments are operated by external institutes under their own responsibility. There are

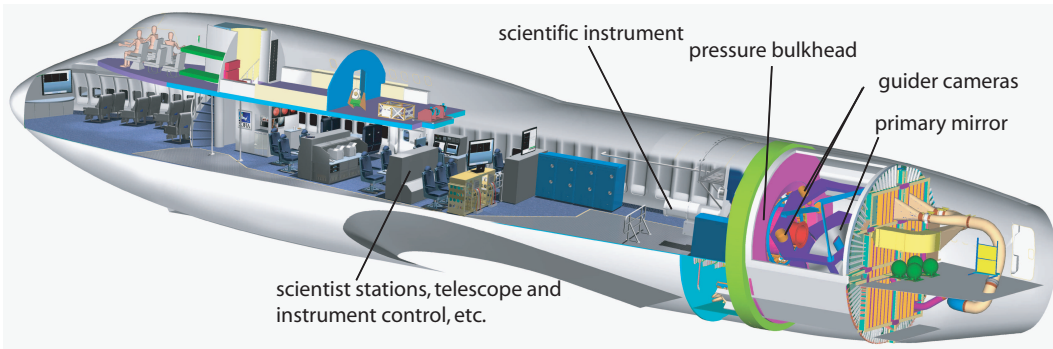


Figure 2.2: The SOFIA telescope has a Nasmyth-Cassegrain design with a primary mirror of 2.5 m in diameter. The telescope is stabilized by its own inertia. Remaining motions of the telescope are measured by high precision laser gyroscopes and corrected via active positioning elements. In addition two guider cameras are used to correct for an intrinsic gyroscope-drift. Behind the pressure bulkhead the scientific instrument is mounted onto the Nasmyth tube.

The SOFIA telescope	
type	Nasmyth/Cassegrain
primary mirror diameter	2.5 m
focal length	49140.9 mm
f-ratio	f/19.6
field of view	> 8 arcmin
spectral range	0.3 $\mu\text{m}$ - 1600 $\mu\text{m}$
elevation range	20-60 degree
Strehl-ratio	0.84
field of view curvature	415 mm

Table 2.1: The main parameters for the SOFIA telescope.

seven American instruments: the near-infrared camera FLITECAM (UCLA) and the mid-infrared camera FORCAST (Cornell University), the near infrared-photometer HIPO (Lowell Observatory) designed to observe star occultations as well as the mid-infrared spectrograph EXES (UT), the FIR-camera HAWC (University of Chicago), the submillimeter heterodyne-spectrometer CASIMIR (Caltech) and the submillimeter and FIR spectrometer SAFIRE (NASA/GSFC). The German contribution comprises two PI instruments: the heterodyne-spectrometer GREAT (MPIfR Bonn and University Cologne) as well as the FIR Field Imaging Line Spectrometer FIFI-LS (MPE Garching). The large number of different instruments, which range from broadband cameras to high resolution spectrometers and cover the large wavelength range from 5  $\mu\text{m}$  to about 650  $\mu\text{m}$ , will allow observations addressing a broad range of different astronomical topics. The data collected by SOFIA's instruments will make an important contribution to infrared-astronomy due to the high spectral and spatial resolution, as well as the high sensitivity, which was never reached before in this spectral range.

# Chapter 3

## The Far-Infrared Spectrometer FIFI-LS

### 3.1 Concept and Specification

The FIR Field Imaging Line Spectrometer (FIFI-LS) is one of the nine instruments which will operate as part of the first scientific flight campaigns of the airborne observatory SOFIA. It is an integral field spectrometer that allows one to simultaneously obtain both a two dimensional image of an astronomical object and spectral information for each spatial pixel (see Fig. 3.1). The instrument covers a wavelength range from 42 to 210  $\mu\text{m}$ .

The spectral information of different regions within the image of an astronomical object is a powerful tool to investigate the physical conditions in the astronomical source. The wavelength range of FIFI LS covers many important spectral features, e.g. atomic fine structure lines ([OI] 63 & 145  $\mu\text{m}$ , [OIII] 53 & 88  $\mu\text{m}$ , [NII] 122 & 205  $\mu\text{m}$ , [NIII] 57  $\mu\text{m}$ , [CII] 158  $\mu\text{m}$ ) or emission lines from molecules such as OH, H<sub>2</sub>O, CH, and CO and many other molecular species. This spectral information can be used to investigate e.g., the morphology of heating and cooling in nearby galaxies, the powering mechanism and ISM chemistry of ULIRGs or to investigate AGN where CO cooling lines, arising from a hot torus, are expected.

Due to the fact that there is no photoconductor material that allows the achievement of a good quantum efficiency over the entire wavelength range, the spectral range is split into two separate channels which can observe simultaneously: a short wavelength spectrometer (blue channel), with a wavelength range from 42 to 110  $\mu\text{m}$ , and a long wavelength spectrometer (red channel) covering the wavelength range from 110-210  $\mu\text{m}$ . The detector material is gallium doped germanium (Ge:Ga) and the single detector pixels of the red channel are mechanically stressed to adapt their wavelength sensitivity to the desired wavelength range. Due to this complication, the detector design is quite complex, and due to the extreme costs of the detector material, a  $25 \times 16$  pixel detector array was the largest realizable array size.

FIFI-LS uses aluminum mirrors as imaging components. Refractive elements can in principle be manufactured, but there is no existing antireflective coating

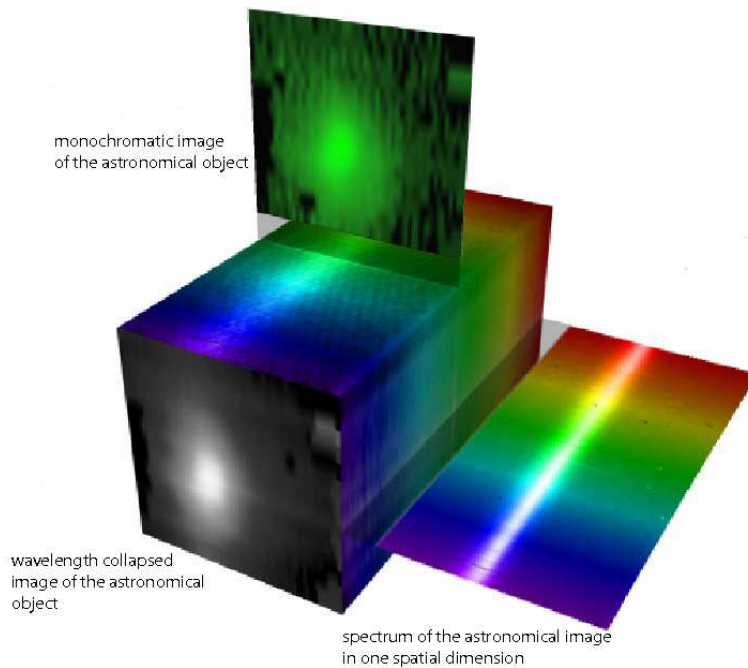


Figure 3.1: Schematic illustration of imaging 3D spectroscopy (integral field spectroscopy)

for the broad wavelength range of FIFI-LS. An advantage of using aluminum material for the mirrors as well as for the optical bench is that, when cooled down to working temperature (4 K), the entire optics contracts homologously so that the imaging properties do not change. Since FIFI-LS operates in the FIR the entire instrument has to be cooled to prevent the instrument itself from radiating in the FIR. The entrance optics are cooled to about 70 K using liquid nitrogen, while the spectrometer optics are cooled down to about 4 K using liquid helium. In addition the detectors are cooled to their working temperature of about 1.8 K using a separate cryostat and super fluid helium. The optical alignment described in Section 4 was carried out for the red channel and the entrance optics.

## 3.2 Imaging 3D-Spectroscopy

All spectrometers face the problem of projecting a three-dimensional information (2 spatial dimensions + 1 spectral dimension) onto a two-dimensional detector. Classical methods of spectroscopy, such as the slit-spectrometer or the Fabry-Perot spectrometer, solve this problem by reducing the number of simultaneously observed dimensions to two dimensions. These spectroscopic methods are quite often used, even if one dimension is missing, since they require a much less complex instrumental setup. By stepwise scanning across the third dimension they also allow one to obtain the full three-dimensional information. However, this scanning process requires a large number of single measurements depending on the spatial or spectral resolution. This often requires a time consuming process to obtain a full three-dimensional data cube, within which the atmospheric con-

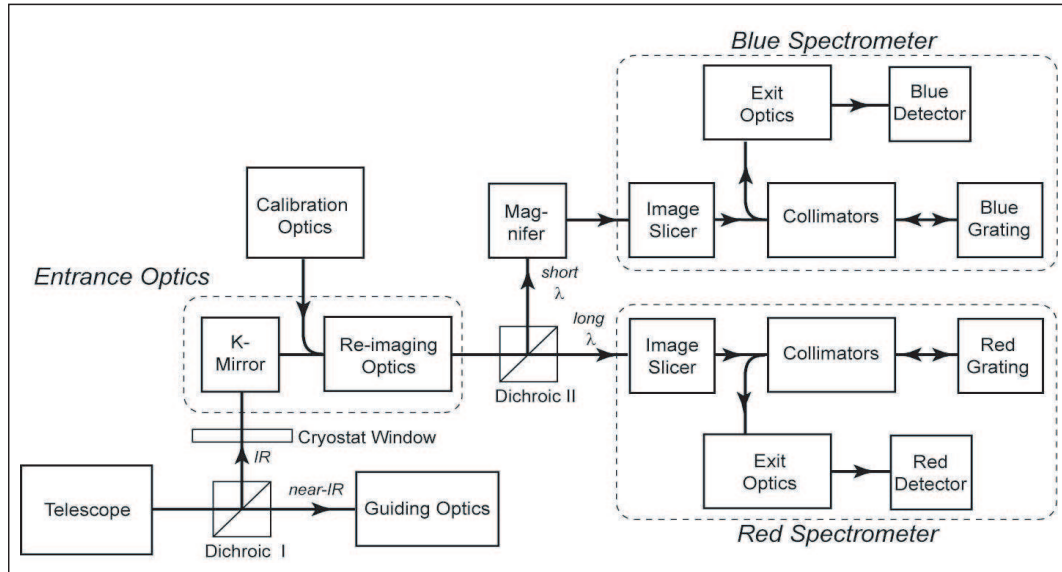


Figure 3.2: Schematic illustration of the entire optical system of FIFI-LS

ditions could change significantly. Another disadvantage of the slit-spectrometer is the error of the telescope pointing in the scanning mode, causing systematic errors in the measured data. These problems can be solved if the two-dimensional image can be rearranged into a one-dimensional so called pseudo-slit. This can be achieved with an image slicer unit. In FIFI-LS the image slicer unit consists of  $3 \times 5$  mirrors which decompose the original two-dimensional image into five slices and rearrange them to a pseudo-slit. The pseudo-slit can then be used as the entrance slit of a classical spectrometer. Using such a system, the second detector dimension can be used to record the spectral information, while the full two-dimensional spatial information is compressed into one dimension. This method allows one to acquire within a single measurement the entire three-dimensional data cube. Even if the atmospheric conditions change significantly during the measurement, a consistent dataset can be obtained. The absolute telescope pointing accuracy is not critical anymore, but rather its stability in time. This is because the exact a-priori position of the object within the field of view is of reduced importance.

### 3.3 The Optical System

The following section will introduce the overall optical system and explain specific components in further detail.

Figure 3.2 shows a diagram of the optical components of FIFI-LS. The first optical component in the optical path is a dichroic beam splitter, which reflects the infrared radiation at wavelengths longward of  $2 \mu\text{m}$  into the spectrometer. The visible and the near infrared part are transmitted towards the guiding camera system. The dichroic can be used to align the optical axis of FIFI-LS with respect to the telescope axis. The light, reflected into the spectrometer, passes through a polypropylene window into the evacuated cryostat. The entrance optics

consists of a field of view de-rotator (K-mirror) and a simple imaging optics to re-focus the beam. Another dichroic beam splitter separates the light into a short and a long wavelength part, which enter into the blue and the red spectrometer channels, respectively. The spectrometer setup of both channels is in principle identical. The only difference is an image magnification in the blue channel by a factor of 2, via the relay optics. At shorter wavelengths, the diffraction effects are smaller and thus the spatial resolution of the telescope is higher. This allows one to gain a factor of 2 for the spatial resolution in the blue channel. In the spectrometers the image is separated with the image slicer unit into five slices, and then rearranged along a line (the pseudo slit). To fit the gratings into the instrument it was necessary to manufacture them in a rectangular shape with a dimension of  $320 \times 85$  mm. This deviation from a quadratic shape in combination with the projection angle requires anamorphic optics, which collimates the beam with different magnifications along the main axes of the grating. Since the spectrometers work close to a Littrow-configuration, the dispersed infrared beam is reflected back through the same collimator system while the anamorphity is reversed. Finally, the focal plane is imaged via the anamorphic exit optics onto the detector array. To be able to internally calibrate the relative sensitivity of the single detectors (flat fielding) it is possible to illuminate the detectors homogeneously with chopped continuum radiation of a calibration source. This can be achieved by using a flip-mirror, imaging the exit of the calibration source onto the aperture pupil (Lyot-stop) of the system.

### 3.3.1 The Entrance Optics

The function of the entrance optics is to prepare the beam for the spectrometers. A K-mirror (see Fig. 4.1) serves as a field of view de-rotator to compensate for field rotation, which can be large especially for long integration times. The K-mirror consists of a prism-mirror (E1 and E3) and a flat mirror (E2) which are arranged such that a rotation by an angle  $\alpha$  of the K-mirror results in a rotation of  $2\alpha$  for the field of view. Its first mirror is located in the telescope focus. The second important duty of the entrance optics is to refocus the telescope beam with the proper magnification onto the first mirror stack of the image slicer unit. The magnification is chosen such that 1 pixel is equivalent to 12 arcsec for the red and 6 arcsec for the blue spectrometer. In addition, the entrance optics produces an image of the secondary mirror (pupil) of the telescope exactly at the position where the beam enters through the optical bench into the liquid helium cooled region. This pupil is the aperture pupil of the system (Lyot-stop) ensuring that only light rays emerging from the telescope within the proper solid angle enter the instrument. Finally, the entrance optics fold the optical path to fit into the available volume. This is achieved by the flat folding-mirrors E4 and E6, which, together with the imaging mirror E5, are the so-called periscope optics (see Fig. 3.3).

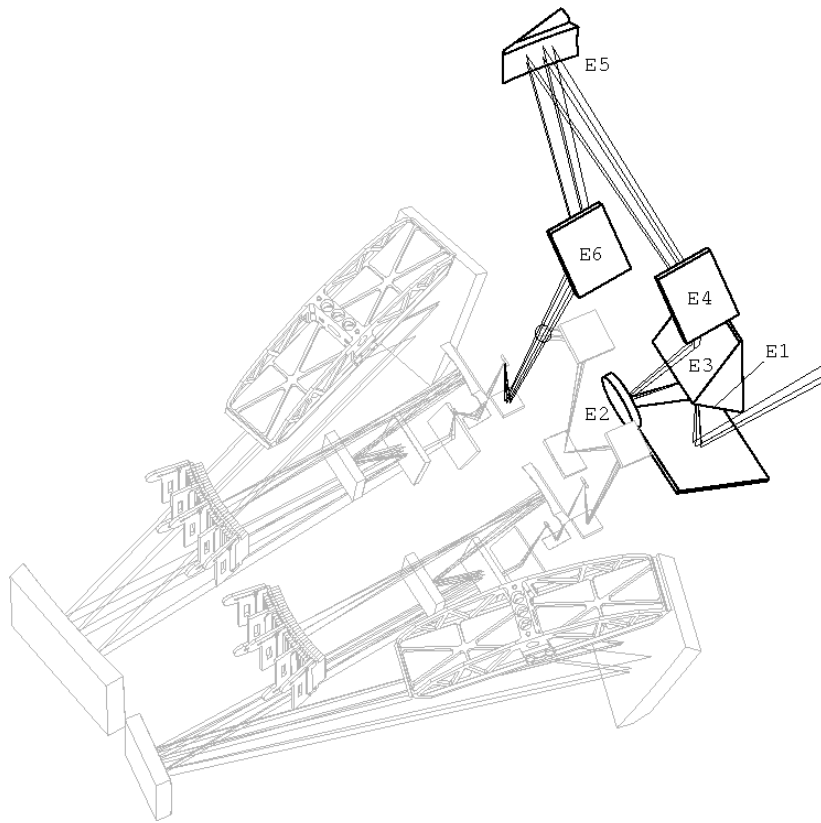


Figure 3.3: The entrance optics. E1-E3: K-mirror, E4 and E6: folding mirrors (flat), E5: imaging mirror (used to refocus the telescope beam)

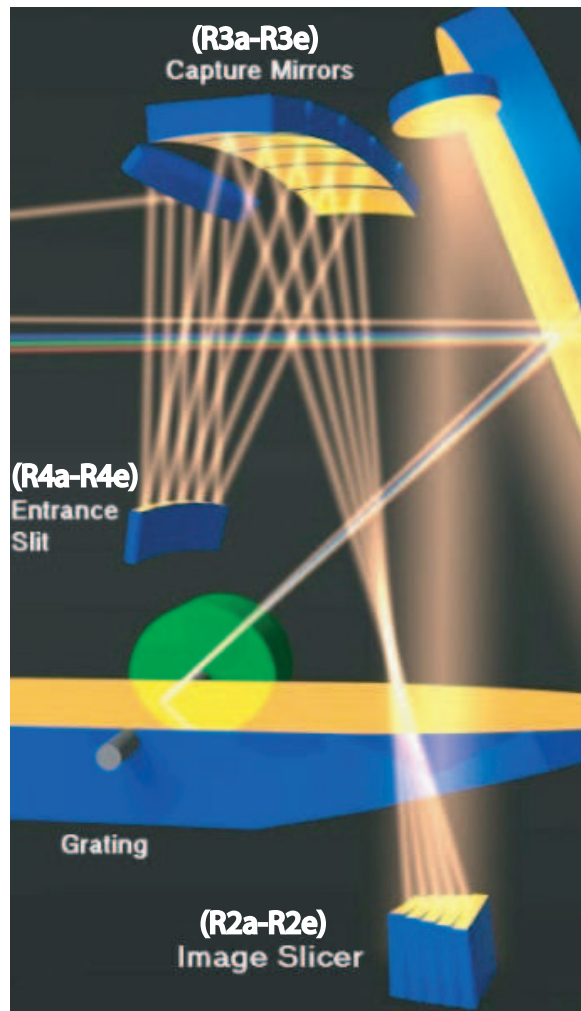


Figure 3.4: The image slicer unit rearranges the two-dimensional field of view into a quasi one-dimensional pseudo slit. It consists of five image slicer- (R2a-R2e), capture- (R3a-R3e) and entrance slit mirrors (R4a-R4e).

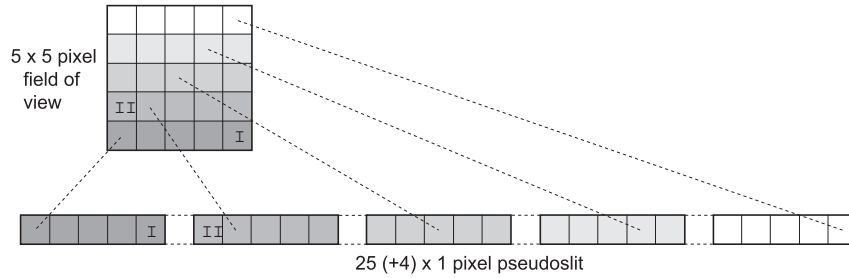


Figure 3.5: The image slicer concept: the two-dimensional field of view (5x5 pixel) is rearranged into a quasi one-dimensional pseudo slit. A gap of one pixel is left in-between the single slices to avoid any overlap.

### 3.3.2 The Image Slicer Unit

The function of the image slicer unit is to subdivide the two-dimensional image into five slices, and to rearrange them along a (quasi one-dimensional) pseudo slit. This rearrangement is achieved using a sequence of five slicer mirrors, capture mirrors and slit mirrors. The single slicer mirrors (configurations) (R2a-R2e ; B2a-B2e (see Fig.3.4 and 3.6)) are located in a focus of the instrument and are tilted with respect to each other. This setup fans out the beam spatially and separates the two-dimensional image into the five slices. An arrangement of five capture mirrors (R3a-R3e ; B3a-B3e) re-focuses the single slices approximately in a common plane and rearranges them along a line. Five slit mirrors (R4a-R4e; B4a-B4e) recombine the single pupils and produce a virtual image of this recombined pupil. The slices form now a single pseudo slit, that serves as the entrance slit for the grating spectrometer. The optical design of the image slicer is such that the slicer mirrors image the pupil into the center of the capture mirrors, which image the focal plane onto the slit mirrors. Slicer and slit mirrors are simple spherical mirrors, while the capture mirrors are of toroidal shape.

### 3.3.3 The Exit Optics

The dispersed image of the pseudo slit is projected via an anamorphic optics onto the detectors. In addition this optics produces an image of the pupil 240 mm in front of the detectors. This pupil image is important, since the detectors are designed such that they can only receive light emerging from the solid angle defined by this pupil. Light-cones in front of each detector pixel reflect the light emerging from wrong directions. Together with a mask, located in the pupil plane, this is a very efficient way to prevent ambient stray light falling onto the detectors. The exit optics in the two channels consist each of three imaging mirrors (R8-R10 and B8-B10). The magnification in the spectral direction is driven by the spectral resolution of the grating. The measured value for the spectral resolution of the long wavelength grating is 250 km/s at 160  $\mu\text{m}$  (Doppler velocity). The Nyquist-Sampling-Theorem demands for each resolution element two sample points, which leads to a magnification of 0.068  $\mu\text{m}$  per pixel. Since the detectors consists of 16 spectral pixels one observation with fixed grating angle equals a wavelength

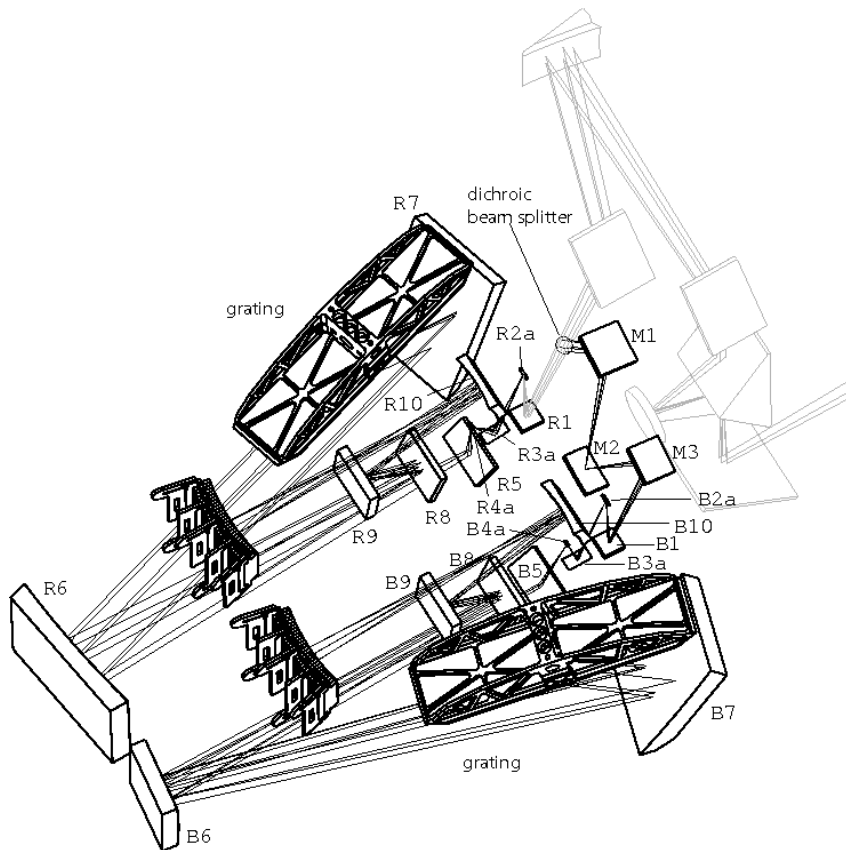


Figure 3.6: The spectrometer optics: The optical components of the blue (B) and red (R) spectrometer channels are shown. M1-M3 are the mirrors of the relay optics. B1 and R1 are flat mirrors, reflecting the beam into the slicer units. Each slicer unit (see also Fig. 3.4) consists of five slicer mirrors, capture mirrors and slit mirrors. Here just one of the five configurations is shown (B2a-B4a and R2a-R4a). B5 and R5 are flat mirrors reflecting the beam towards the collimator mirrors. B6, B7 and R6, R7 are the collimator mirrors, collimating the beam anamorphically onto the gratings. The mirrors B8-B10 and R8-R10 are the exit optics, imaging the dispersed pseudo slit onto the detectors.

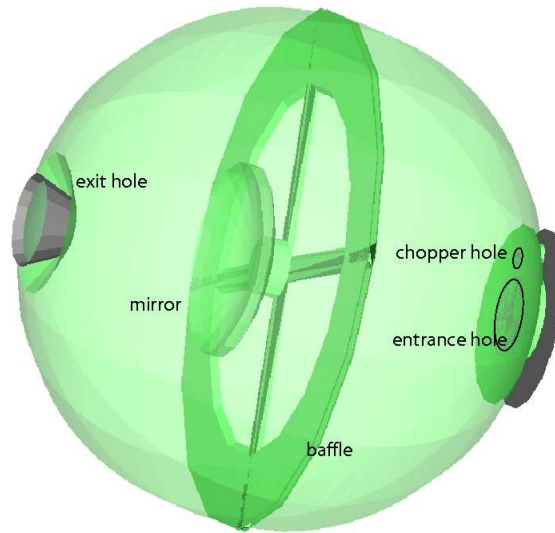


Figure 3.7: The internal calibration source

range of  $\sim 1 \mu\text{m}$ .

### 3.3.4 The Calibration Optics

Due to the very complex setup of the detectors, large differences for the absolute and relative spectral responsivity of the single pixels are expected. For this reason internal relative calibration of the detector response signals (flat fielding) is required. The internal calibration uses a continuum source that can be brought into the optical path by a flip mirror. This source can chop with a selectable frequency of a few hertz between two different continuum levels. These continuum levels are characterized by grey bodies of a certain temperature and emissivity. The parameters of the continuum source are selected such that the energy which is emitted into a certain frequency band per time is similar to the one emitted by the relatively warm telescope ( $\sim 15\%$  emissivity). Thus we can achieve a detector calibration at a background level which is typical for a real observation.

### 3.3.5 The Internal Calibration Source

A modified integrating sphere is used as the internal calibration source. A schematic drawing of this source is shown in Figure 3.7. The integrating sphere is a hollow sphere with a spark eroded, galvanically gold coated inner surface, which is thermally coupled to the liquid helium reservoir. Its rough inner surface produces diffuse scattering of the infrared light which is necessary to achieve a uniform illumination of the pupil of FIFI-LS. An internal spherical mirror in front of the exit hole inside the sphere prevents ambient light (from the outer parts of

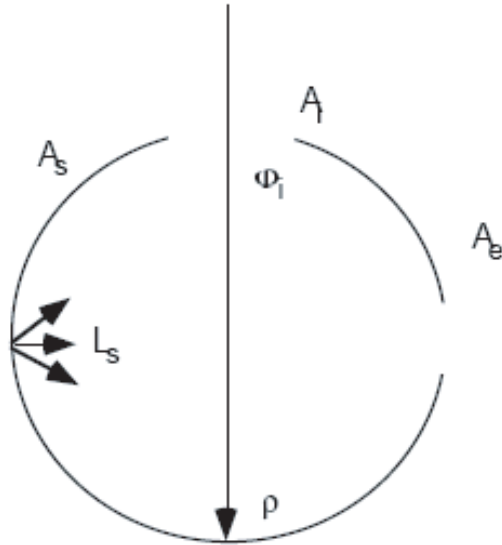


Figure 3.8: Integrating sphere concept

the source) from entering the sphere through the exit hole. An additional baffle ring prevents direct reflections out of the sphere. The sphere has three openings: so-called two entrance holes and one exit hole, the size of the latter one is 9 mm in diameter. The exit hole is imaged via a flip mirror to the position of the Lyot-stop. In front of the entrance holes, an infrared black painted aluminum radiator is located, serving as a black body radiator illuminating both holes simultaneously. A cooled aluminum finger is located between the smaller entrance hole and the radiator. By using electromagnets this finger oscillates with a selectable frequency of a few hertz and serves as a shutter. The smaller hole is a few percent of the size of the large entrance hole, and together with the cooled shutter it can produce a modulated signal in the frequency range of a few hertz. The background level, which is superimposed on this modulated signal, is determined by the size of the larger entrance hole. As explained above, the goal was to achieve a background level that is comparable to the expected background produced by the relatively warm SOFIA telescope. Since the expected emissivity for the SOFIA telescope is about  $\sim 15\%$ , this should also be the case for the internal calibration source in order to achieve the correct intensity at each wavelength. To meet this condition, a calculation was performed as well as a ray tracing simulation with the software package ZEMAX. The next subsections provide an introduction to the theory of integrating spheres and viewing factors, and explain how the desired size of the entrance hole was determined.

### The Integrating Sphere

The purpose of an integrating sphere is to spatially integrate radiant flux (see also [www.labsphere.com/tecdocs.aspx](http://www.labsphere.com/tecdocs.aspx)) and to produce a homogeneous exit radiation field. If light falls onto a diffuse surface it creates a “virtual” light source

by reflection. The light emanating from the surface is best described by its radiance, which is the flux density per unit solid angle. This quantity can be used to predict the amount of flux that can be collected by an optical system that views the illuminated surface. Although in our case the geometry is somewhat different due to the internal mirror and baffle, we introduce here the theory of a general integrating sphere and account for the difference later on by introducing a correction factor derived from the comparison to a ray tracing simulation. The expression for the radiance  $R$  (in units of  $\text{W}/\text{m}^2/\text{sr}$ ) of an ideal diffuse surface is given by

$$R = \frac{\phi_i \rho}{\pi A} \quad (3.1)$$

where  $\rho$  is the reflectance,  $A$  the illuminated area,  $\pi$  the total projected solid angle from the surface and  $\phi_i$  the input flux. The radiance equation for an integrating sphere must consider multiple surface reflections as well as losses through the port openings.

Consider a sphere with input port area  $A_i$  and exit port  $A_e$  (see Fig. 3.8). One can show that the fraction of radiant flux received by a surface element of the sphere is equal to the fractional surface area it consumes within the sphere. By the initial reflection the input flux will be perfectly diffused so that the amount of flux incident on the entire sphere surface is

$$\phi_{s1} = \phi_i \rho \left( \frac{A_s - A_i - A_e}{A_s} \right). \quad (3.2)$$

For simplicity we define the port fraction  $f$  as  $f = \frac{A_i + A_e}{A_s}$  so that the quantity in parentheses can be written as  $(1-f)$ . The amount of flux incident on the total sphere surface after the second reflection is

$$\phi_{s2} = \phi_i \rho^2 (1-f)^2 \quad (3.3)$$

and so on. After  $n$  reflections the total flux over the entire integrating sphere surface is

$$\phi_s = \phi_i \rho (1-f) (1 + \rho(1-f) + \dots + \rho^{n-1} (1-f)^{n-1}). \quad (3.4)$$

If we expand this to an infinite power series, this reduces to

$$\phi_s = \frac{\phi_i \rho (1-f)}{1 - \rho(1-f)}. \quad (3.5)$$

This equation indicates that the total incident flux on the sphere surface is higher than the input flux due to multiple reflections inside the sphere. From Equation 3.5 it follows that the sphere surface radiance can be written as

$$R_s = \frac{\phi_i}{\pi A_s (1-f)} \cdot \frac{\rho(1-f)}{1 - \rho(1-f)} \quad (3.6)$$

$$= \frac{\phi_i}{\pi A_s} \cdot \frac{\rho}{1 - \rho(1-f)}. \quad (3.7)$$

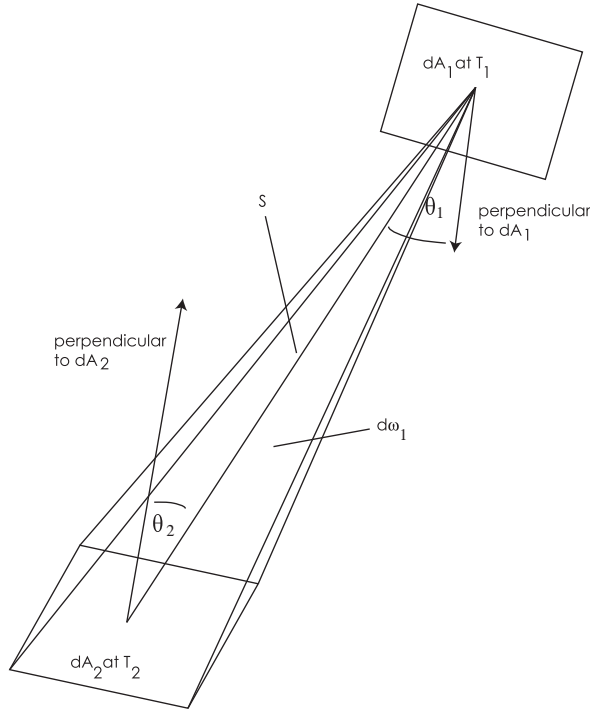


Figure 3.9: Radiation exchange between two black body surfaces.

This final equation can be used to determine the radiance of the integrating sphere for a given sphere diameter, reflectance and port fraction. We still have to identify the incident flux  $\phi_i$ .

The determination of  $\phi_i$  is a geometrical problem. In our case we have a rectangular black body emitter in front of a circular entrance hole. The black body can be considered as a Lambertian source. The surface brightness of a Lambertian radiator does not change when observed from different inclinations. Its radiance ( $\text{W}/\text{m}^2/\text{sr}$ ) is independent of viewing angle.

To describe the radiant energy exchange between surfaces so-called viewing factors are used. In general the viewing factor describes how much energy is exchanged between a configuration of radiating surfaces, in dependence on their shape and relative orientation (see also Siegel et al. 2002).

### The Viewing Factor

Consider two differential surface elements as seen in Figure 3.9. The elements  $dA_1$  and  $dA_2$  are isothermal and are at temperatures  $T_1$  and  $T_2$ . They are oriented arbitrarily in space and their surface normal vectors have the angles  $\theta_1$  and  $\theta_2$  with respect to their direct connection line  $S$ . The total energy received from  $dA_1$  per unit time at  $dA_2$  is

$$d^2\phi_{d1-d2} = R_{s,1}dA_1 \cos\theta_1 d\omega_1, \quad (3.8)$$

where  $d\omega_1$  is the solid angle under which  $dA_2$  appears from the position of  $dA_1$ .  $R_{s,1}$  is the radiance of surface  $dA_1$  and  $d\omega_1$  can be written as

$$d\omega_1 = \frac{dA_2 \cos \theta_2}{S^2}. \quad (3.9)$$

Together with Equation 3.8 it follows

$$d^2\phi_{d1-d2} = \frac{R_{s,1}dA_1 \cos \theta_1 dA_2 \cos \theta_2}{S^2} \quad (3.10)$$

and in analogy

$$d^2\phi_{d2-d1} = \frac{R_{s,2}dA_2 \cos \theta_2 dA_1 \cos \theta_1}{S^2}. \quad (3.11)$$

Following the Stefan-Boltzmann law the radiance of a black body radiator can be written as

$$R_s = \frac{\sigma T^4}{\pi}. \quad (3.12)$$

Together with Equation 3.12 and the definition of the viewing factor as the fraction of energy emitted by  $dA_1$  and received by  $dA_2$  per time, normalized to the total emitted energy of  $dA_1$  per time, the differential viewing factor can be written as

$$dF_{d1-d2} = \frac{d^2\phi_{d1-d2}}{\sigma T_1^4 dA_1} = \frac{\sigma T_1^4 ((\cos \theta_1 \cos \theta_2)/(\pi S^2)) dA_1 dA_2}{\sigma T_1^4 dA_1} = \frac{\cos \theta_1 \cos \theta_2}{\pi S^2} dA_2. \quad (3.13)$$

Now we want to know the viewing factor for the energy exchange between two finite surfaces  $A_1$  and  $A_2$ . Equation 3.10 can be expressed as

$$d^2\phi_{d1-d2} = \sigma T_1^4 \frac{\cos \theta_1 \cos \theta_2}{\pi S^2} dA_1 dA_2. \quad (3.14)$$

If this expression is integrated over  $A_1$  and  $A_2$ , the energy emitted from  $A_1$  to  $A_2$  is obtained. For the viewing factor it follows

$$F_{1-2} = \frac{\int_{A_1} \int_{A_2} (\sigma T_1^4 \cos \theta_1 \cos \theta_2 / (\pi S^2)) dA_2 dA_1}{\sigma T_1^4 A_1} = \frac{1}{A_1} \int_{A_1} \int_{A_2} \frac{\cos \theta_1 \cos \theta_2}{\pi S^2} dA_2 dA_1. \quad (3.15)$$

We can express this term by using differential viewing factors as follows

$$F_{1-2} = \frac{1}{A_1} \int_{A_1} \int_{A_2} dF_{d1-d2} dA_1 = \frac{1}{A_1} \int_{A_1} F_{d1-2} dA_1. \quad (3.16)$$

For many typical geometries one can find solutions in the literature. In particular, a solution was found for the case of an emitting, differential surface element in front of a circular absorber. Figure 3.10 demonstrates this geometrical setup, while Equation 3.17 gives the corresponding viewing factor which has to be integrated over the rectangular shape of our black body radiator in front of the entrance hole,

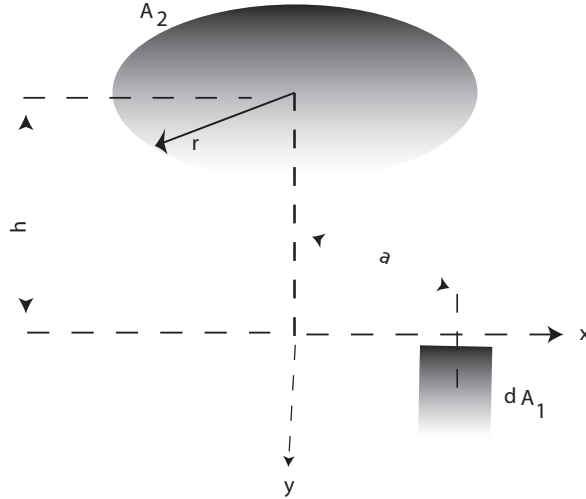


Figure 3.10: Circular surface in front of a differential surface element.

$$F_{d1-2} = \frac{1}{2} \left( 1 - \frac{Z - 2R^2}{\sqrt{Z^2 - 4R^2}} \right). \quad (3.17)$$

In this equation the following definitions were assumed :  $H = h/a$  ,  $R = r/a$  and  $Z = 1 + R^2 + H^2$  (compare also with Fig. 3.10). In addition, we define the distance  $a$  to the differential surface element by  $a^2 = x^2 + y^2$ , where  $x$  and  $y$  are oriented along the two axes of our rectangular black body. The origin of the coordinate system spanned by  $x$  and  $y$  is located on the surface normal of  $A_2$  which intersects the center of  $A_2$ . According to Equation 3.16 we can write

$$F_{1-2}^{sphere}(r) = \frac{1}{2A_1} \int \int \left( 1 - \frac{1 + \frac{h^2 - r^2}{x^2 + y^2}}{\sqrt{\left(1 + \frac{h^2 + r^2}{x^2 + y^2}\right)^2 - 4\frac{r^2}{x^2 + y^2}}} \right) dx dy. \quad (3.18)$$

This double integral was solved numerically using Mathcad taking into account the geometry of our setup. The dimensions of the black body radiator are  $A_{BB} := A_1 = 16 \times 20 \text{ mm}^2$  while its surface is located 3 mm apart ( $h=3 \text{ mm}$ ) from the entrance hole. Now we can calculate the sphere emissivity  $\epsilon$  from the following, the emissivity defining expression. Taking Equation 3.12 into account it follows

$$\frac{F_{1-2}^{sphere}(r) \sigma A_{BB} T_{BB}^4}{\pi A_s} \frac{\rho}{1 - \rho(1 - f(r))} = \epsilon \cdot \frac{\sigma T_{BB}^4}{\pi} \quad (3.19)$$

thus

$$\epsilon = \frac{F_{1-2}^{sphere}(r) A_{BB} \rho}{A_s (1 - \rho(1 - f(r)))}. \quad (3.20)$$

This is the emissivity of the sphere, which still depends on the entrance opening radius  $r$ .

The reflectivity  $\rho$  for the rough internal sphere surface was adopted from calorimetric measurements of the calibration source of the PACS instrument.

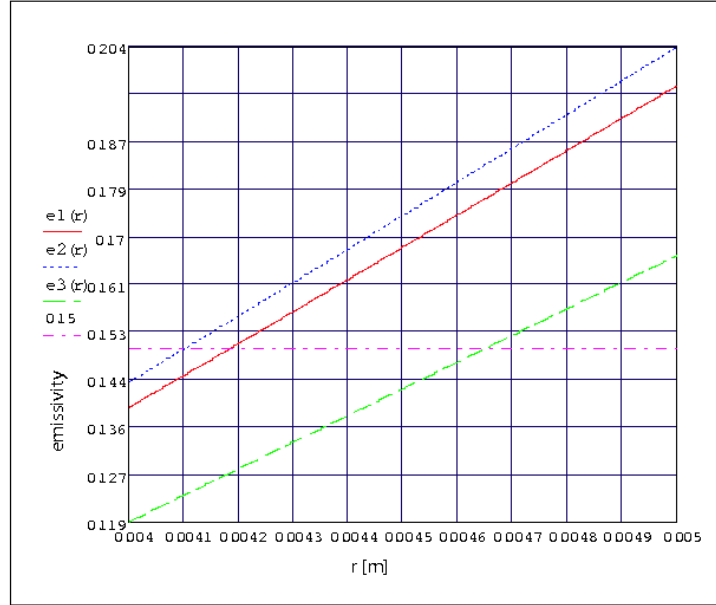


Figure 3.11: The integrating sphere emissivity for different distances (blue: 2.5 mm, red: 3 mm, green: 5mm) between black body and entrance hole plotted versus the entrance hole radius. The horizontal line indicates an emissivity of 15%.

PACS was built at MPE and is one of the scientific instruments for the Herschel satellite. It was found that  $\rho \sim 99.0\%$ . The radius  $r$  was varied in order to reach the required emissivity of 15%. In Figure 3.11 the emissivity is plotted for different distances  $h$  and different entrance hole radii  $r$ . The horizontal line indicates an emissivity of 15%. One can see that for a distance  $h=3$  mm (red curve), the required emissivity is achieved with an entrance hole radius of about  $r=4.2$  mm. The comparison to an estimation of the emissivity from a ray tracing simulation of the integrating sphere showed that the “simulated” emissivity is about a factor 0.66 lower than expected from the theoretical calculation taking also a larger inner surface into account (due to the internal mirror and baffle).

This difference can be explained by the additional inner components of our calibration source compared to a perfect integrating sphere and in particular by the spherical mirror in front of the exit hole. The simulations assume a scattering factor of 70%, which implies that about 30% of the light is directly reflected. Due to the particular shape and position of the mirror light falling into the sphere is suppressed by reflecting it out again, and at the same time the mirror reduces the emerging light by not allowing direct reflections out of the sphere. Including a correction factor of  $k=0.66$  for the emissivity, the theoretical and the simulated emissivity are consistent. However, the real emissivity depends strongly on the scattering factor. To be able to change the emissivity of the source the entrance hole is manufactured as a set-in; it can be replaced by another opening with different size. The final design parameters are listed in Table 3.1

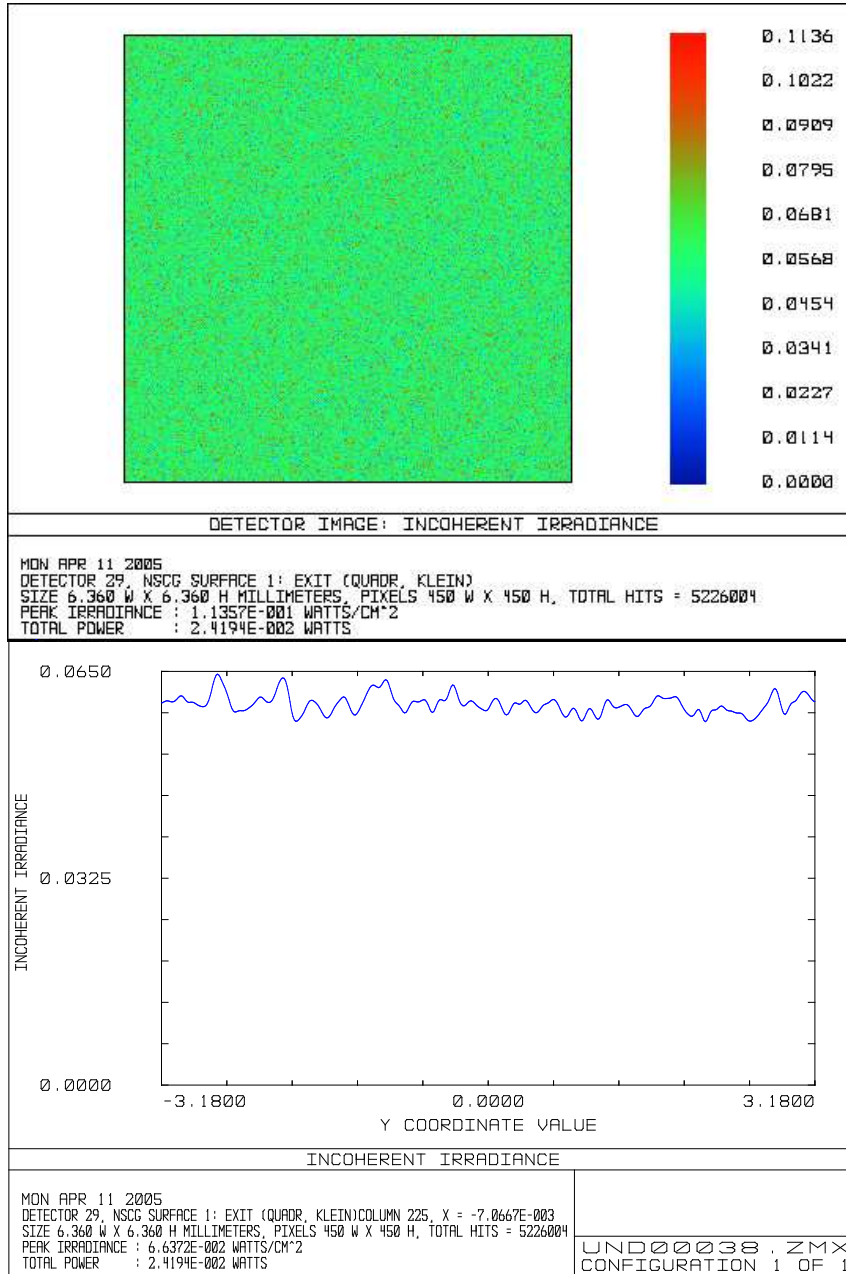


Figure 3.12: ZEMAX simulation of the homogeneously illuminated pupil (averaged over the angle of incidence).

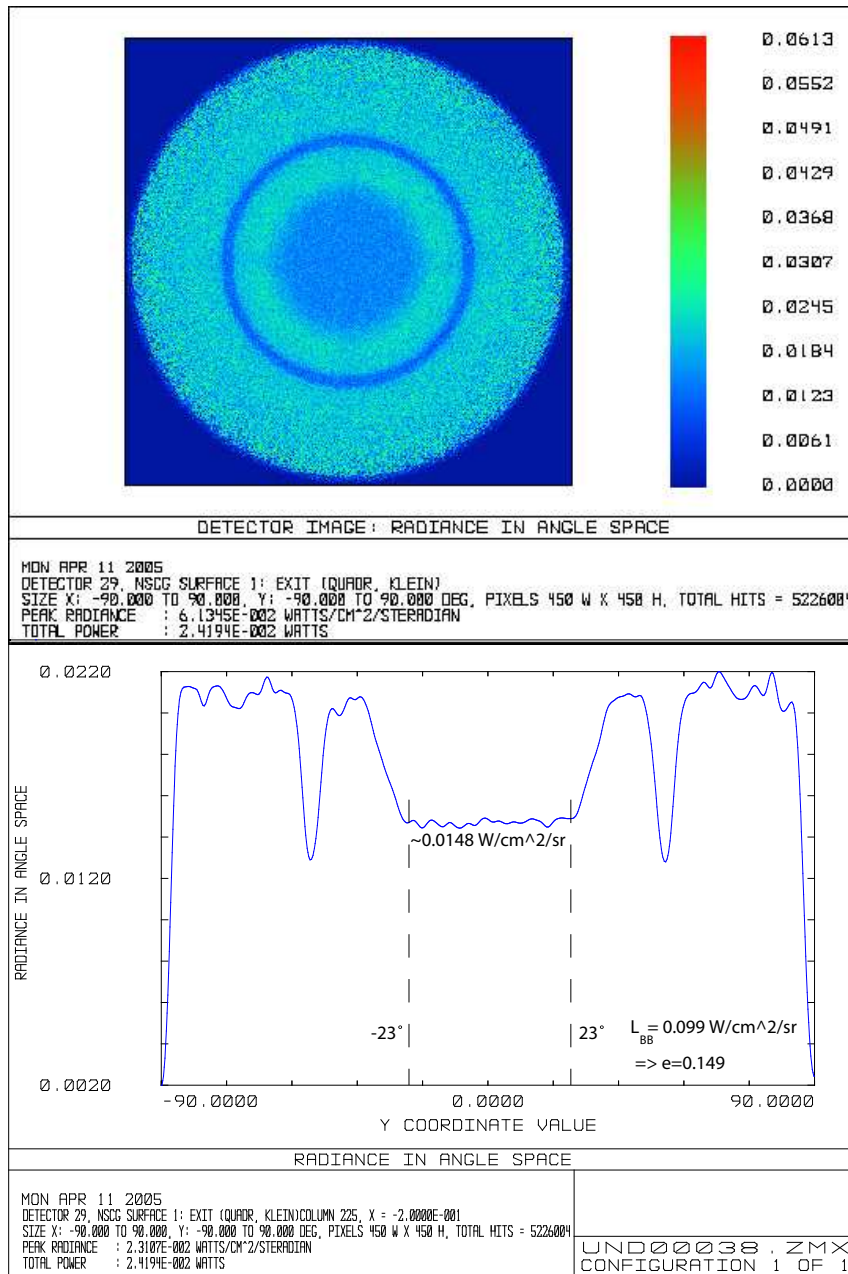


Figure 3.13: ZEMAX simulation of the pupil radiance in angle space (averaged over the entire pupil). The radiance of the simulated black body was  $0.099 \text{ W/cm}^2/\text{sr}$ , thus the resulting emissivity is  $\epsilon = 0.149$ . The maximum viewing angle of FIFI-LS is  $15.2^\circ$ . Within this range the radiance is isotrop.

property	value
$A_{BB}$	$0.016 \times 0.02 \text{ m}^2$
h	0.003 m
r	0.0066 m
$A_s$ (sphere+mirror+holding structure)	0.029 m <sup>2</sup>
$\rho$	99 %
$r_{exit}$	0.0045 m
$r_{chopper}$	0.0015 m
$\epsilon$	0.149

Table 3.1: Final (design) parameters for the internal calibration source.

In the following figures the results of the ray tracing simulation are shown. Figure 3.12 illustrates the homogeneously illuminated pupil plane. In Figure 3.13, the radiance is plotted in angle space. One can see that the radiance is lower in the central region ( $\pm 23^\circ$ ) due to the internal mirror. Figure 3.13, also shows the isotropic distribution of the radiance in the central region. Since the angle space covered by the beam of FIFI-LS is smaller than this region (maximum viewing angle =  $15.2^\circ$ ), the calibration source can be considered a Lambertian source. This implies that the radiance is angle independent within this angle space. Since the radiance in Figure 3.13 is averaged over the entire pupil it has also been verified that the radiance and its isotropy do not change for different positions within the pupil. Using the internal calibration source we can illuminate the grating and detector plane homogeneously and perform a detector calibration with a background level comparable to that produced by the SOFIA telescope. A picture of the internal calibration source is shown in Figure 3.14.

Within the scope of this thesis, ray tracing simulations were used in addition to design a mirror that brings the exit of the internal calibration source into the optical path of FIFI-LS. It was found that the required shape of this mirror is an off axis hyperboloid. The mirror is mounted onto a mechanism that can move it into the optical path and it is designed such that it images the exit hole of the calibration source onto the Lyot-stop pupil of FIFI-LS. In this way a homogeneous illumination of the detector array is achieved. In Figure 3.15 the result of an optical test of this mirror is shown. The Lyot-stop pupil is imaged backwards onto the position of the exit hole of the internal calibration source (at optical wavelengths). It was found that the mirror produces an image at the desired position with the proper magnification.



Figure 3.14: The calibration source. In the lower picture one can see the internal spherical mirror located in front of the exit hole and the baffle ring to prevent direct reflections out of the sphere.

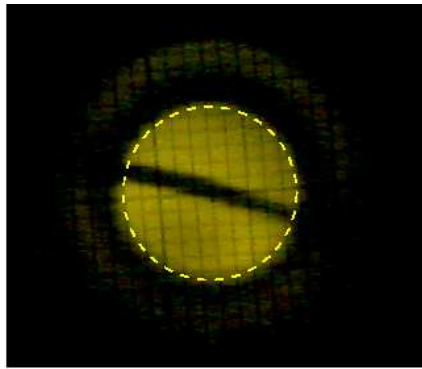


Figure 3.15: A test of the flip mirror. The optical image of the Lyot-stop was projected back onto the entrance hole of the internal calibration source in order to test the imaging properties and the alignment of the flip-mirror. The image was located at the expected position and the expected magnification indicated by the yellow circle was achieved. The black line across the image is a piece of wire at the Lyot-stop, that was imaged back to the entrance hole of the calibration source.

# Chapter 4

## Optical Alignment

FIFI-LS has several types of optical components, most of which being mirrors of different shapes and sizes. The red channel and the entrance optics include 28 mirrors while the blue spectrometer channel plus relay optics consist of 25 mirrors. In total, FIFI-LS has 53 single mirrors.

None of the optical components in FIFI-LS have alignment mechanisms. All components are fixed to their positions using fit pins. The only way to correct a possible misalignment is to shim the mirrors with layers of a thin aluminum foil, and if necessary to remove the fit pins. Mistakes made in the manufacturing process of parts (holders, mirrors), and lower manufacturing precisions than desired contribute to the total misalignment. Since the whole system will be cooled down to a few Kelvin in operation, it is also necessary to verify that the alignment is stable at these temperatures. This was tested in the optical as well as in the far-infrared using a telescope simulator that will be introduced in the next section.

The following list shows the steps which have been undertaken as part of this thesis to align the optical system:

- Mirror Tests
- K-mirror Alignment
- Image Slicer Unit Alignment
- Spectrometer Optics Alignment
- Cold Test of the Optical Alignment
- Alignment of K-mirror and Entrance Optics with respect to the Spectrometer
- FIR Performance Verification of FIFI-LS using the Telescope Simulator

### 4.1 K-Mirror Alignment

The function of the K-mirror is to de-rotate the field of view, which would otherwise rotate due to the change of source elevation and azimuth along the flight

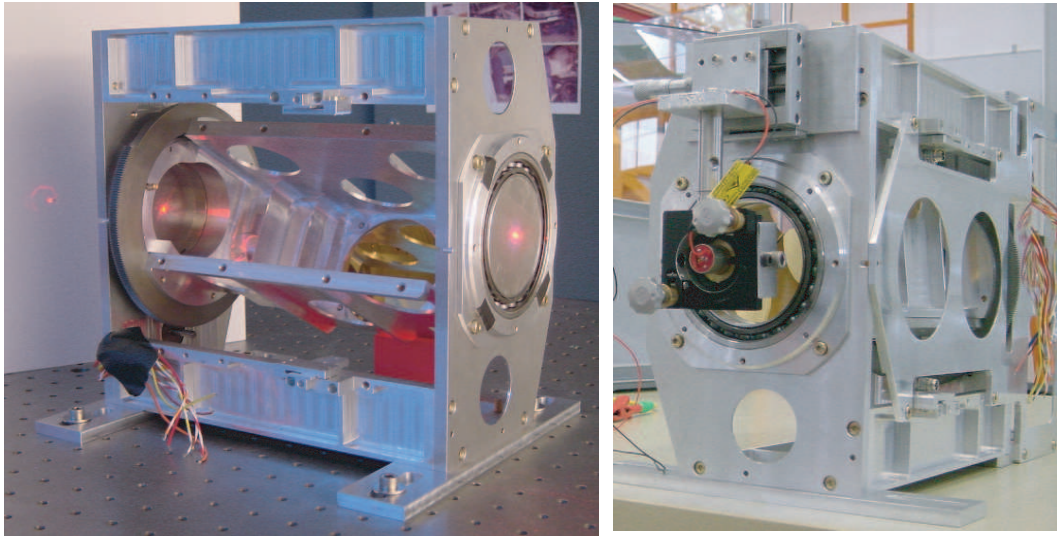


Figure 4.1: The K-mirror. Left: the pinhole masks are used to align the laser onto the rotational axis of the system. The prism mirror was taken out. Right: mounting of the alignment laser onto the K-mirror housing.

path of the aircraft (non-polar telescope mount). The K-mirror system is the first optical component within the cryostat, and consists of a prism mirror and a flat mirror located above the prism mirror. In Figure 4.1, the K-mirror system is shown.

The mirror system is mounted onto an aluminum structure that is fixed via ball bearings into the outer housing. The entire system is mounted with the outer housing onto the nitrogen cooled plate, where it is part of the entrance optics. By observing reference stars with the guider camera system in the optical, the desired rotational correction is measured and translated into a command that moves the K-mirror via a stepper motor to its new position.

The first alignment step is to align the K-mirror itself to ensure that the image rotates around the center of the field of view, without any superposed epicyclic motion. A misalignment can result in a movement of the image behind the K-mirror which would cause the image to be offset from its desired center position on the detector. This offset depends furthermore on the distance to the K-mirror. It is necessary to measure the beam position at different distances from the K-mirror while it rotates. To test the K-mirror performance an alignment laser was used which was mounted on the outer housing of the K-mirror (see Fig. 4.1). Two high precision translation stages were used to fine tune the position of the alignment laser, and two high precision rotational stages to tune the orientation. In addition, two thin circular aluminum masks with pinholes at their centers were used at the entrance and exit of the K-mirror to facilitate the definition of the rotational axis of the system.

If the system is aligned perfectly there is one laser position/orientation where the transmitted beam does not move at all if the K-mirror rotates. This is exactly the axis of rotation/symmetry. This has to be tested for at least two different distances from the K-mirror. In Figure 4.2, the laser spot at 70 and 570 cm

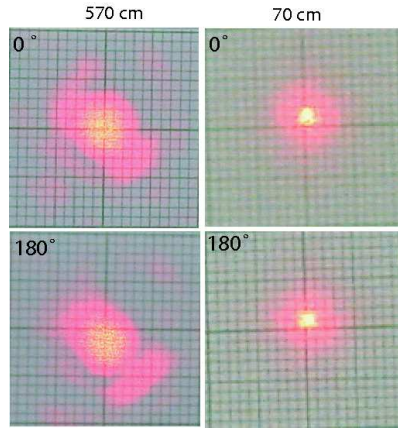


Figure 4.2: K-mirror alignment test. The laser was aligned with respect to the rotational axis of the K-mirror. The position of the laser spot was measured for a rotation of  $0^\circ$  and  $180^\circ$  at 70 and 570 cm behind the K-mirror. The spot position is very stable indicating a good internal alignment of the K-mirror.

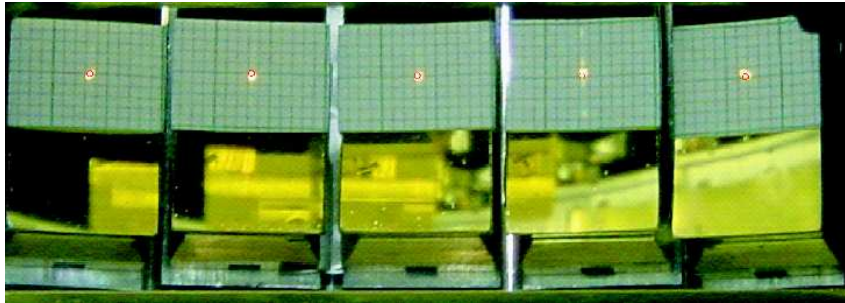


Figure 4.3: Images of the Lyot-stop pinhole centered on the capture mirrors. The single images were centered by aligning the slicer mirrors. The red circles indicate the center of the capture mirrors.

behind the K-mirror is shown after the K-mirror was aligned. The upper and lower images are separated by a K-mirror rotation of  $180^\circ$ . The K-mirror is aligned well, since the laser spot is stable over the full rotation. At 570 cm from the K-mirror, the spot moves about 1.5 mm in the vertical direction, which is less than 1% of the pupil size and can therefore be neglected.

## 4.2 Long Wavelength Spectrometer Alignment

The next step was the alignment of the red spectrometer channel. This was achieved with a stepwise procedure since the system consists of multiple components. The first component in the optical path of the spectrometer optics is the image slicer, next follow the two collimators, the grating, and finally the exit optics.

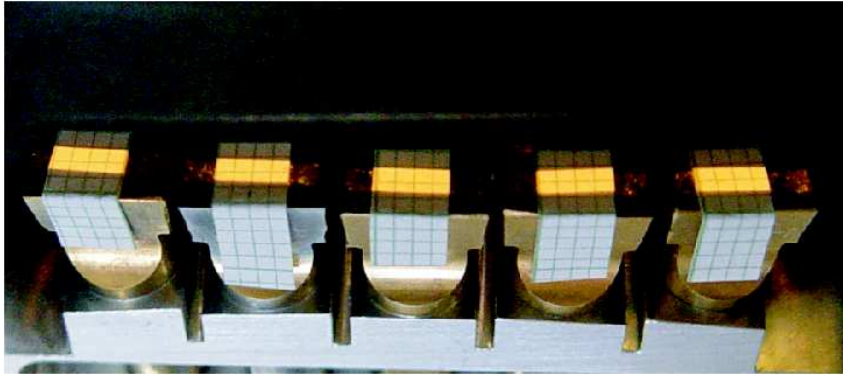


Figure 4.4: The pseudo-slit slices centered on top of the slit mirrors.

### 4.2.1 Image Slicer Unit Alignment

As described above, the function of the image slicer unit is to rearrange the two-dimensional field of view into a quasi one-dimensional pseudo slit. The first optical component of the image slicer unit is made up of five field mirrors (slicer mirrors). The function of these mirrors is to image the pupil (Lyot-stop) onto the center of the next 5 mirrors, which are the so-called capture mirrors. To test if this condition was fulfilled, we brought a mask with central pin-hole into the Lyot-stop. This mask was illuminated from the backside of the Lyot-stop, producing a divergent point source that was imaged by the slicer mirrors onto the capture mirrors. Millimeter graph paper was centered on each capture mirror from which the image position was estimated. The images of the point source were quite sharp, implying that the surface of the slicer mirrors were designed and manufactured within the specification. However, it was found that the images of the pupil were not located at the center of the capture mirrors as desired. This problem was solved by shimming the single slicer mirrors as well as the whole stack of mirrors with aluminum foil. In Figure 4.3, the alignment result is shown. The center of the capture mirrors is located within the red circle and one can see that a sharp, centered image of the pinhole is achieved for all five configurations. The alignment precision is about 0.5 mm, which is  $\sim 8\%$  of the pupil size at this position, while the capture mirrors are oversized by a factor  $\sim 2$  with respect to the pupil.

The function of the capture mirrors is to image the single slices onto the slit mirrors. After the alignment of the slicer mirrors, the Lyot-stop mask was removed and replaced by a diffuse glass screen to achieve a homogeneous illumination of the pupil. In this way more light could enter the system, which simplified the measurement. In Figure 4.4 the images of the slices on top of the slit mirrors are shown. The images are quite sharp and centered on the slit mirrors, demonstrating that the capture mirrors are well oriented and that their surface shape is correct.

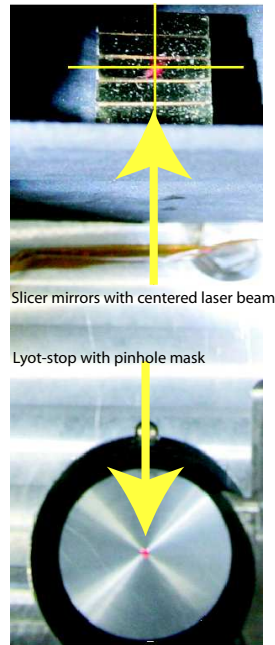


Figure 4.5: The alignment reference axis defined by the Lyot-stop center (pinhole mask) and the center of the slicer mirror stack.

### 4.2.2 Spectrometer Optics Alignment

The next component in the optical path is a flat folding mirror (R5), which reflects the light out of the slicer assembly towards the first collimator mirror (R6). To test the alignment of this mirror and the slit mirrors we used the alignment laser. The optical spectrometer axis is defined by the center of the Lyot-stop pupil and the center of the slicer mirror stack (see Fig. 4.5).

The laser was aligned with respect to this axis using the Lyot-stop pinhole mask. The position of the beam was measured directly behind the location of the fold mirror (R5). As can be seen in Figure 4.6, the beam was perfectly centered in the horizontal direction but its vertical position was about 1 mm too low compared to the expectations from the ray tracing simulation. This small deviation is acceptable, since it will only minimally influence the wavelength calibration and a correction would have required to enlarge the screw holes within the holding plate of the mirror (R5).

After the fit pins of the fold mirror (R5) were removed, the orientation of the mirror was aligned such that the beam hits the required position (indicated by the cross in Fig. 4.7) on the mirror holder of the first collimator (R6) with a precision of about 0.5 mm, corresponding to  $\sim 1\%$  of the beamsize at this position. From the first collimator (R6) the beam is reflected to the second collimator mirror (R7), which is located directly in front of the grating. At the second collimator (R7) the beam was vertically 1 mm higher than expected. This discrepancy is due to the fact that the beam is located 1 mm too low at the fold mirror (R5), an acceptable offset, since it will just cause a minimal shift of the recombined pupil at the grating position. To successfully recombine the pupil of the single configurations at the grating, the orientations of the slit mirrors have

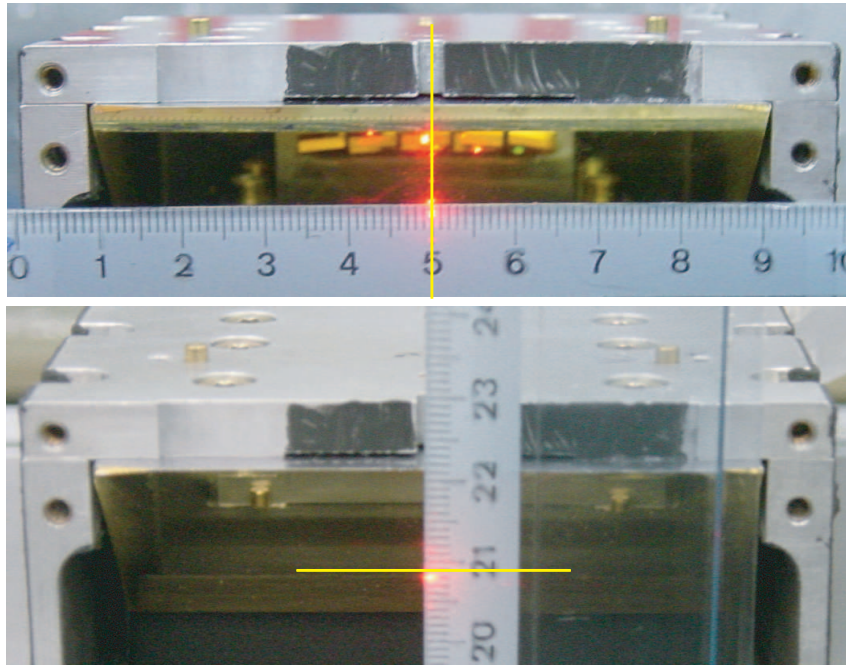


Figure 4.6: Measurement of the laser beam position behind the fold mirror (R5). The horizontal position was found to be perfectly centered, while the vertical position was 1 mm too low.

to be precisely aligned. Small manufacturing errors of the slit mirrors lead to an offset of the single pupils from their pre-defined position, which is the center of the grating. The maximum deviation along the larger axis of the grating is 10 mm and 5 mm along the short axis, corresponding to about  $\sim 8\%$  of the beam size at this position. The magnification factor between the capture mirrors and the extended direction of the grating is 25.5. Since the pupil alignment at the capture mirrors has a precision of about 0.5 mm, the measured deviations of the pupil images at the grating are within expectations. This is also true for the short axis of the grating, since the anamorphic magnification relation is 2:1 between the long and short grating axis. Since the dimensions of the grating are oversized, the pupil misalignment at the grating position will not lead to a loss of light but may cause a small difference in the spectral calibration of the single configurations if the angle of the incident beam changes among the configurations.

In Figure 4.8, one can see the laser beam centered on the grating for the central configuration. The spectrometer is designed to closely resemble a Littrow-configuration, which means that the beam direction is reversed at the grating. The dispersed beam passes the two collimators and falls upon the detector via the exit optics. The exit optics produces an image of the pupil 240 mm in front of the detectors.

Figure 4.9 shows the alignment-verification of the detector-pupil for the central configuration. The yellow lines indicate the expected location of the laser spot in the horizontal and vertical directions. Whereas there is a small offset in the vertical direction of about 0.5 mm, the horizontal direction is perfectly aligned. The offset in the vertical direction of 0.5 mm is acceptable since it only amounts

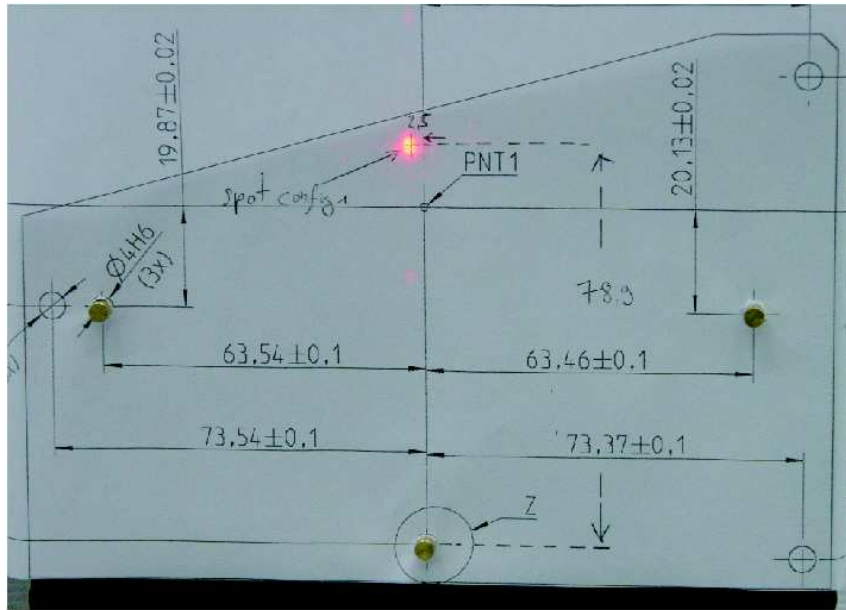


Figure 4.7: The laser beam hits the desired position (for the central configuration) on the mirror holder of the first collimator (R6) (red spot + cross)

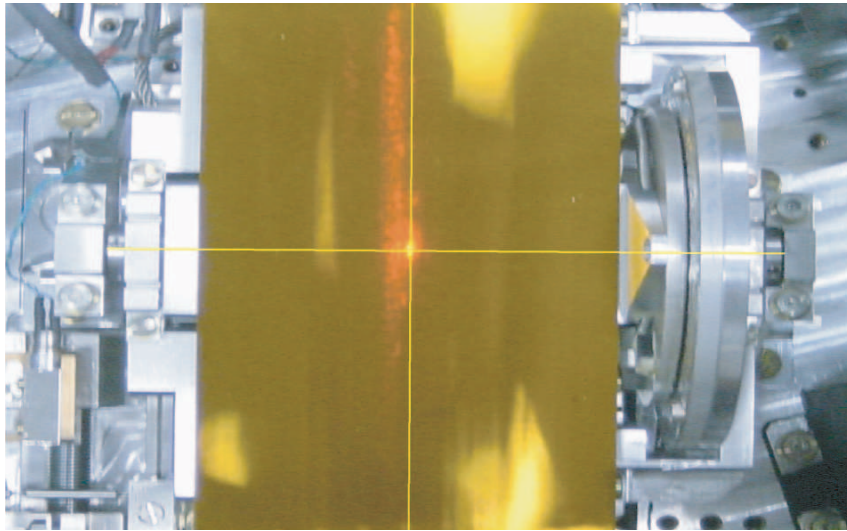


Figure 4.8: The laser beam centered on the grating (for the central configuration).

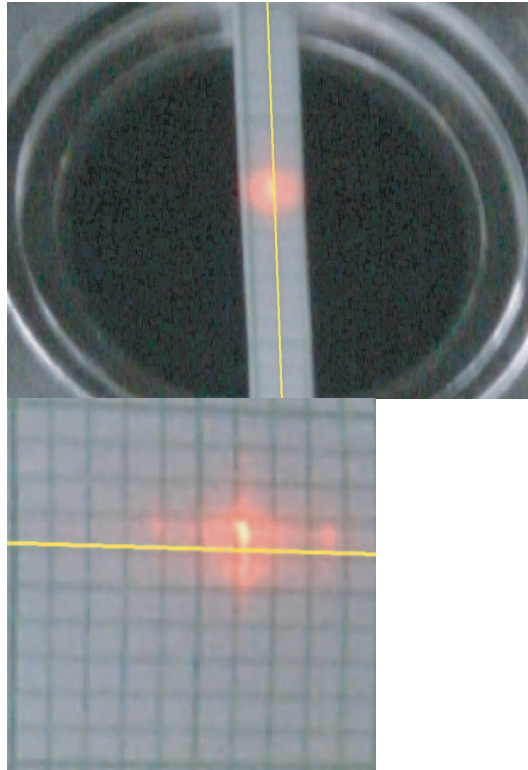


Figure 4.9: Verification of the detector-pupil alignment for the central configuration. The yellow lines indicate the horizontal and vertical expected location of the laser spot. While the pupil is perfectly aligned in the horizontal direction a small offset of 0.5 mm was found in the vertical direction. The precision of the measurement is also  $\sim 0.5$  mm.

to  $\sim 11\%$  of the pupil size at this position and the pupil mask is oversized in the vertical direction.

In Figure 4.10, a blaze reflex (for the central configuration) falling onto the detector is shown. A blaze reflex is a direct or multiple reflection at the grating grooves and appears for certain grating orientations. Figure 4.10, shows how the blaze reflex is perfectly centered on the central detector module. This was achieved by rotating the grating and the second collimator mirror (R7) both with their fit pins removed. Changing the grating angle (angle of incidence) by about  $30^\circ$  led to a second much weaker blaze reflex. It was verified that this second reflex was also centered on the central detector module, demonstrating that the rotational axis of the grating is well aligned with respect to the grating surface.

Next, the K-mirror was aligned with respect to the entrance optics. To achieve this, the alignment laser was centered with respect to the rotation axis of the K-mirror and then the reimager (E5) (with removed fit pins) was slightly rotated to align the beam with respect to the reference axis defined by the center of the Lyot-stop and the center of the central slicer mirror (Fig. 4.5). Rotation of the K-mirror did not change the beam alignment at any position within the optical path, confirming that the system was well aligned.

To test if the single slices were correctly imaged into the detector plane the

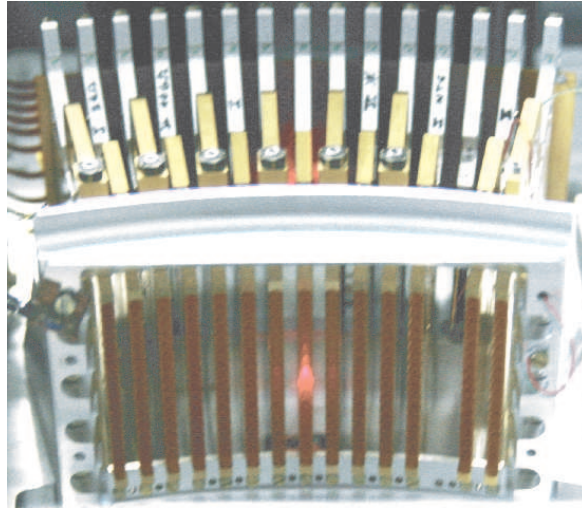


Figure 4.10: The laser beam hits the central detector module as expected for the image center.

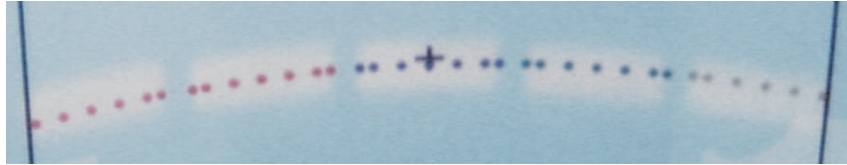


Figure 4.11: Image of the pseudo slit in the detector plane compared to a ray tracing simulation. The black dots are simulated field points vertically centered on each slice. Measurement and simulation are in good agreement, and only a small rotational offset is measured.

Lyot-stop was homogeneously illuminated, and the grating was replaced by a flat mirror mounted into the holding structure of the grating. In Figure 4.11, the images of the slicer mirrors in the detector plane are compared with a ray tracing simulation (black dots). The black dots are simulated field points vertically centered on each slice. The images of the slices fit well the simulation, with only a small rotational offset that will minimally influence the spectral calibration.

### 4.2.3 Cold Test of the Optical Alignment

Since FIFI-LS operates in the far-infrared, the instrument is cooled to a few Kelvin. The optical alignment was done at room temperature, so does the alignment change when the instrument is cold? To investigate this, the central detector module of each configuration was replaced with a dummy module. In these dummy modules a LED (light emitting diode) was mounted at the location of the central spectral detector pixel. This allowed us to send light from the detector plane backwards through the entire optical path of FIFI-LS. In addition, reference crosses made from thin wires were placed at the pupil positions (at the Lyot-stop, the grating and the detector pupil). The grating was replaced by a mirror in this experimental setup. Finally the cryostat was closed and evacuated.

Pictures of the pupil and the focal plane were taken by changing the focus of a camera, which was located in front of the entrance window of the cryostat. This was done twice, once with the cryostat at room temperature and once cooled with liquid nitrogen to about 70 K. In Figure 4.12 the results are presented. The two columns on the left side of Figure 4.12 show the warm setup, while the two columns on the right side show the situation with the cooled instrument. The images in the first column show the focal plane (slicer stack). The LEDs in the detector plane can be seen simultaneously. In each image (A,B,C,D,E) a different configuration (LED in detector plane) is selected. In the second column the pupil images are shown with overplotted colored lines across the reference wires. The colors indicate the different pupils (black: Lyot-stop, blue: grating, green: in front of detector). The same was performed for the cold case as shown in column 3 and 4 of Figure 4.12. By comparing the warm and the cold setup it was found that the pupil was stable while the focal plane was vertically shifted in the cold case. A ray tracing simulation showed that the 2nd collimator mirror, which is directly located in front of the grating, must be responsible for this offset. Because this mirror is located almost inside the pupil, a small change of its alignment would only minimally influence the pupil image but would have a strong effect on the focal plane, which is located further away. This mirror is located at the edge of the optical bench, further away from the helium vessel that stabilizes the optical bench. Additional tests showed that in fact the edges of the optical bench are critical. They were not stiff enough to ensure a stable alignment. Because of this, a structural support has been designed that is mounted below the optical bench to increase its stiffness.

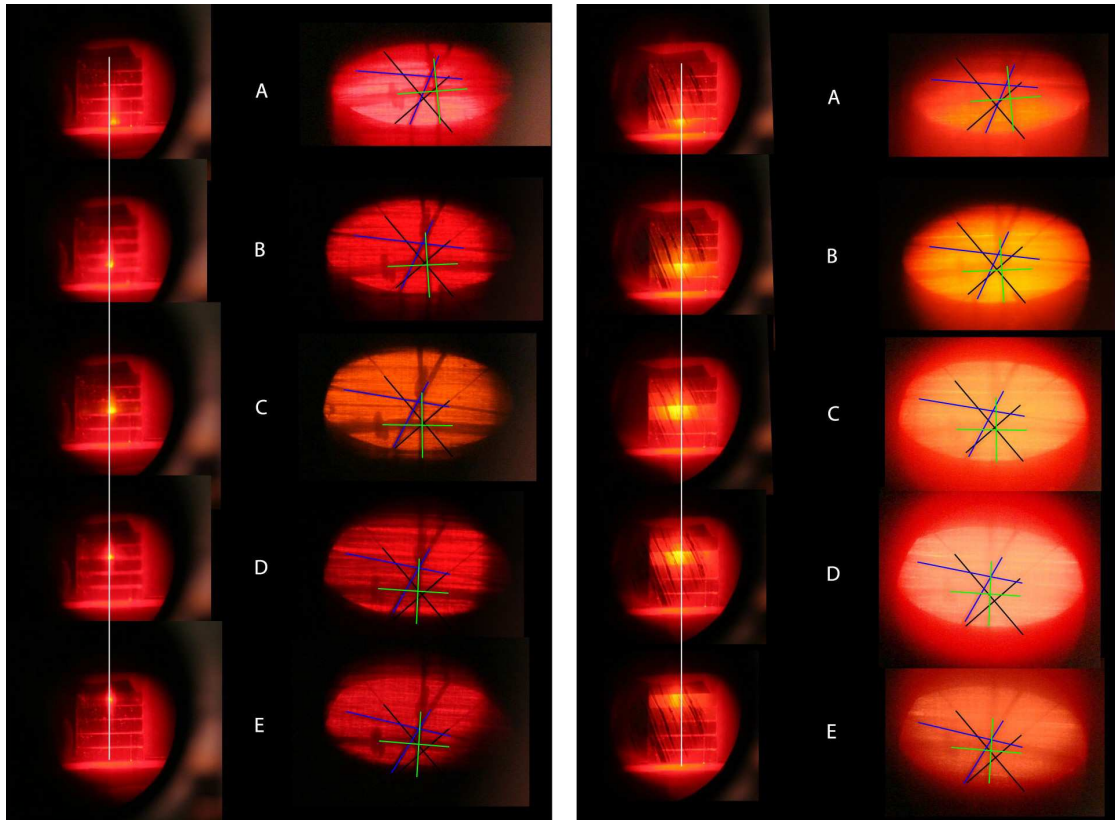


Figure 4.12: Test of the optical alignment with nitrogen cooled cryostat. The first two columns are for a warm cryostat and the last two columns are for a cold cryostat. First column is the focal plane. The slicer mirrors as well as the LED in the detector plane can be seen simultaneously. The second column is the pupil plane. The reference wires in the pupil positions can be seen. Columns 3 and 4 are the same but with the cold cryostat. The colored lines across the reference wires indicate the different pupils (black: Lyot-stop, blue: grating, green: in front of detector). This shows that the image shifts slightly in the vertical direction while the pupil stays stable.



# Chapter 5

## The Telescope Simulator

So far, all the tests (geometrical alignment) were done in the optical wavelength range. The next step was the verification of the instrument performance in the FIR. A telescope simulator was designed, built, and aligned for this reason. The telescope simulator reproduces the SOFIA FIR telescope beam. This is necessary in order to test whether the optical path of FIFI-LS is well aligned with respect to the optical axis of the SOFIA telescope using the SOFIA mounting flange/plane as a reference. The optical performance of all FIFI-LS components can be tested at their working temperatures and in the FIR. Furthermore, the telescope simulator allows us to characterize the spectral and imaging properties of FIFI-LS.

For testing the spectral performance, the telescope simulator has a gas cell mounted into the optical path that can be filled from outside (e.g. with CO). The gas cell provides FIR molecular emission lines, since it is mounted in front of a cold background. It can be used to spectrally calibrate the instrument and to measure the spectral resolution of FIFI-LS. To test the imaging properties of FIFI-LS, a FIR point source is scanned through the field of view. This allows one to test the optics in the cold. By scanning the point source across the field of view, a beam map can be measured that delivers the point spread function (PSF) of the instrument. In addition, a cooled infrared black mask can be brought into the pupil to homogeneously illuminate the entire detector array.

### 5.1 Design and Alignment of the Telescope Simulator

To reduce the costs of the telescope simulator, components from a former instrument were used. One of these components was the vacuum vessel of the former FIFI instrument (KAO). This restricted the entire design to fit into the vessel envelope. Other re-used components were the gas cell and the chopper mirror. The first step in the design was to set up the entire optical system in the ray tracing program ZEMAX, taking into account the outer boundary condition given by the dimensions of the vacuum vessel. The final ray tracing result is shown in Figure 5.1 and 5.2. To ensure that the telescope simulator reproduces the beam of the SOFIA telescope a trick was employed: The SOFIA telescope beam was

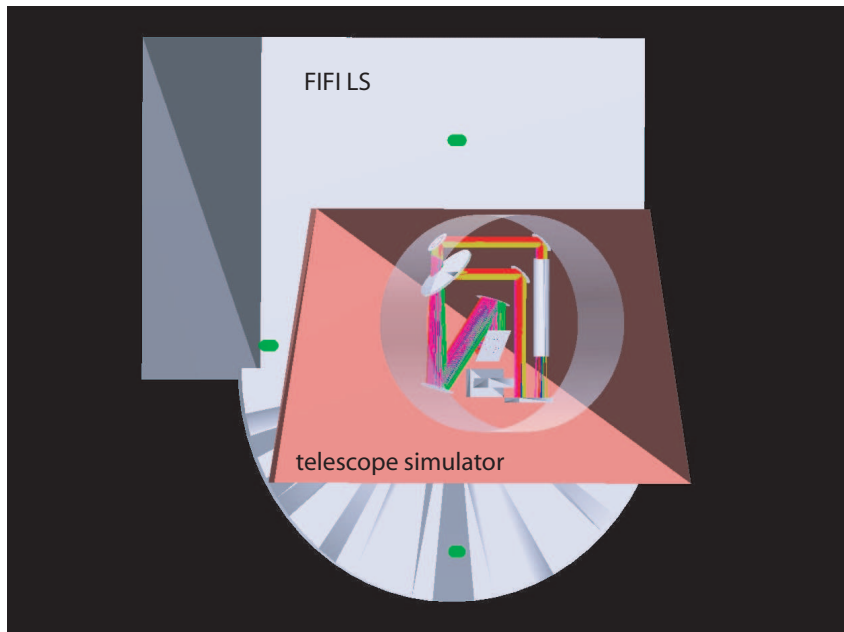


Figure 5.1: ZEMAX ray tracing simulation of the telescope simulator mounted on FIFI-LS.

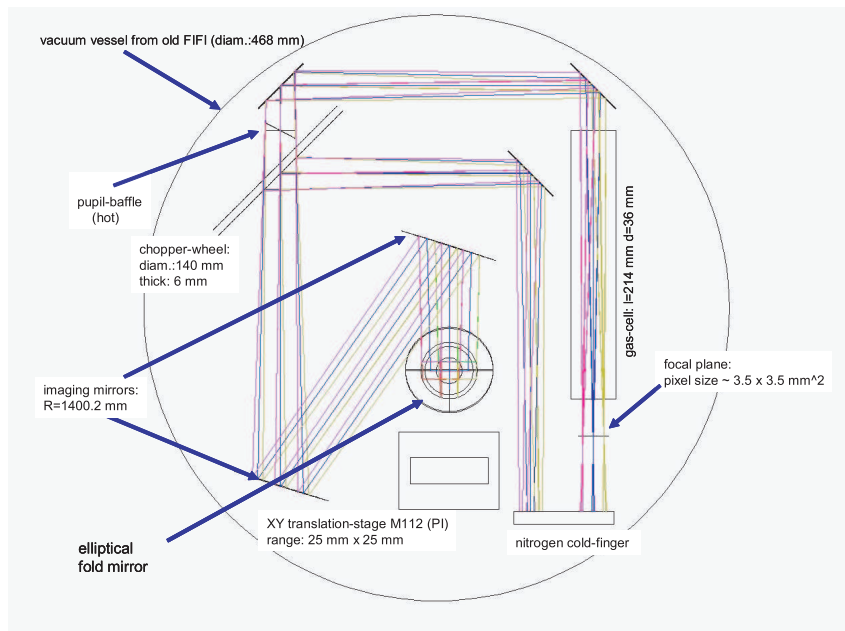


Figure 5.2: ZEMAX ray tracing simulation of the optical path of the telescope simulator.

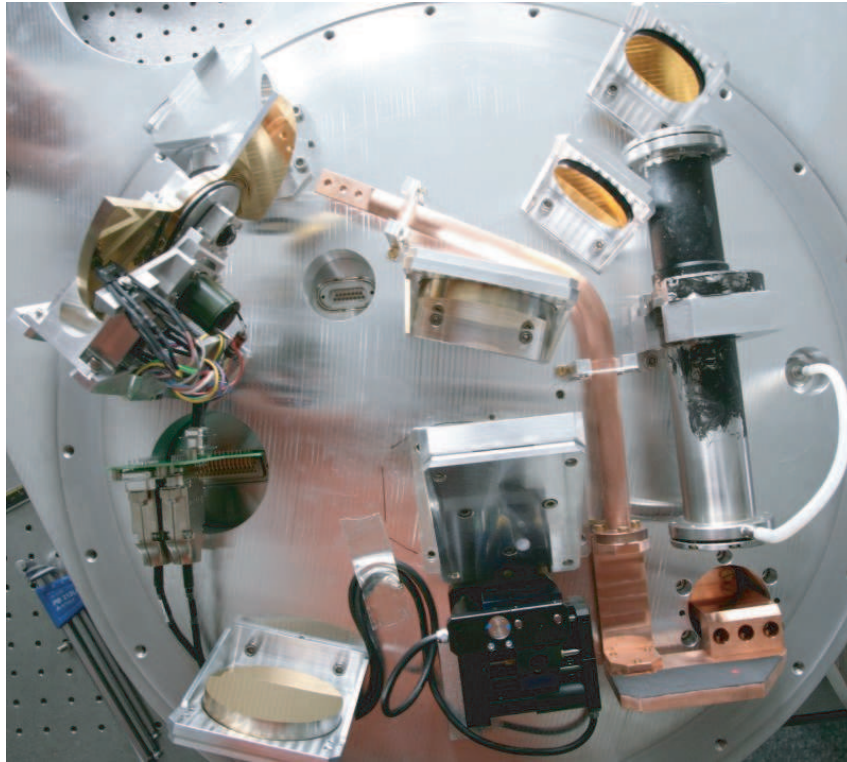


Figure 5.3: Picture of the actual telescope simulator (compare to Figure 5.2).

used as an input for the ray tracing simulation of the telescope simulator. The simulator was then developed backwards from its final reflecting mirror to the focal plane. This method ensured that the reversed optical path properly reproduces the SOFIA telescope beam. Two imaging mirrors are used in the telescope simulator to produce an image of the detector plane as well as an image of the pupil (Lyot-stop). These mirrors are off-axis hyperboloids. All other mirrors in the setup are flat mirrors. The telescope simulator can be mounted on FIFI-LS with respect to the SOFIA telescope reference mounting plane, which will be used to mount FIFI-LS onto the SOFIA telescope.

A vacuum sealed box establishes the optical and mechanical connection between the telescope flange and the entrance window of FIFI-LS. This box contains in addition the optical guiding camera system and is used to guide the telescope with respect to the center of the FIR field of view of FIFI-LS. This is the so-called “boresight box”. Since the actual boresight box was not finished, a boresight box dummy (see Fig. 5.7) was designed to produce a vacuum sealed connection between the telescope simulator exit and the FIFI-LS cryostat entrance window. In operation, the entire telescope simulator including the connection to the FIFI-LS entrance window is evacuated.

**The Point Source:** An xy-translation stage that is integrated in the telescope simulator, allows one to scan a point source (Fig. 5.4) in two dimensions across the focal plane. The point source is a gold plated spherical segment with a



Figure 5.4: The point source in front of the gas cell. The point source is a gold plated spherical segment with a diameter of 2 mm.

diameter of 2 mm, which is fixed with two thin suspension wires. Since the detector pixel size in the focal plane of the telescope simulator is about  $3.5 \times 3.5 \text{ mm}^2$  the spherical segment can be considered a point source for FIFI-LS. The suspension wires ( $30 \mu\text{m}$  in diameter) are fixed to a holding clamp mounted on the xy-translation stage. Behind the focal plane, a copper plate is located in the optical path. This plate is connected to a cryogenic vessel. The vessel is filled from outside the telescope simulator with liquid nitrogen to cool the copper plate. The rest of the telescope simulator is at room temperature. The gold plated spherical segment in the focal plane serves as a reflector, which reflects the ambient room temperature radiation into the optical path of FIFI-LS.

The copper plate is painted black with an infrared black paint. This cool background produces the contrast necessary to see the warm reflected room temperature radiation as a FIR point source. Using the telescope simulator an automated point source scan can be performed to measure the PSF of FIFI-LS within the entire field of view. The size of the scan region, the number of positions within this region, and the waiting time at each single position have to be entered into the control program of the telescope simulator before the scan is started. To be able to identify the single detector readouts with the proper motor positions, the FIFI-LS computers and the computer controlling the telescope simulator are synchronized by their CPU times. FIFI-LS marks each read-out with a time stamp, and the telescope simulator marks each point source position with a start and a end time that is written into an additional file. In this way, the data can be correlated with the individual point source positions.

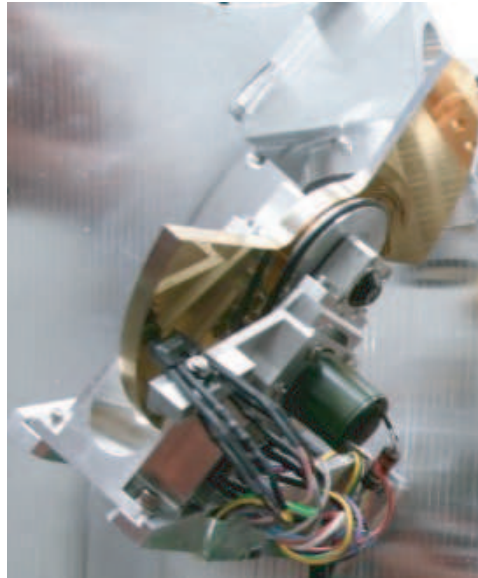


Figure 5.5: The chopper mirror with light switches to synchronize its rotation to the read-out sequence of FIFI-LS.

**The Chopper Mirror:** To achieve a meaningful observation in the FIR it is necessary to subtract the ambient background radiation from the actual observation. At the SOFIA telescope, the secondary mirror is used to chop the field of view on and off the source. This is necessary since the background radiation in the FIR (e.g. due to the telescope and to the remaining atmosphere emission) is in general high. The telescope simulator offers the possibility to obtain chopped observations using a chopper mirror, shown in Figure 5.5. It is mounted directly in front of the pupil. The chopper mirror rotates, thus switching between two optical paths. The nominal optical path is seen if the chopper mirror is out of the beam. In this configuration FIFI-LS has a direct view onto the focal plane and the point source with the cooled copper plate in the background. When the chopper mirror is inside the beam, the reference path is selected. The reference path uses two additional flat mirrors to achieve a direct view onto the cooled copper plate, excluding the point source. Using the reference path, a background image can be acquired which can be subtracted from the actual observation. This solves the problem of a dominant and potentially time varying background.

**The Gas Cell:** Using the gas cell, FIFI-LS can be spectrally calibrated and characterized. The gas cell can be brought into the beam of the nominal optical path. Its windows are made from a thin polypropylene foil. The length of the gas cell is 214 mm and its diameter is 36 mm. A tube connects the cell to the outer part of the telescope simulator. The tube is used to bring a gas (e.g. CO or ambient air) into the gas cell. For a line measurement, the point source is moved out of the field of view. Since we have a warm (room temperature), optically thin gas ( $\sim 20$  mbar) in front of a cool background ( $\sim 70$  K), the gas shows molecular emission features.

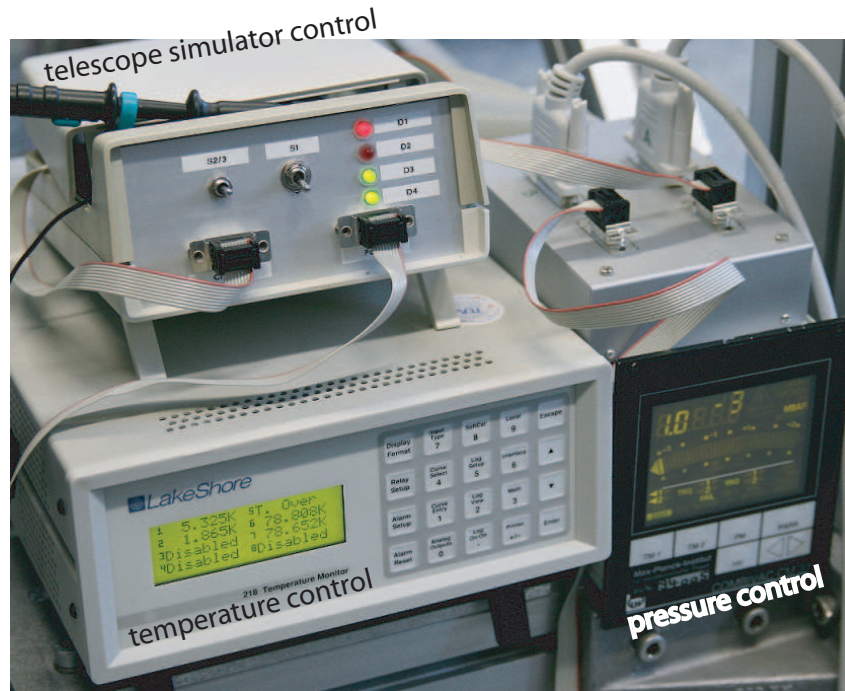


Figure 5.6: The control electronics are shown; in the upper left, the PLL control box for the telescope simulator is indicated.

**The “Warm” Pupil Mask:** Before any measurement with the telescope simulator is performed, the optical axis of the telescope simulator has to be well aligned with respect to the optical axis of FIFI-LS. A warm (room temperature) pupil mask is located at the pupil position of the telescope simulator, which can be used to align the two axes with respect to each other. The mask has a centered hole with exactly the size of the pupil. If the two axes were misaligned, the outer warm rim of the pupil mask would enter the beam of FIFI-LS, increasing drastically the FIR background signal of all detectors. By aligning a fold mirror located within the boresight box dummy, the FIR background signal can be minimized. In this way, the two optical axes can be aligned with respect to each other.

**The Control Electronics:** Since FIFI-LS reads out the data from the detectors with a selectable frequency, it is important that the rotation of the chopper mirror is synchronized with the readout sequence of FIFI-LS. After the synchronization the data collection can start. The data are stored in a sequence of nominal path and reference path observations, with the readout sequence of FIFI-LS controlled by the so called “pattern generator”. The pattern generator also provides a TTL (Transistor-Transistor-Logic) signal that can be used for the synchronization. Figure 5.5 shows the chopper wheel and the light switches, which are mounted in front of the chopper wheel. Two light switches mounted under  $45^\circ$  with respect to each other detect the rotation frequency of the chopper wheel and its phase. Frequency and phase are then compared to the frequency and phase of the pattern signal using a PLL (phased locked loop) circuit which

controls the synchronization. After a short time ( $\sim 10$  seconds) a stable, synchronized rotation is achieved. The simulator uses two light switches simultaneously to increase the sampling rate, so that for low rotation frequencies the PLL circuit is still able to synchronize the rotation with the pattern signal. In total, four light switches are used to control the chopper wheel. All the light switches are used together to identify the orientation of the chopper wheel and four LEDs indicate the orientation of the chopper wheel by showing the status of the light switches. In manual chopper mode, the chopper wheel can be moved by hand by pressing a switch. In this way, one can select the nominal or the reference optical path for a measurement. In Figure 5.6 the control electronics are shown.

## 5.2 Preparation of the Telescope Simulator

**Measuring the Geometry:** Since the function of the telescope simulator is to simulate the SOFIA telescope, it is necessary that the orientation of its optical axis is the same as the expected orientation of the telescope axis, which is perpendicular to the reference mounting plane of FIFI-LS and centered within the connection-flange. The geometry of the telescope simulator was measured using a high precision 3D measuring machine to assure that its base, which is used to mount the simulator to the reference plane of FIFI-LS, is parallel to the optical bench of the simulator. This is important since the optical bench is the alignment reference for the optical components of the telescope simulator. It was found that the deviation from a parallel orientation of the optical bench and the base of the telescope simulator is not larger than  $0.01^\circ$ . It may well be that this angle is even smaller in the nominal position when the simulator is mounted (and fixed with screws) to FIFI-LS.

**Alignment of the Telescope Simulator:** The next step was to align the optics of the telescope simulator in a way that its optical axis is perpendicular to its optical bench (and its base) and centered within the exit flange. To achieve this, the simulator was mounted with its base onto an optical table, with the alignment laser positioned at a distance of  $\sim 1500$  mm on the same table. A mask with a central pinhole was used to center the beam within the exit flange of the simulator. A mirror was mounted across the exit hole parallel to the optical bench of the simulator. This mirror reflected the beam back. In this way the laser was auto-collimated relative to the optical bench of the simulator, with a precision achieved for the auto-collimation of about 0.5 mm or  $\sim 0.02^\circ$ . Thus, the laser beam was centered (due to the pinhole mask) within the exit flange of the simulator and aligned perpendicular to the optical bench. Then, the mirror (across the entrance hole) was removed, and the individual optical components of the simulator aligned with respect to the optical axis defined by the aligned laser beam.

**Alignment of the Telescope Simulator with respect to FIFI-LS:** We were now in a position to mount the telescope simulator onto FIFI-LS. But be-



Figure 5.7: The boresight box dummy. This is a replacement for the actual boresight box which was not manufactured at this time. The dummy has an internal mirror, which reflects the beam into the cryostat. It can be used to align the optical axis of FIFI-LS with respect to the telescope simulator. The real boresight box will contain the guiding camera system.

fore FIFI-LS was cooled down, another alignment step was necessary, i.e. the alignment of the optical axis of FIFI-LS with respect to the optical axis of the telescope simulator, by aligning the boresight box dummy (see Fig. 5.7), which contains a flat mirror reflecting the simulator-beam into the FIFI-LS cryostat. To test the alignment in the optical, the Lyot-stop of FIFI LS was illuminated by a centered point source (LED) from the spectrometer side of the instrument. If the alignment is correct, the image of this point source is projected into the center of the pupil inside the telescope simulator. By aligning the boresight box dummy we could fulfill this requirement. The same alignment is possible in the FIR using the “warm” pupil mask of the telescope simulator as explained above.

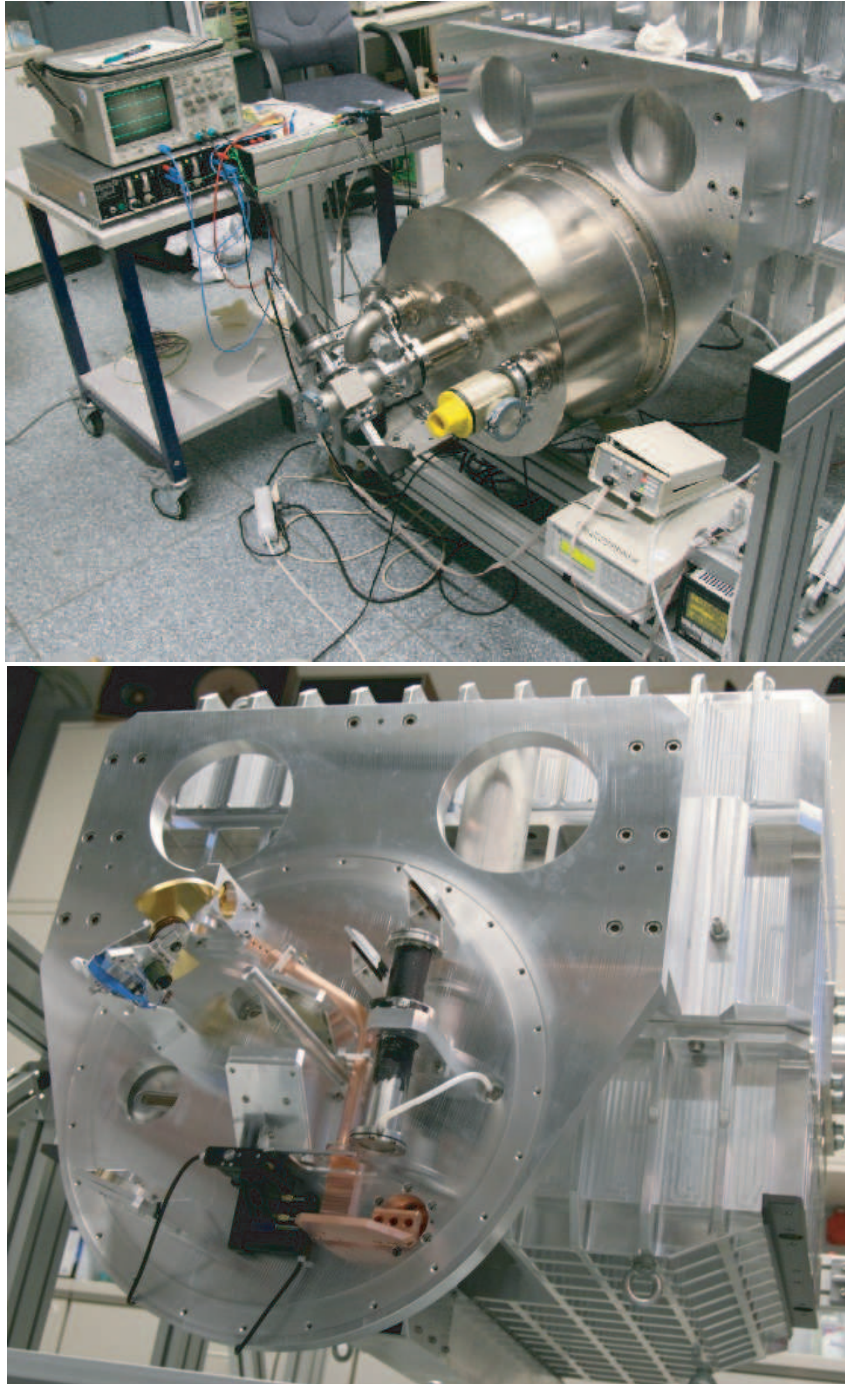


Figure 5.8: The telescope simulator mounted on FIFI-LS. Upper panel: simulator cooled, evacuated and connected to the control electronics; lower panel: open telescope simulator.



# Chapter 6

## Characterizing FIFI-LS

The spectral and imaging properties of FIFI-LS were tested in two cool downs, during which we performed measurements with the telescope simulator. We performed a point source scan across the field of view to measure the PSF of FIFI-LS. In order to measure the spectral resolution and to achieve a spectral calibration, the gas cell was filled under low pressure ( $\sim 20$  mbar) with air of ambient humidity (or carbon monoxide) while at the same time a grating scan was performed. The results of these measurements are presented in the following sections.

### 6.1 Measuring the PSF

Firstly FIFI-LS and the telescope simulator were evacuated and cooled to their working temperatures and the point source was centered within the field of view. Prior to any measurement the rotation of the chopper mirror has to be phase locked to the pattern signal (readout sequence). This synchronization has been observed using an oscilloscope (Fig. 6.1), and was found to be stable after an initial settling time of about 10 seconds. The phase between chopper position and FIFI-LS readout was set by optimizing the time delay between the pattern signal and the actual FIFI-LS readout. The optimum time delay was found by observing the readouts (ramps) as illustrated in Figure 6.2. The ramps are the time integrated signals (in Figure 6.2 selected for one individual pixel). For the measurements we have chosen 4 ramps per half cycle of the chopper. The first readout (upper ramps in Fig. 6.2) was taken along the nominal beam. The second/fourth readout was recorded while the chopper mirror moved in/out of the beam so that the signal became weaker/stronger with time. These ramps were not used in the data processing. The third readout (lower ramps in Fig. 6.2) was taken along the reference beam (no source), so that the total signal was weaker than for the nominal beam. For the data processing only the first and the third ramp were used while the third ramp (reference beam) was subtracted from the first ramp (nominal beam) to achieve a subtraction of the background signal.

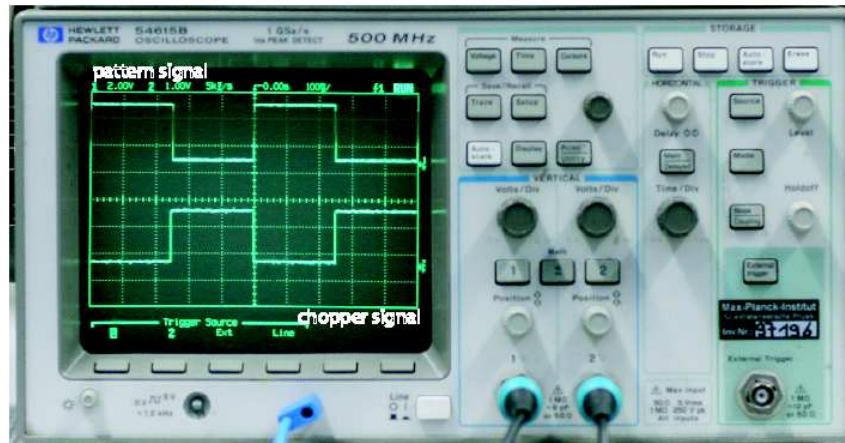


Figure 6.1: Oscilloscope showing the synchronization between pattern signal and chopper mirror rotation.

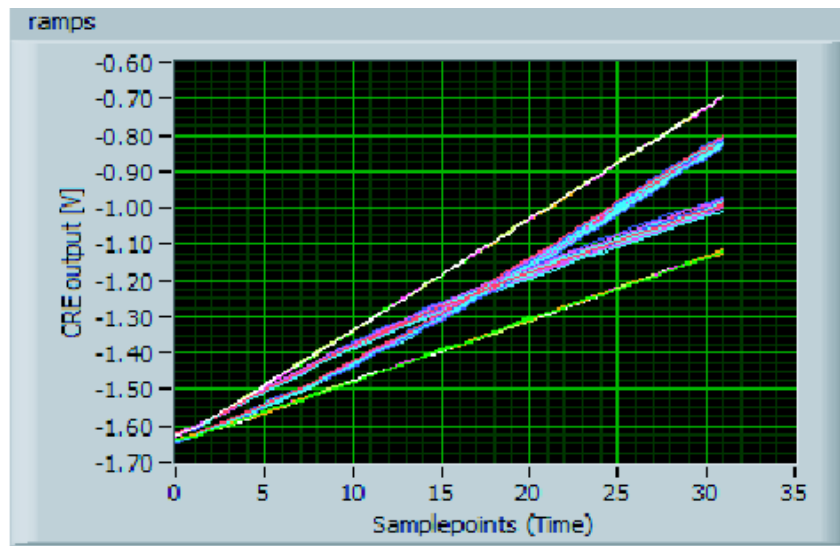


Figure 6.2: Multiple time integrated signals for one individual detector pixel (ramps). Upper ramps: chopper mirror located out of beam = nominal beam (on source); Lower ramps: chopper mirror located in the beam = reference beam (off source); The other ramps were taken at the time where the chopper mirror moved in/out of the beam and were not used for the data processing.

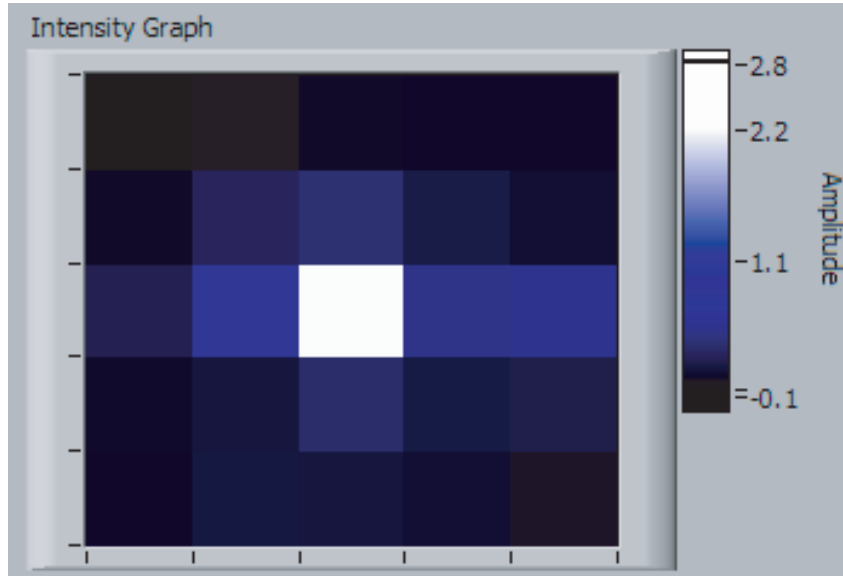


Figure 6.3: The  $5 \times 5$  pixel field of view of FIFI-LS with the centered point source.

In Figure 6.3, the background-subtracted  $5 \times 5$  pixel field of view of FIFI-LS is shown, with the point source located on the central pixel. Multiple ramps were co-added to produce this image. The source seems to be elongated along the horizontal direction. This effect is due to the thermal radiation/reflection of the suspension wires of the source and was also observed in the point source scan (Fig. 6.4).

The grating was in its center position corresponding to a wavelength of  $\sim 160 \mu\text{m}$ . The full width at half maximum of the PSF of FIFI-LS is expected to be not significantly larger than the pixel size. This is due to compromises made in the optical design with respect to diffraction effects at the slicer mirrors. To measure the PSF with a reasonable spatial sampling rate, it is necessary to scan the point source with small spatial steps across the field of view while recording the spectrally collapsed signal for each spatial pixel simultaneously. In Figure 6.4, the spectrally collapsed signal of a single pixel for different positions of the point source is shown. The x-direction was oriented parallel to the extended side of the slicer mirrors and the y-direction was parallel to their short side. The step width of the point source was  $\sim 1.35 \text{ mm}$  (corresponding to 0.39 pixel) and the integration time (waiting time) at each position was 5 seconds. The single point source positions are indicated by the black dots. As was previously observed (Fig. 6.3), an elongated structure is detected (in y-direction). This structure can be explained by the infrared signal produced by the suspension wires of the source. To take this underlying signal into account the measurement was fitted using the superposition of a two-dimensional and second one-dimensional Gauss-function

$$model = a \cdot e^{-0.5\left[\left(\frac{x-x_0}{\sigma_x}\right)^2 + \left(\frac{y-y_0}{\sigma_y}\right)^2\right]} + b \cdot e^{-0.5\left(\frac{x-x_0}{\sigma_x}\right)^2} + c. \quad (6.1)$$

The fit result is shown in Figure 6.4. The resulting fit parameters are :  $a = 2663.16$  ,  $b = 258.266$ ,  $c = -42.7681$ ,  $x_0 = 15.921$ ,  $y_0 = 16.4849$ ,  $\sigma_x =$

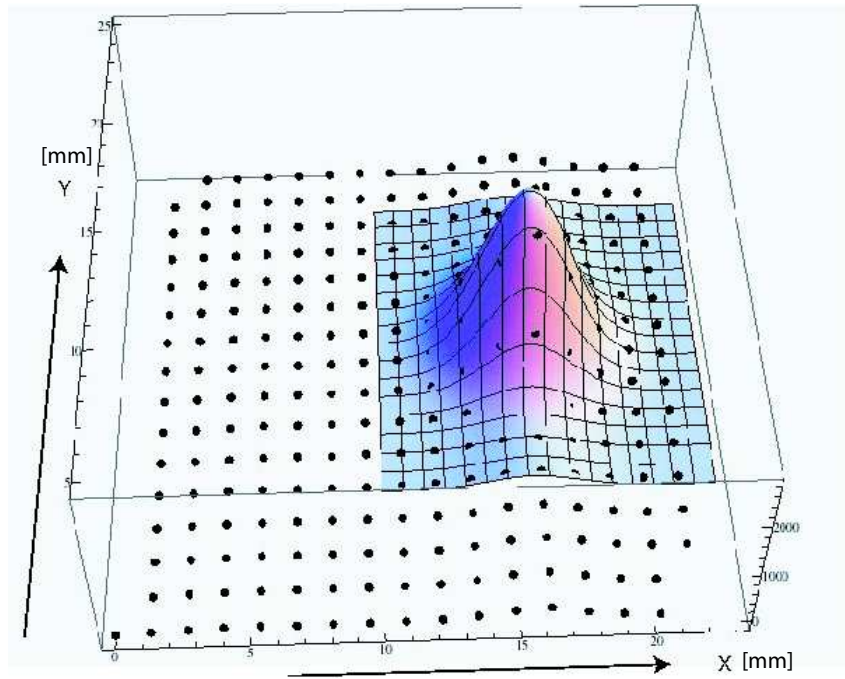


Figure 6.4: A multiple Gauss function fitted to the measured data.

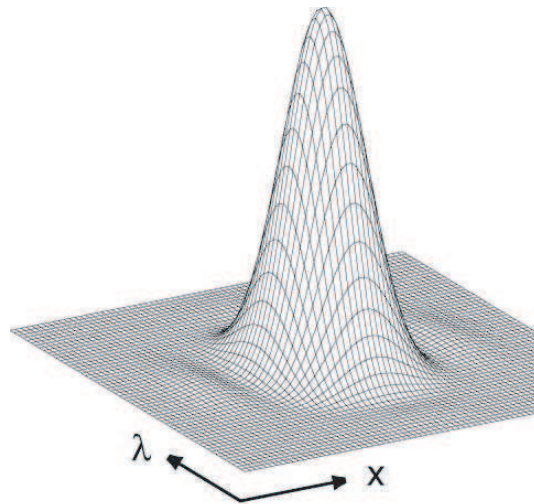


Figure 6.5: The calculated monochromatic PSF in the detector plane.

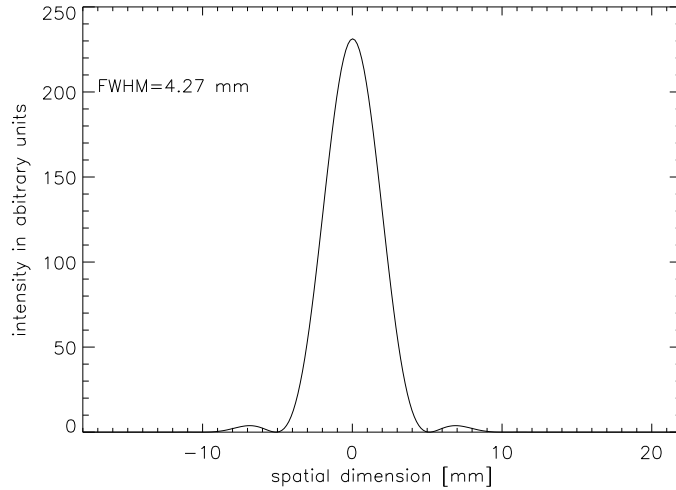


Figure 6.6: A cut through the calculated PSF in the spatial direction. The FWHM is 4.27 mm.

1.73731,  $\sigma_y = 1.52429$  with  $x_0, y_0, \sigma_x, \sigma_y$  given in mm, while  $a, b, c$  are given in arbitrary units. For the full width at half maximum in the x direction, we obtained  $\text{FWHM}_x \sim 4.1$  mm and in y direction  $\text{FWHM}_y \sim 3.6$  mm. Due to a magnification factor of  $\sim 1.037$  between the detector plane of FIFI-LS and the focal plane of the telescope simulator this result translates into  $\text{FWHM}_x \sim 4.3$  mm and  $\text{FWHM}_y \sim 3.7$  mm in the detector plane of FIFI-LS. The magnification factor has been determined using a ray tracing simulation and verified by measuring the intensity distribution (as in Fig. 6.4) for separate pixels. A difference in the FWHM between the x and y directions is expected and caused by the fact that the slicer mirrors cut more light out of the diffraction pattern along their short side (y-direction) than along their extended side. The lower transmission for the energy within the wings of the point source diffraction pattern in the y-direction tends to decrease the FWHM of the PSF in this direction. It has been verified that the smaller FWHM of the PSF is oriented along the shorter direction of the slicer mirrors.

For FIFI-LS, W. Raab performed a detailed scalar diffraction analysis in his thesis (W. Raab 2002) using the software package GLAD. A simulated diffraction pattern for a point source was calculated in the detector plane of FIFI-LS and is presented in Figure 6.5. The FWHM along the spatial direction was 4.3 mm, measured from a cut through the diffraction pattern as shown in Figure 6.6. Since the pixel size (3.6 mm) of the detector is similar to the FWHM of the PSF, the intensity distribution of the diffraction pattern has to be convolved with the pixel size of the detector. This slightly increases the FWHM. Taking also the difference for the transmission in the horizontal and vertical direction of the slicer mirrors into account, the expected FWHM in the detector plane is  $\text{FWHM}_x \sim 4.9$  mm and  $\text{FWHM}_y \sim 4.5$  mm. The difference of the FWHM of the PSF between the two directions is  $\sim 8\%$  of the larger FWHM. A comparison to the measured FWHM of the PSF shows that the measured FWHM is slightly smaller, while

the difference between the two directions is  $\sim 14\%$  of the larger FWHM.

While the agreement between the simulation and the measurement is generally good, the small deviations may be explained by the error within the magnification factor, a somewhat different diffraction situation within the simulator compared to the SOFIA telescope, and a slightly smaller effective pixel size caused by the behavior of the light-cones located in front of each pixel. Also, a slightly different wavelength, due to a small deviation from the center position of the grating, may contribute to the deviation between measurement and calculation.

## 6.2 The Spectral Calibration

To perform the spectral calibration, the point source was moved out of the field of view and the gas cell was mounted into the nominal beam. The gas cell was connected to a vacuum pump with an additional valve to fill air or carbon monoxide into the cell. Both gases have strong transition lines in the wavelength range of FIFI-LS. The gas cell was filled with laboratory air under a pressure of  $\sim 20$  mbar. The 16 spectral pixels of the central detector module (center of the field of view) were used to perform a first order spectral calibration of the instrument. Individual water lines (due to rotational transitions) were identified by comparing the pattern of the measured versus expected water lines and used for the spectral calibration of FIFI-LS. For a fixed grating position, the line-widths of all the lines do not cover more than three spectral pixels. To determine the centroid of the line intensity distribution in pixel coordinates a weighting method was used. The weighted line-center was determined using the relation

$$pixel_{line-center} = \frac{\sum I_{pixel} \cdot pixel_{number}}{\sum I_{pixel}}. \quad (6.2)$$

Here  $I_{pixel}$  is the intensity measured for each pixel and  $pixel_{number}$  the pixel number (1-16) in the spectral direction of the respective pixel. The sum runs over the neighboring spectral pixels containing the line flux. The measured spectrum is shown in Figure 6.7, where several water lines were identified. The x-axis of Figure 6.7 shows the position readout for the grating angle (in counts). The y-axis shows the flux density in arbitrary units. The numbers above the lines indicate the wavelength values taken from the literature in  $\mu\text{m}$ . To achieve the spectral calibration, we fitted the measured grating positions for the centroid of a line to its theoretical wavelength using the grating equation. This has been performed for all the lines with a single, consistent set of fit parameters. As fit parameters, we assumed a variable grating period  $g'$  in mm/groove to account for the thermal contraction of the grating. Due to the uncalibrated offset of the grating position readout a constant angle offset  $\alpha$  from the actual measured position is also considered. The grating equation holds for the central spectral pixel (center of detector). To determine the wavelength of lines which were not centered on the detector we took a wavelength shift  $\Delta\lambda_{(pixel-dispersion)}$  into account, the so called pixel dispersion. Thus the grating equation for the Littrow-setup can be written

as

$$\lambda(g', m, \phi + \alpha, \gamma) = \frac{g'}{m}(\sin(\phi + \alpha + \gamma) + \sin(\phi + \alpha - \gamma)) + \Delta\lambda_{(pixel-dispersion)}, \quad (6.3)$$

where  $m$  is the diffraction order,  $\phi$  the Littrow angle,  $\gamma=1.2^\circ$  the deviation from the perfect Littrow configuration. The pixel dispersion  $\Delta\lambda_{(pixel-dispersion)}$  was calculated using the following relation

$$\Delta\lambda_{(pixel-dispersion)}(g', m, \phi, \gamma) = \frac{d}{d\phi} \left( \frac{g'}{m} (\sin(\phi + \gamma) + \sin(\phi - \gamma)) \right) \cdot \text{pixscal} \cdot \Delta_{pixel}. \quad (6.4)$$

Here  $\text{pixscal}$  is a conversion factor converting the incident angle  $\phi$  into pixels at the detector. This value has been determined using a ray tracing simulation.  $\Delta_{pixel}$  is the centroid shift of the line in pixels with respect to the center of the detector. The fit result is shown in Figure 6.8. The red lines indicate the wavelength values for the lines taken from the literature. The blue circles indicate the fitted wavelength values, determined using the grating position readouts and a consistent set of fit parameters. One set of fit parameters ( $g' = 0.117$  mm,  $\alpha = 20.957^\circ$ ) was sufficient to fit all lines very well with a standard deviation of  $\sigma = 0.014 \mu\text{m}$ .

## 6.3 The Spectral Resolution

In order to perform the measurement, the point source was moved out of the field of view, and the gas cell was mounted into the nominal beam. To determine the spectral resolution of FIFI-LS, we measured the CO line at  $162.81 \mu\text{m}$  ( $J=16-15$ ) at a gas pressure of about 20 mbar and at room temperature by scanning the grating (Fig. 6.9). For this measurement we used CO gas at low pressure to prevent the blending of emission lines and minimize the pressure broadening. While the grating was performing the scan, the signal of the central detector pixel was recorded. A Gaussian function was fitted to the measured line, and the FWHM of the line was found to be  $\sim 0.136 \mu\text{m}$ . It follows that the spectral resolution is  $R = \frac{\lambda}{\Delta\lambda} \sim 1200$ . The theoretically expected value can be calculated using the following equation for the approximation of a Littrow-configuration, where the incident and the exit beam coincide

$$R_{theo} = m \cdot N = \frac{m \cdot g \cdot \text{coll}}{\cos(\beta)} = \frac{m \cdot g \cdot \text{coll}}{\sqrt{1 - (m \cdot g \cdot 0.5\lambda)^2}}. \quad (6.5)$$

Here  $m$  is the diffraction order,  $N$  describes the number of illuminated grating grooves,  $g$  describes the groove density in grooves/mm (grating constant),  $\text{coll}$  is the diameter of the collimated beam,  $\beta$  the angle of incidence and  $\lambda$  the wavelength (in our setup,  $m=1$ ,  $g=8.5$  grooves/mm,  $\text{coll}=120$  mm and  $\lambda \sim 163 \mu\text{m}$ ). The expected resolution is then  $R_{theo} = 1414$ . This value is just slightly larger than the measured resolution. The difference can be understood if we take into account that we did not consider the discrete pixel sampling in Equation 6.5. To correct for this effect, the continuous intensity distribution has to be convolved

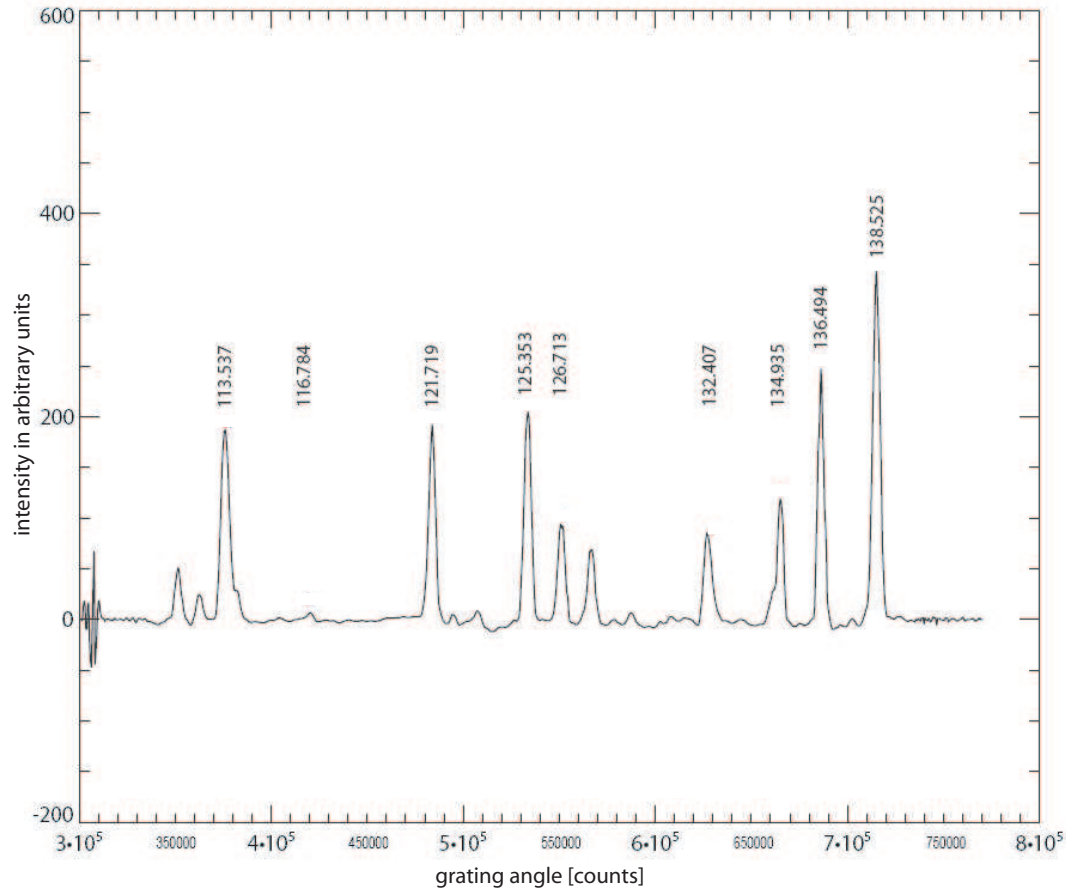


Figure 6.7: Measured water spectrum with the x-axis given in counts of the grating position readout. The y-axis is given in arbitrary units. The numbers above the lines indicate the wavelength values taken from the literature in micrometers.

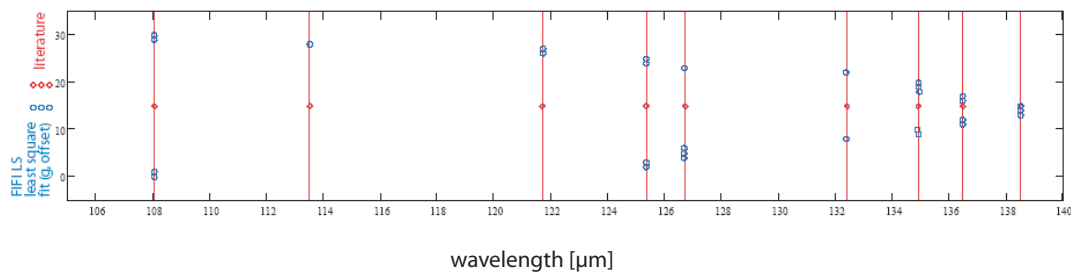


Figure 6.8: Spectral calibration using the water lines from Figure 6.7. The red lines indicate the wavelength values for the lines taken from the literature. The blue circles indicate the fitted wavelength values, taking the grating position readouts and a consistent set of fit parameters into account. The vertical axis indicates the chronological order of the individual line measurements within the grating scan.

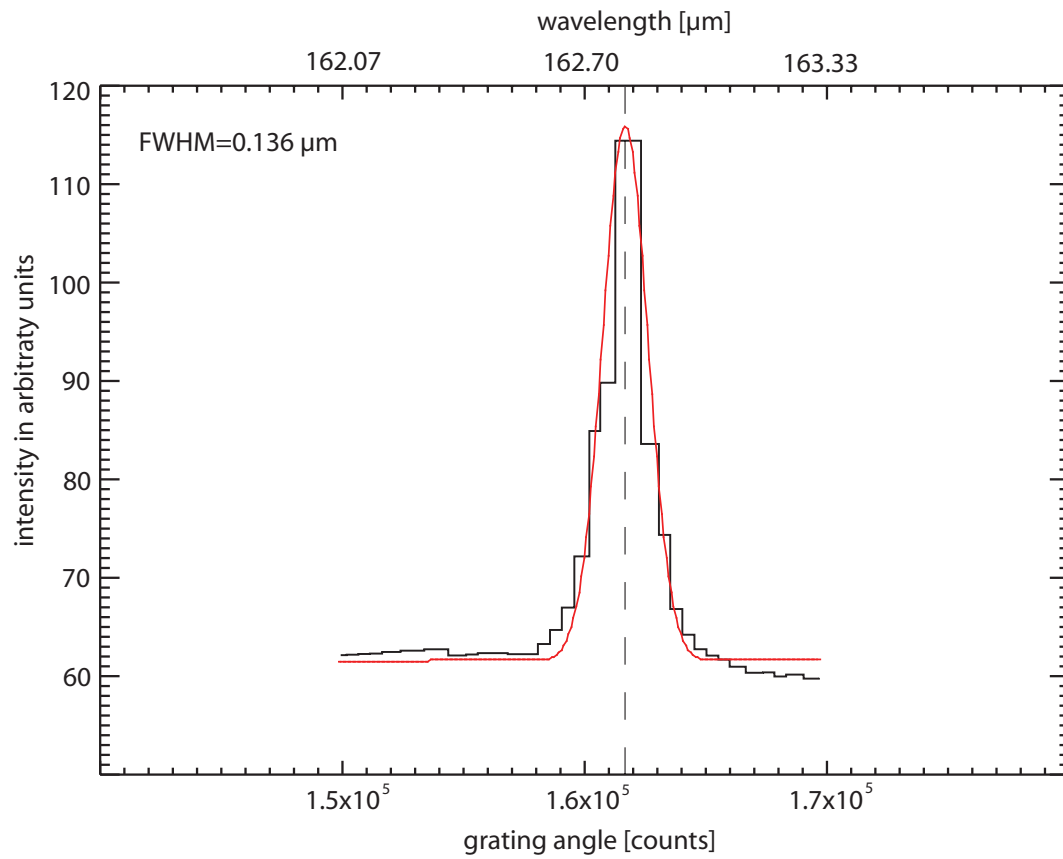


Figure 6.9: CO line (J=16-15 at 162.81 μm) measurement + Gaussian fit with the x-axis given in counts of the grating position readout (with arbitrary offset). The y-axis is given in arbitrary units.

Property	Expectation	Measurement
FWHM of the PSF (at detector, $\sim 160\mu\text{m}$ )	$4.9 \times 4.5 \text{ mm}$	$4.3 \times 3.7 \text{ mm}$
spectral resolution	R=1268	R=1200
spectral calibration		achieved ( $g' = 0.117 \text{ mm}$ , $\alpha = 20.957^\circ$ )

Table 6.1: Comparison of expected and measured instrument properties.

with the pixel size in the focal plane ( $3.6 \times 3.6 \text{ mm}^2$ ). The discrete pixel sampling slightly increases the  $\Delta\lambda$  by a factor of 1.115 (see PhD thesis of W. Raab 2002) at  $160 \mu\text{m}$ , so  $R_{\text{theo-discrete}} = 1268$ . This is in good agreement with the measured resolution. Finally, Table 6.1 summarizes the results and compares the expected and measured properties.

## Part II

# AGN Studies with the Spitzer Space Telescope



# Chapter 7

## Introduction

### 7.1 The Spitzer Space Telescope

The Spitzer Space Telescope was launched in 2003. It provided the scientific community with the most powerful tool yet available for astronomical explorations between 2.6 and 160  $\mu\text{m}$ . Spitzer utilizes an Earth-trailing heliocentric orbit. For Spitzer, the Earth-trailing orbit has several major advantages over near-Earth orbits. The principle advantage is the distance from Earth and its heat; this facilitates the extensive use of radiative cooling, which makes Spitzer's cryo-thermal design extremely efficient. At any time 35% of the sky is visible, and the entire sky is visible every six months. Spitzer operates autonomously in its orbit; once or twice per day the observatory reorients itself so that a fixed X-band antenna mounted on the bottom of the spacecraft points to the Earth and down links 12 to 24 hours of stored data via the Deep Space Network (DSN). Most of the cryogenic telescope assembly (CTA) was at room temperature at launch. Only the science instrument cold assemblies and the super fluid helium vessel were cold within the cryostat vacuum shell. This allowed a much smaller vacuum pressure vessel and a smaller observatory mass than the cold launch architecture used in the Infrared Astronomy Satellite (IRAS) and ISO missions. A combination of passive radiative cooling and helium boil-off vapor cools the components of the CTA after launch. Radiative cooling works for Spitzer because the solar orbit allows the spacecraft to be oriented with the solar array pointed toward the sun, while the Earth is so distant that its heat input is negligible. The system of reflective and emitting shells and shields, which is always shadowed by the solar array, rejects almost all heat that leaks inward while radiating the small amount not rejected into the cold of space. As a result, the outer shell of the CTA achieves a temperature of 34 to 34.5 K solely by radiative cooling. With such a cold outer shell, a small amount of helium vapor suffices to maintain the telescope at its operating temperature, which can be as low as 5.5 K. Spitzer has an  $f/1.6$  primary mirror with a diameter of 85 cm and a Ritchey-Chretien Cassegrain optical design. The telescope optics and metering structure are constructed entirely of beryllium so that changes in both the telescope prescription and its alignment with the focal plane are minimized as the telescope cools on-orbit. A focus mechanism was used to adjust the axial position of the secondary mirror to optimize the focus



Figure 7.1: The Spitzer Space Telescope

as the telescope reached its equilibrium temperature. The Spitzer telescope provides diffraction-limited performance at all wavelength greater than  $5.5 \mu\text{m}$ . The pointing and control system includes redundant gyroscopes and star trackers for sensing the pointing position of the telescope, and reaction wheels for moving the telescope. With this system Spitzer achieves a pointing stability of  $0.03 \text{ arcsec}$  (1 sigma) for times up to 600 seconds.

### 7.1.1 Instruments

Spitzer's three instruments occupy the multiple instrument chamber behind the primary mirror. They share a common focal plane, with their fields of view defined by pickoff mirrors. The instruments achieve great scientific power with uncomplicated design through the use of state-of-the-art infrared detector arrays in formats as large as  $256 \times 256$  pixels. Together the three instruments, IRAC which is the Infra Red Array Camera, MIPS the Multi band Imaging Photometer for SIRTf and IRS which is the Infrared Spectrograph provide imaging and photometry in eight spectral bands between  $3.6$  and  $160 \mu\text{m}$  and spectroscopy and spectrophotometry between  $5.2$  and  $95 \mu\text{m}$ . Compared to previous space infrared missions, most notably ISO, Spitzer brings a factor of 10 to 100 times improvement in limiting point source sensitivity over most of its wavelength band. In addition, the arrays in use on Spitzer provide 100 to 1000 times more pixels than previously available, leading to major increase in efficiency for both imaging and

Module	Detector	Wavelength range (microns)	Resolution
Short-Low (SL)	Si:As	SL 2nd: 5.2-8.7	60-127
		SL 1st: 7.4-14.5	61-120
Blue Peak-Up (SL)	Si:As	13.5-18.7	( $\sim 3$ )
Red Peak-Up (SL)	Si:As	18.5-26	( $\sim 3$ )
Long-Low (LL)	Si:Sb	LL 2nd: 14-21.3	57-126
		LL 1st: 19.5-38	58-112
Short-High (SH)	Si:As	9.9-19.6	$\sim 600$
Long-High (LH)	Si:Sb	18.7-37.2	$\sim 600$

Table 7.1: IRS module operating wavelengths

spectroscopy. Since the following part of this work is related to data taken with IRS, a short description of this instrument is given here.

IRS provides the Spitzer Space Telescope with low and moderate resolution spectroscopic capabilities from 5.2 to 38  $\mu\text{m}$ . The IRS is composed of four separate modules, with two modules providing  $R \sim 60$ -120 spectral resolution over 5.2-38  $\mu\text{m}$  and two modules providing  $R \sim 600$  spectral resolution over 9.9-37.2  $\mu\text{m}$  (see Table 7.1). The IRS has no moving parts and each module has its own entrance slit in the focal plane. The low-resolution modules employ long slit designs that allow both spectral and one-dimensional spatial information to be acquired simultaneously on the same detector array. Two small imaging sub-arrays in the low resolution part of the short wavelength module allow objects to be placed accurately into any of the IRS entrance slits and provide images of sources for photometric or structural information. In Figure 7.2 the four modules installed on the baseplate can be seen. While the low resolution modules are usual grating spectrometers, the high resolution modules use a cross-dispersed echelle design that allows broad spectral coverage in a single exposure. In such a design two crossed gratings are used. First the light falls onto the so called echelle grating which is used in high diffraction orders. This is useful to achieve a high resolution since the resolution of a grating is proportional to the diffraction order. Due to the high order, the single orders overlap after the echelle grating. To disentangle the single orders from each other a second grating, the so-called cross disperser is used. The grooves of this grating are oriented perpendicular to the grooves of the echelle grating so that the single orders are dispersed into different directions and finally imaged onto the detector. The maximum spectral resolution Spitzer achieves with this technique is  $R=600$ .

## 7.2 Active Galaxies

The study of active galaxies is at the forefront of current astronomical research. Astronomers investigating these most powerful objects in the universe use the latest state-of-the-art detection techniques along with the largest and most sophisticated telescopes in the world. To understand the “secrets” of active galaxies, astronomers need to make observations over the entire electromagnetic spectrum,

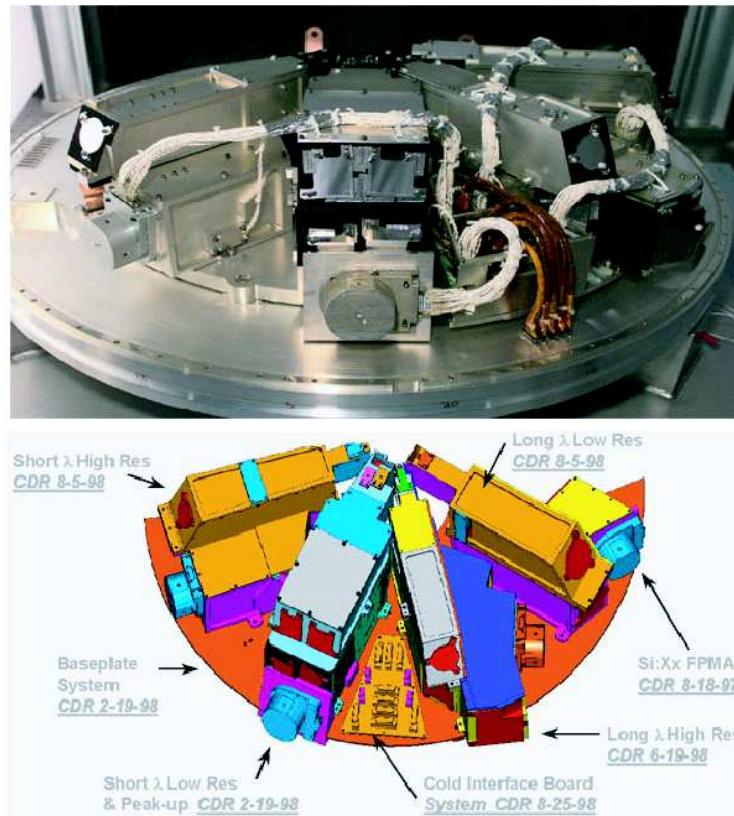


Figure 7.2: The four modules of the Infrared Spectrograph (IRS).

from radio waves through the millimeter/submillimeter, far-infrared, infrared, optical, ultraviolet, extreme ultraviolet, X-rays and finally gamma-rays. To cover this vast spectral range, telescopes in space as well as those on the ground are used. Active galaxies are different from normal galaxies in the fact that they emit the same energy as that emitted by a thousand galaxies like the Milky Way. The power source occupies a volume of space only about the size of the solar system. Quasars (QSOs) are the most powerful of the active galaxies. Some quasars are highly luminous radio emitters, others are very bright in X-rays, while all show emission lines of highly ionized species. The output of a number of active galaxies is known to vary with time, sometimes on timescales as short as minutes and hours. A minority of objects have narrow jets arising from their centers. In the most luminous objects, the quasars, the central luminosity source is so powerful that it easily outshines the light from all the surrounding stars of the host galaxy. Then we no longer see the extended galaxy, but only an intense central point source. This central engine can be explained by material accreting onto a supermassive black hole where supermassive refers to masses greater than about  $10^6 M_{sun}$ . These supermassive black holes possess deep gravitational potential wells and work like enormous engines, converting potential energy of in-falling material into kinetic energy. In doing so, the material that is being dragged towards the black hole produces an accretion disk and is heated to high temperatures ( $T \gtrsim 10^5 \text{K}$ ). This radiant energy is emitted mainly in UV and X-ray. Hence the fundamental power source of active galaxies is the gravitational potential well of

a supermassive black hole.

Since the first publication presented in this thesis will treat silicate emission in a LINER, we will here shortly introduce LINERs. LINERs are Low Ionization Nuclear Emission line Region galaxies. They are active galaxies with the lowest luminosities within the AGN population. LINERs are classified spectroscopically and two main factors stand out; the presence of strong emission from neutral oxygen (OI) at 630 nm (also observed in Seyferts) and the weakness of lines from highly ionized species such as doubly ionized oxygen [OIII] and quadruply ionized neon (NeV), both of which are strong in the spectra of Seyfert nuclei. They are distinguishable from normal spiral galaxies by frequently having compact flat spectrum radio cores and some show point-like X-ray emission. In the optical however, the nuclear emission is weak compared to the surrounding starlight, precisely opposite to the situation of QSOs in which the nuclear emission outshines the starlight from the underlying galaxy. LINERs can be considered mini-Seyferts.

Another important category of galaxies are the so-called ULIRGs. ULIRGs are Ultra Luminous Infrared Galaxies with a substantial fraction showing AGN activity (e.g., high excited line emission like [OIV]). They are very dusty systems with high star formation rates as inferred from their strong PAH (poly-cyclic aromatic hydrocarbons) emission features. Since these systems are very dusty and their star formation rate is high, the stellar ultra violet emission is reprocessed by the dust and re-emitted in the infrared which explains their strong emission in the infrared. ULIRGs are related to galaxy mergers. The compression of material within merging galaxies, and especially within the interacting regions results in an increased star formation rate. At the same time may this disturbance cause an inflow of matter towards the central black hole and trigger the activity of an AGN. In this way ULIRGs and QSOs could be connected evolutionarily like supported by computer simulations (Di Matteo, Springel, Hernquist 2005). In such a scenario the merging of galaxies triggers the ULIRG phase, and the infall of matter triggers the activity of the AGN. After the system relaxes and the dust settles within the gravitational potential, the naked QSO becomes visible (for a review on ULIRGs and AGN see Verma et al. 2005).

### 7.2.1 The AGN Unification Model

A variety of active galaxies covering a broad range in luminosity with different spectral properties have been observed. Seyfert galaxies show lower luminosities within the AGN population, while QSOs are the most luminous AGN. Some of the AGN show a certain level of non-thermal radio emission while others are radio quiet. Active galaxies are divided into sub-classes depending on their spectral appearance. The largest difference is found between so called Type-1 and Type-2 sources. Type-1 sources are characterized by showing broad optical lines, while these lines are generally not found in Type-2 sources. Both types show narrow forbidden lines like [NeV] or [OIV] from highly ionized atomic species. While in Type-2 AGN amorphous silicate dust features at  $\sim 10 \mu\text{m}$  and  $\sim 18 \mu\text{m}$  are in general found in absorption, these features have recently been found (Spitzer) in

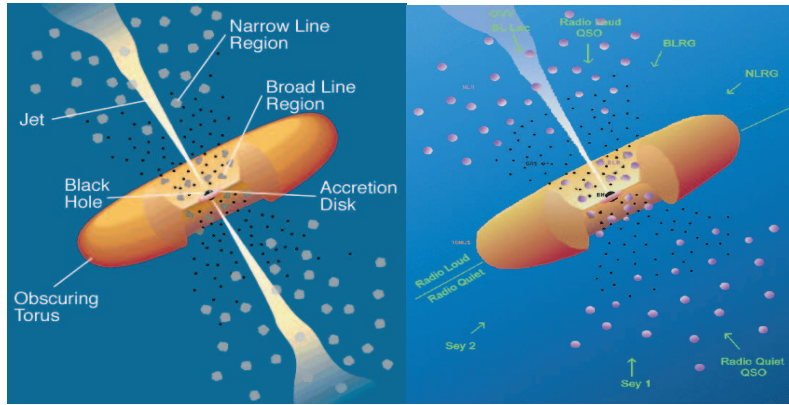


Figure 7.3: Illustration of the AGN Unification Model.

emission in Type-1 sources (Siebenmorgen et al. 2005, Hao et al. 2005). Another difference between the two types is that Type-1 sources show the so called “big blue bump”, which is a pronounced continuum emission peaking in the ultra violet. In Type-2 sources this feature is not directly visible.

One possibility to explain the physical origin of this difference is to assume an obscuring structure surrounding the central bright engine. This structure is often assumed to be an obscuring (possibly clumpy) torus with an inner radius of  $\sim 1$  pc. While in principle the sources are assumed to be the same physical objects, the difference between Type-1 and Type-2 is explained by different line of sight inclinations with respect to the obscuring structure. In this picture Type-1 sources are observed if we have a direct view onto the central engine for face-on geometries. Type 2 sources are observed if we have an edge-on view onto the obscuring torus. This interpretation is called the “AGN Unification Model” (Antonucci 1993), since the variety of observed AGN properties is reduced to just a geometric property. Figure 7.3 illustrates the “AGN Unification Model”.

Following the “AGN Unification Model” Type-1 sources show broad, allowed optical lines, since one has a direct view onto the “Broad Line Region” (BLR). This is a dense region with an extension of  $\sim 1/10$  pc (Kaspi et al. 2005). Due to the vicinity to the black hole, the strong gravitational potential well forces the material to move with high velocities, resulting in a Doppler broadening of the emission lines emerging from this material. In Type-2 sources, the BLR is instead obscured due to the torus, thus explaining the absence of broad emission lines. The same obscuration effect holds true for the “big blue bump”, that is thought to be emission arising from the innermost hot accretion disk surrounding the black hole. The “Narrow Line Region” (NLR) is less dense and located further away ( $\sim 1$  kpc, Bennert et al. 2002, Schmidt et al. 2003) above the obscuring structure. This explains why the narrow lines are observed in both types of sources. For a Type-2 source we have an edge-on view onto the obscuring structure. In this case the emission from the center, has to penetrate the dusty torus, which implies that for Type-2 sources dust absorption features are expected. The opposite is the case for Type-1 sources, where one has a direct view onto the illuminated hot inner surface of the dusty torus. Here the dust is expected to exhibit emission features. The first two publications will treat the silicate dust emission and its

origin in AGN.

## 7.3 The QUEST Project

The 2nd and 3rd publications are part of a large observational program called QUEST (Quasar and ULIRG Evolution Study). They are related to AGN studies using the MIR-spectrometer IRS on board of the Spitzer Space Telescope. QUEST studies in detail the basic physical processes involved in creating massive early type hosts on the one hand, and growing/feeding embedded massive black holes on the other hand, in major merger galaxies. This is important since 50% of cosmic star formation at high- $z$  and most of the big black holes appear to be formed in this process, which still requires a better understanding in a “local laboratory”, in order to apply this knowledge to high redshift. To obtain the maximum amount of information which is needed to resolve the “nature” of the observed astronomical objects, it is necessary to use multiple instruments operating in different wavelength regions. First, one has to understand the structural properties of each galaxy merger as well as the time/phase at which we see it. This information is achievable in the near-IR/optical regime using the Hubble Space Telescope. Then one has to assign to each system the amount of radiation/energy produced in star formation and BH accretion. The key fine-structure line diagnostics can only be obtained from mid-IR spectroscopic data using the Spitzer Space Telescope. To obtain also dynamical information (e.g. the stellar velocity dispersion) for the QUEST sources we use ground based near infrared spectroscopy with the Very Large Telescope (VLT).

QUEST especially addresses the following questions:

- Is it true that massive ellipticals as well as QSO-like ( $> 10^8 M_{sun}$ ) black holes are formed when two big, gas rich galaxies merge (Sanders et al. 1998)?
- How and at what rate during the various stages of the merger are black holes fed and grow in mass?
- Are the resulting black holes typical for QSOs?
- Does merging adhere to the local black hole mass - sigma relationship?

The publications presented in this thesis are more related to an investigation of particular aspects of the AGN physics than to the evolutionary aspects of the QUEST program. Nevertheless, the finding of similar starburst properties in QSOs and ULIRGS (Chapter 10) supports their evolutionary connection.

## 7.4 Data Reduction Tools

An outline of the data reduction procedure for our *Spitzer* data is given in Chapter 10.2.2. This section gives a short introduction to the IDL software tools, developed in the context of this thesis, to process and analyze the *Spitzer* data.

Programs were developed to remove outlying values for individual detector pixels (lhcoaddb.pro, lhdeglitchb.pro) and to fit the QSO spectra with spectral templates (tempfit.pro).

### 7.4.1 Removing Outlying Pixel Values

The detector arrays of the IRS show some degree of permanent and temporary disturbances caused by impacts of particles from the solar-wind and cosmic rays. Some pixels show constant offsets, while other pixels have outlying values only in individual observations. At the time of our *Spitzer* data reduction no software tool was available to account for these outlying values (glitches). Thus we developed a software tool to deglitch the data. An observation consists of multiple cycles taken at two different nod positions along the spectrometer slit. The nodding shifts the spectrum slightly in the spatial direction on the detector array. This is useful to prevent the loss of spectral information due to damaged or offset detector pixels. In addition one can achieve a background correction by subtracting the two nod positions from each other.

Starting from the two-dimensional basic calibrated data (BCD) products our program corrects the outlying values for each cycle of the observation and for a fixed nod position. To identify outlying pixel values within low signal regions we used a  $\kappa_{gl} \cdot \sigma$ -criterion. If the difference between a pixel value and the median of its local neighborhood is larger than  $\kappa_{gl} \cdot \sigma$  the pixel value is replaced with the median value.  $\kappa_{gl}$  is a selectable constant (typically 2-3) and has to be optimized by visual inspection of the resulting spectrum, while  $\sigma$  is the standard deviation of the neighbored pixel values in the spectral direction. In regions of stronger signal we used a different criterion. In these regions it is useful to define a line-to-continuum criterion to identify outlying pixels. This means if a pixel value is larger than the median value of its local neighborhood (in spectral direction) times a selectable constant (lcmn) the pixel value is replaced by the median value. In addition the program allows one to relax the clipping threshold for spectral features, in order to avoid mis-interpreting lines as glitches. One can define a “protection” region around single spectral features. Then another selectable parameter (mult) controls the relaxation of the deglitching threshold within this region. lcmn is multiplied by a factor which is 1 at the edges of the protection region and increases linearly to  $2 \cdot \text{mult}$  at its center.

After the outlying values have been removed, all cycles of one nod position are automatically averaged using again an iterative  $\kappa \cdot \sigma$ -clipping for the individual pixels of each cycle. Using the program SMART (Higdon et al. 2004) we then subtracted the “cleaned” and averaged observations of the two nod positions from each other. Our entire method is an interactive process which requires careful visual inspection. One has to compare the “cleaned” observation with a reference spectrum. The reference spectrum is the averaged observation of one nod position but without any bad pixel removal. This comparison is necessary to find the best parameters ( $\kappa_{gl}$ ,  $\kappa$ , lcmn, mult) and to make sure that spectral features are not affected.

### 7.4.2 Template Fitting

One major goal of our data analysis is to disentangle, identify and quantify the contribution of individual components (star formation, AGN, extinction, absorption features) in our spectra. I developed an IDL program for fitting the observed spectra with a mixture of individual templates, black bodies and power laws. Each component can be subject to individual extinction. Most features of the program are described in Chapter 9, where the program was intensively used to estimate the possible origin of silicate emission observed in PG QSOs. Another forthcoming paper (Veilleux et al. 2008) will use the program to analyze and quantify the contribution of star formation in the IRS spectra of heavily absorbed ULIRGs. The program is based on the IDL routine MPFIT written by C.B. Markwardt<sup>1</sup> that performs a  $\chi^2$  minimization.  $\chi^2$  is defined by

$$\chi^2 = \sum_{\lambda} \left( \frac{F_{\text{obs}}(\lambda) - F_{\text{mod}}(\lambda)}{\text{Err}(\lambda)} \right)^2, \quad (7.1)$$

where  $F_{\text{obs}}(\lambda)$  is the monochromatic source flux and  $F_{\text{mod}}(\lambda)$  is the model flux made of the sum of all selected templates, black bodies and powerlaws. Template spectra can be included in the fit by including their three dimensional data (wavelength, flux density, error of the measurement). The scaling factor of each template is a fit parameter and its start value has to be defined in a control file. The control file contains all the information about the fit components and their start parameters. The program offers the possibility to use black bodies and power laws as fit components. The fit parameters of this components are temperature (black bodies), powerlaw index and the scaling factor. In addition it is possible to mark any fit parameter as fixed. In this case the parameter keeps its pre-defined start value throughout the fit. In general it is possible that certain fit components are extinguished by dust. To account for this possibility there is an additional option to obscure each component individually by screen or mixed extinction. To do this one can include one or more extinction curves. The extinction curves are given as  $\frac{A_{\lambda}}{A_V}$  where  $A_{\lambda}$  is the extinction at the wavelength  $\lambda$  and  $A_V$  is the visual extinction. Screen extinction occurs if a source is covered behind an obscuring screen, while mixed extinction occurs if the emitting sources are mixed with the obscuring material. In the case of screen extinction the following relation is used.

$$I(\lambda) = I_0(\lambda) \cdot e^{-0.4 \cdot A_V \cdot \text{extinctioncurve}(\lambda)} \quad (7.2)$$

Here  $I(\lambda)$  is the observed and extinguished intensity and  $I_0(\lambda)$  the unextinguished, intrinsic intensity of the source at the wavelength  $\lambda$ . The optical depth  $\tau(\lambda)$  can be written as  $\tau(\lambda) = 0.4 \cdot A_V \cdot \text{extinctioncurve}(\lambda)$ .

In the case of mixed extinction another formula is used (Thronson et al. 1990)

$$I(\lambda) = I_0(\lambda) \cdot \frac{1 - e^{-\tau(\lambda)}}{\tau(\lambda)} \quad (7.3)$$

<sup>1</sup><http://cow.physics.wisc.edu/~craigm/idl/idl.html>

where  $\tau(\lambda)$  is defined as before.  $A_V$  is the fit parameter for the extinction in both cases.

To account in addition for possible absorption features (e.g, water-ice absorption) within the single fit components individual absorption features can be included in the fit. The absorption curves are defined as  $10^{\frac{\tau(\lambda)}{\tau_{max}}}$  where  $\tau_{max}$  is the maximum optical depth. One can apply these absorption curves to individual fit components. The program accounts for the absorption by multiplying the regarding template with

$$e^{-\tau_{peak} \cdot \log_{10}(\text{absorptioncurve}(\lambda))}. \quad (7.4)$$

$\tau_{peak}$  is the fit parameter for the absorption features. Taking all possible templates, black bodies, powerlaws, extinction curves and absorption features into account,  $F_{\text{mod}}(\lambda)$  from Equation 7.1 can be written as

$$\begin{aligned} F_{\text{mod}}(\lambda) = & \sum_i A_i \frac{\text{Planck}_i(\lambda, T_i[K])}{\max(\text{Planck}_i)} \cdot \text{ext}_i^{BB}(\lambda) \cdot \prod_j e^{-\tau_{peak(i,j)} \cdot \log_{10}(\text{abs}_{i,j}(\lambda))} \\ & + \sum_k B_k \frac{\nu^{P_k}(\lambda)[\text{Hz}]}{\max(\nu^{P_k})} \cdot \text{ext}_k^{PL}(\lambda) \cdot \prod_l e^{-\tau_{peak(k,l)} \cdot \log_{10}(\text{abs}_{k,l}(\lambda))} \\ & + \sum_m C_m \frac{\text{template}_m(\lambda)}{\max(\text{template}_m)} \cdot \text{ext}_m^{\text{template}}(\lambda) \cdot \prod_n e^{-\tau_{peak(m,n)} \cdot \log_{10}(\text{abs}_{m,n}(\lambda))} \end{aligned}$$

The indices of the sums run over all black bodies (Planck<sub>*i*</sub> with temperature  $T_i$ ), power laws ( $\nu^{P_k}$ ) and templates (template<sub>*m*</sub>).  $A_i$ ,  $B_k$  and  $C_m$  are the scaling factors for each individual fit component. To achieve an easier first guess for this parameters each fit component is normalized to its maximum flux density ( $\max(\text{Planck}_i)$ ,  $\max(\nu^{P_k})$ ,  $\max(\text{template}_m)$ ) within the wavelength range of the fit. If no extinction is applied to any fit component  $\text{ext}_i^{BB}(\lambda)$ ,  $\text{ext}_k^{PL}(\lambda)$  and  $\text{ext}_m^{\text{template}}(\lambda)$  equal 1. Otherwise they refer to the extinction correction as discussed for Equation 7.2 and 7.3 with the fit parameters  $A_{V,i}$ ,  $A_{V,k}$ ,  $A_{V,m}$ . The products run over all absorption features selected for each individual fit component.  $\tau_{peak(i,j)}$ ,  $\tau_{peak(k,l)}$ ,  $\tau_{peak(m,n)}$  are the fit parameters for each individual absorption feature ( $\text{abs}_{i,j}(\lambda)$ ,  $\text{abs}_{k,l}(\lambda)$ ,  $\text{abs}_{m,n}(\lambda)$ ) as discussed for Equation 7.4. If no absorption is selected for any fit component the products equal 1. In summary the fit parameters are  $A_i$ ,  $B_k$ ,  $C_m$ ,  $T_i$ ,  $P_k$ ,  $A_{V,i}$ ,  $A_{V,k}$ ,  $A_{V,m}$ ,  $\tau_{peak(i,j)}$ ,  $\tau_{peak(k,l)}$  and  $\tau_{peak(m,n)}$ .

Weighting as a function of  $\lambda$  is introduced by  $Err(\lambda)$  in Equation 7.1. By using additional software tools one can choose a weighting scheme. For example one could select  $Err(\lambda)$  to be the error of the measurement. But also other weighting schemes are possible as explained in Chapter 9.

The program automatically estimates the wavelength range for the fit. The fit is performed over the largest common wavelength range of the source spectrum, template spectra, extinction curves and absorption curves. The control file offers the additional possibility to choose a different wavelength range by hand.

# Chapter 8

## Silicate Emissions in Active Galaxies - From LINERs to QSOs

E. Sturm, M. Schweitzer, D. Lutz, A. Contursi, R. Genzel, M.D. Lehnert, L.J. Tacconi, S. Veilleux, D.S. Rupke, D. -C. Kim, A. Sternberg, D. Maoz, S. Lord, J. Mazzarella, D.B. Sanders, 2005, ApJ, 629L, 21S

### Abstract

We report the first detection of  $\sim 10$  and  $\sim 18 \mu\text{m}$  silicate dust emissions in a low-luminosity active galactic nucleus (AGN), obtained in Spitzer-IRS 7-37  $\mu\text{m}$  spectroscopy of the Type 1 LINER galaxy NGC 3998. Silicate emissions in AGN have only recently been detected in several quasars. Our detection counters suggestions that silicate emissions are present only in the most luminous AGN. The silicate features may be signatures of a dusty “obscuring torus” viewed face-on as postulated for Type 1 AGN. However, the apparently cool ( $\sim 200$  K) dust is inconsistent with theoretical expectations of much hotter torus walls. Furthermore, not all Type 1 objects are silicate emission sources. Alternatively, the silicate emission may originate in dust not directly associated with a torus. We find that the long-wavelength ( $20 \mu\text{m}$ ) tail of the emission in NGC 3998 is significantly weaker than in the sample of bright QSOs recently presented by Hao et al. The  $10 \mu\text{m}$  profile in our NGC 3998 spectrum is inconsistent with “standard” silicate ISM dust. This may indicate differences in the dust composition, grain size distribution, or degree of crystallization. The differences between NGC 3998, QSOs, and Galactic templates suggest that there are significant environmental variations.

## 8.1 Introduction

In the unifying scheme for active galactic nuclei (AGN) it is postulated that an “obscuring torus” usually surrounds the accreting massive black hole. Models predict that the spectral energy distribution (SED) of a torus depends sensitively on its orientation, geometry, and density distribution (Veilleux 2004, and references therein). In particular, the tori are predicted to exhibit prominent silicate dust features in either absorption or emission, depending on whether an AGN is viewed with the torus edge-on (Type 2) or face-on (Type 1).

Many Type 2 AGN do indeed exhibit silicate absorption features. However, until very recently Type 1 objects have not shown any clear evidence of silicate features, neither in emission nor in absorption (e.g. Clavel et al. 2000). In uniform density torus models with standard dust, suppression of the silicate features occurs for only a very narrow range of model parameters. To account for the non-detections clumpy torus models or tapered disks have been invoked (e.g., Nenkova et al. 2002, Efstathiou & Rowan-Robinson 1995), and larger grain sizes have been postulated (e.g., Laor & Draine 1993; Maiolino et al. 2001a, 2001b).

The Spitzer Space Telescope with its good wavelength coverage and excellent sensitivity allows a more detailed re-investigation of this problem. Siebenmorgen et al. (2005) and Hao et al. (2005) have reported the first detections of prominent silicate emission features in mid-infrared Spitzer-IRS spectra of several luminous quasars. Here, we report the first such detection in a low luminosity AGN, the LINER galaxy NGC 3998. We also comment on detections in more luminous AGN in our sample, with luminosities up to  $10^4$  greater than in NGC 3998.

NGC 3998 is an S0 galaxy at a distance of 14.1 Mpc (Tonry et al. 2001). The optical line ratios are typical of Low-Ionization Nuclear Emission-Line Regions (LINERs). Because of a broad H $\alpha$  component (Ho et al. 1997) NGC 3998 has been classified as a Type 1 object. The 2-10 keV X-ray luminosity of NGC 3998 is  $3 \times 10^{41}$  erg/s (Ptak et al. 2004). A strong UV point source was detected by HST (Fabbiano et al. 1994). The UV source is variable indicating AGN accretion, as opposed to a stellar, energy source (Maoz et al. 2005).

## 8.2 Observations and Data Processing

Our data were obtained with the Spitzer IRS (Houck et al. 2004; Werner et al. 2004) as part of our GO Cycle-1 project on LINERs. For comparison we also consider PG QSOs which are part of our medium size GO Cycle-1 program on Quasar and ULIRG evolution (QUEST; PI: S. Veilleux). The objects were observed in three low and high resolution IRS modules: short low (S0), short high (S1) and long high (S3). Our data reduction started with the two-dimensional BCD products from the Spitzer pipeline (S11). We used our own IDL routines for de-glitching and sky subtraction, and SMART (Higdon et al. 2004) for extraction of the final spectrum.

## 8.3 Results and Discussion

The SED of NGC 3998 is characterized by a well-detected warm continuum with clear broad emission features in the 9 - 13  $\mu\text{m}$  and 15 - 20  $\mu\text{m}$  range (Fig. 8.1). PAH dust emission features are absent. The spectrum also exhibits a number of ionic emission lines (omitted in Fig. 8.1), that will be analyzed elsewhere.

Siebenmorgen et al. (2005) have suggested that the failure to detect silicate emission in AGN in earlier missions could be explained as luminosity dependence, because the only detections so far have been in highly luminous (but apparently faint) quasars. Our detection of a prominent silicate feature in a LINER with an AGN luminosity 4 to 5 orders of magnitude below those of quasars is clear evidence against this hypothesis. Silicate emission can be equally strong in low luminosity AGN (see the comparison in Fig. 8.1). The AGN in which silicate emissions have been reported to date are listed in Table 8.1. This emission is present for a large range of intrinsic 2-10 keV X-ray luminosity. Our QUEST and LINER programs are beginning to provide additional observations. Although only a fraction of these observations have been taken or analyzed so far, these surveys provide an early indication of the prevalence of silicate emissions in AGN. They appear in a majority of our optically selected QSOs (with 2-10 keV X-ray luminosities ranging from  $\approx 10^{43.3}$  to  $10^{44.3}$  erg/s) but in only a small fraction of LINERs (1 out of 10). In many LINERs (but not in NGC 3998) and Seyferts the analysis is complicated by confusion with strong PAH emission, requiring a careful decomposition of the spectra into the various components. This will make determining the prevalence and characteristics of silicate emission challenging.

In Fig. 8.1 we compare NGC 3998 to one of the QSOs (3C273) in the Hao et al. (2005) sample, using their continuum subtracted spectrum. For NGC 3998 we subtracted the continuum by fitting a spline (see Fig. 8.1) through the continuum points in the 7-8  $\mu\text{m}$  and 25-35  $\mu\text{m}$  ranges. Without any further scaling the two spectra are virtually identical in the 10  $\mu\text{m}$  feature, but at wavelengths  $> 20 \mu\text{m}$  they deviate significantly from each other. The other QSO spectra also match the shape of the 10  $\mu\text{m}$  feature but the peak wavelength varies between 10 and 11.5  $\mu\text{m}$ . All are different from NGC 3998 at longer wavelengths.

We now compare the 10  $\mu\text{m}$  profile in NGC 3998 with feature “templates” from various astronomical environments. Figure 8.2a shows a comparison to normal ISM silicate emission (Kemper et al. 2004). Clearly, the normal ISM profile is not a good fit. The ISM silicate profile peaks at  $\sim 9.8 \mu\text{m}$ , and it is narrower than in NGC 3998. Siebenmorgen et al. and Hao et al. try to fit the broadened and shifted profiles by folding ISM dust opacities with steeply rising (cold) Planck functions. However, in NGC 3998 this cannot be the full explanation (Fig. 8.2c). While the relative intensities of the 10/18 peaks in NGC 3998 can be reproduced by such a fit with a temperature of  $\sim 180$  K, the emission in the blue wing of the 10  $\mu\text{m}$  feature and longwards of  $\sim 20 \mu\text{m}$  is significantly over-predicted.

Fig. 8.2a also shows a template spectrum for enhanced grain sizes (van Boekel et al. 2005). An increase in the grain size clearly shifts and broadens the profile. Van Boekel et al. have used such templates to fit silicate emission profiles of young stellar objects (Herbig Be stars). They found that none of the stellar

sources consist of fully pristine dust comparable to that found in the ISM, and that larger grain sizes and/or crystallization due to dust processing are necessary to fit the spectra. In Fig. 8.2b we show a comparison of NGC 3998 with the Herbig Be star HD163296 (Meeus et al. 2001). The shapes of the two  $10\ \mu\text{m}$  profiles match quite well; the emission *peak* in NGC 3998 is shifted towards longer wavelengths, however.

While an increased average grain size of amorphous silicates (olivine, pyroxene) can move the feature as a whole, an increased admixture of crystalline silicates (fosterites, enstatites) would result in an additional, relatively sharp peak at  $11.3\ \mu\text{m}$  and further features at longer wavelengths (e.g. Meeus et al. 2001). Within the S/N limits we do not see clear evidence for such peaks in NGC 3998. We note, however, that other species of crystalline silicates, like clino-pyroxenes, produce weaker discrete features and would also be consistent with the faster decline at  $\sim 18\ \mu\text{m}$  (Wooden et al. 1999).

The feature profile may also be sensitive to the chemical composition. For instance, ISO spectra of carbon-rich environments around red giants revealed strong emission of SiC around  $11.2\ \mu\text{m}$  (e.g. Aoki et al. 1999), which looks very reminiscent of the features studied here. Jaffe et al. (2004) reported a similar blue wing deviation and peak shift in the *absorbed* silicate profile in NGC1068. This indicates that the observed shift of silicate emission may not be purely a temperature effect.

We conclude that, due to dust processing, the dust giving rise to the emission features in these AGN may deviate from pristine galactic ISM dust. Evidence that dust in the circum-nuclear region of AGN has different properties (like larger grain size) than in the Galactic diffuse ISM has been reported earlier (Maiolino et al. 2001a, 2001b). Our conclusion does not depend on the simplified assumption of a single temperature that we made in the fit described above (ISM dust opacities  $\times$  Planck function). We have repeated the fit using a mixture of various Planck functions with cooler and warmer temperatures. Applying a mixture of temperatures rather than a single temperature worsens the fit: the silicon features are broadened even more, such that the mismatch in the blue wing of the  $10\ \mu\text{m}$  feature and the red wing of the  $18\ \mu\text{m}$  feature increases.

The presence of the  $10\ \mu\text{m}$  silicate emission feature over a broad range of AGN luminosities could be taken as evidence for the obscuring torus. However, it is not clear yet whether the silicate emission arises in fact from a face-on torus of the standard unified AGN scenario. Apparently, some AGN have a significant region of optically thin, relatively cool ( $\sim 200\ \text{K}$ ) dust emission with comparable properties in various AGN types. This temperature, though, seems too cold to be explained by a hot inner torus wall, which should emit closer to the sublimation temperature of silicates. Depending on the size and composition of the grains, this is between  $\approx 800$  and  $1500\ \text{K}$  (Kimura et al. 2002). A lower temperature might be the result of a stratification into the torus wall, with cooler dust from deeper layers contributing to the inferred average value. However, as described above, mixing emission components of different temperature makes the fit to the observed feature profiles worse. This preliminary approach needs to be improved by real (3-dimensional) radiative transfer models of the AGN emission,

Object	Type	$z$	$L_{2-10keV}$ [ $10^{43}$ erg/s]
NGC 3998	Liner 1	0.0035	0.03
PG0804+761	QSO	0.0999	29
PG1211+143	QSO	0.0808	5
PG1351+640	QSO	0.0881	
IZw1 (PG0050+124)	RL QSO	0.0611	7.8
3C273 (PG1226+023)	RL QSO	0.158	510
3C249.1 (PG1100+772)	RL QSO	0.312	110
3C351 (PG1704+608)	RL QSO	0.372	

Table 8.1: AGN with silicate emission

before final conclusions can be reached. The case of NGC 3998 with its low AGN luminosity and different SED shape at longer wavelengths compared to QSOs places important new constraints on such modeling.

More indication that the silicate emission may not originate in a (standard) torus is provided by the fact that other Type 1 AGN (e.g. some QUEST QSOs and some QSOs of the Hao et al. sample) do *not* show silicates in emission. Furthermore, obscuring tori may not be present in LINERs at all, given that variable central UV point sources are observed in both Type 1 and Type 2 LINERs (Maoz et al. 2005). In addition, observations of nearby Seyfert galaxies have revealed extended dust emission that is roughly co-spatial with the NLR (e.g. Cameron 1993; Bock et al. 1998; Tomono et al. 2001; Radomski et al. 2003; Packham et al. 2005). The role and influence of this extended component is currently poorly constrained but may be significant, given the absence of a strong Type 1 vs. Type 2 anisotropy in total AGN infrared continua (Lutz et al. 2004). We note that dust temperatures of the order 200 K are fully consistent with observed color temperatures of extended NLR dust (Radomski et al. 2003, Packham et al. 2005). Future results from Spitzer observations of both Type 1 and Type 2 AGN over the entire range of intrinsic luminosity will certainly shed more light on this issue.

This work is based on observations made with the Spitzer Space Telescope, which is operated by the Jet Propulsion Laboratory, California Institute of Technology under NASA contract 1407. Support for this work was provided by NASA through Contracts #1263752 and #1267948 issued by JPL/Caltech (SV, DSR, DCK). AS thanks the Israel Science Foundation for support.

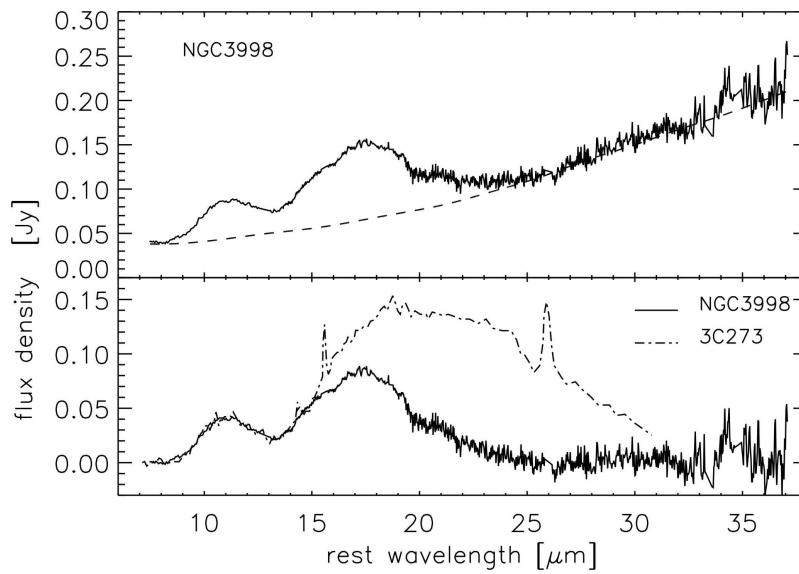


Figure 8.1: *Top*: Combined low and high resolution IRS rest frame spectra of NGC 3998. Narrow emission lines have been omitted. The continuum used for the bottom part of this figure is indicated. *Bottom*: The continuum subtracted spectrum of NGC 3998 compared to the PG QSO 3C273 (from Hao et al. 2005). No scaling has been applied.

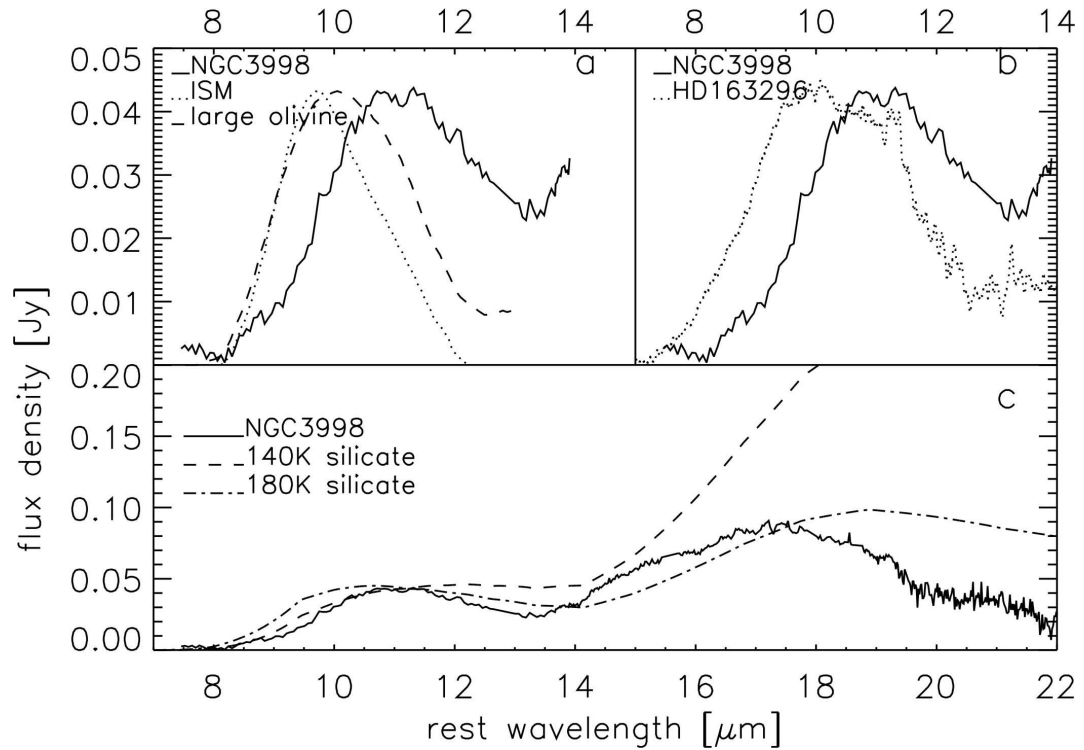


Figure 8.2: (a): Comparison of the NGC 3998  $10 \mu\text{m}$  feature to the standard ISM emission of amorphous silicates (dotted, Kemper et al. 2004), and to olivines of larger grain size (dashed, van Boekel et al. 2005). (b): Comparison to the Herbig Be star HD163296 (dotted, Meeus et al. 2001). (c): Dashed (dash-dotted): the product of a 140K (180K) blackbody and the ISM silicate opacities, produced as in Hao et al. (2005).



# Chapter 9

## Extended Silicate Dust Emission in PG QSOs

M. Schweitzer, B. Groves, H. Netzer, E. Sturm, D. Lutz, A. Contursi, R. Genzel, L.J. Tacconi, S. Veilleux, D.S. Rupke, D. -C. Kim, A.J. Baker, 2008, ApJ, 679, 101S

### Abstract

This paper addresses the origin of the silicate emission observed in PG QSOs, based on observations with the *Spitzer Space Telescope*. Scenarios based on the unified model suggest that silicate emission in AGN arises mainly from the illuminated faces of the clouds in the torus at temperatures near sublimation. However, detections of silicate emission in Type 2 QSOs, and the estimated cool dust temperatures, argue for a more extended emission region. To investigate this issue we present the mid-infrared spectra of 23 QSOs. These spectra, and especially the silicate emission features at  $\sim 10$  and  $\sim 18 \mu\text{m}$ , can be fitted using dusty narrow line region (NLR) models and a combination of black bodies. The bolometric luminosities of the QSOs allow us to derive the radial distances and covering factors for the silicate-emitting dust. The inferred radii are 100-200 times larger than the dust sublimation radius, much larger than the expected dimensions of the inner torus. Our QSO mid-IR spectra are consistent with the bulk of the silicate dust emission arising from the dust in the innermost parts of the NLR.

### 9.1 Introduction

Unified schemes for active galactic nuclei (AGN) postulate an obscuring torus surrounding an accreting super-massive black hole. Models predict that the infrared spectral energy distribution (SED) of the torus depends sensitively on its orientation, geometry and density distribution (e.g., Pier & Krolik 1992; Granato & Danese 1994; Efstathiou & Rowan-Robinson 1995 ; Granato et al. 1997; Nenkova et al. 2002). In particular, the tori are predicted to exhibit prominent silicate dust features in either absorption or emission, depending on whether an AGN is viewed with the torus edge-on (Type 2) or face-on (Type 1). Previous failures

to detect strong  $9.7\mu\text{m}$  silicate emission in Type 1 AGN led to several proposed modifications of the unified model. For example modified grain size distributions have been assumed (Laor & Draine 1993; Maiolino et al. 2001) or a clumpiness of the torus invoked (Nenkova et al. 2002).

The *Spitzer Space Telescope* (*Spitzer*), with its good mid-infrared (mid-IR) wavelength coverage and sensitivity, has drastically changed our view of this problem. Siebenmorgen et al. (2005) and Hao et al. (2005) reported the first *Spitzer* Infrared Spectrograph (IRS) detections of prominent silicate emission features in the mid-infrared spectra of several luminous quasars. Sturm et al. (2005) reported the first detection of 10 and 18  $\mu\text{m}$  silicate emission features in a low-luminosity LINER (NGC 3998). Comparison to the 10/18  $\mu\text{m}$  feature ratio of optically thin emission from silicate dust at different temperatures suggests a modest temperature ( $\sim 200\text{K}$ ) of the emitting dust.

The presence of prominent  $10\mu\text{m}$  silicate emission features in AGN covering a broad range in luminosity could be taken as direct evidence for the existence of an obscuring torus. However, it is not at all clear whether this emission actually arises from the inner regions of a face-on torus. Depending on the size and composition of the grains, sublimation occurs between  $\sim 800$  and  $1500\text{K}$  (Kimura et al. 2002) which is also the temperature range expected for silicate dust located near the hot inner torus wall.

The lower temperature indicated for the emitting silicate dust can be interpreted as evidence for dust emission from regions located further away from the central heating source. Several arguments support such a scenario. Silicate emission has also been detected in Type-2 QSOs (Sturm et al. 2006; Teplitz et al. 2006), whereas for an edge-on view of the torus, one would expect to see silicate in absorption only. An extended emitting region, with dimensions much larger than the inner torus dimension, is fully consistent with this result. Broad-band  $10\mu\text{m}$  imaging of several nearby AGN suggests extended mid-infrared continuum (Cameron et al. 1993; Tomono et al. 2001; Bock et al. 2000; Radomski et al. 2003; Packham et al. 2005). Efstathiou (2006) has modeled the silicate emission of the Type-2 QSO IRASF10214+4724 (Teplitz et al. 2006) invoking extended NLR dust in addition to an AGN torus. Marshall et al. (2007) conclude that some of the optically thin warm emission in the QSO PG0804+761 may emerge from regions beyond the torus and suggest clouds in the NLR as a possible origin of this emission. These arguments indicate that silicate emission may originate in extended regions ( $\sim 100\text{pc}$  dimension).

The nature and location of the extended silicate-emitting region is not yet known. In this paper we explore in a quantitative way one plausible interpretation, namely the association of this cool dust with the NLR. To this end, we present fits of our QSO spectra with a superposition of NLR dust models and spectral components representing the innermost hot dust and the bulk of the inner structure emission (both related to the torus) as well as the large scale host emission. The fitted model and the bolometric luminosity of each source enable us to estimate the cool dust distance and its covering factor. We note that our models cannot exclude the possibility of a torus contribution to the observed silicate emission.

In Section 9.2 we describe our QSO sample. In Section 9.3, we introduce the model components and detail our fitting procedure. We also describe how we estimate the silicate cloud distances and the related covering factors. In Section 9.3.4, we discuss the dependence on model parameters. In Section 9.4, we present the results of the fits, which are then discussed in Section 9.5. Finally Section 9.6 summarizes our conclusions.

## 9.2 The PG QSO Sample

The sources used in our study are part of the *Spitzer* spectroscopy component (PID 3187, PI Veilleux) of the QSO/ULIRG evolutionary study (QUEST). The project and the sample are described in Schweitzer et al. (2006) (hereafter paper I). The QSO sample is largely drawn from that of Guyon (2002) and Guyon et al. (2006). It consists primarily of Palomar-Green (PG) QSOs (Schmidt & Green 1983) and covers the full ranges of bolometric luminosity  $\sim 10^{11.5-13} L_{\odot}$  (based on the absolute  $B$  band magnitude and the SED of Elvis et al. 1994), radio loudness, and infrared excess ( $\nu L_{\nu}(60\mu\text{m})/L_{Bol} \sim 0.02-0.35$ ) spanned by the local members of the PG QSO sample (see also Jester et al. 2005, for a recent view on selection effects in the PG sample). B2 2201+31A is not a PG QSO but is included in the sample because its  $B$  magnitude actually satisfies the PG QSO completeness criterion of Schmidt & Green (1983). The QUEST sample used in this paper includes 23 of 32 objects from the Guyon sample. We add one Palomar-Green object from the Guyon et al. sample previously observed by *Spitzer* (PG0050+124 = IZw1; Weedman et al. (2005)). Table 9.1 lists names and redshifts of all 23 QSOs in our sample, six of which are radio-loud. This sample covers a range from  $M_B = -21$  to  $M_B = -26$ , with median  $M_B = -23.3$ . We assume a cosmology with  $H_0=70\text{km s}^{-1}\text{Mpc}^{-1}$ ,  $\Omega_m = 0.3$  and  $\Omega_{\Lambda} = 0.7$  throughout the paper.

### 9.2.1 Data Reduction

For the QSO sample, spectra were taken both at  $5-14\mu\text{m}$  in the low-resolution (SL short-low) mode and at  $10-37\mu\text{m}$  in the high-resolution (SH short-high and LH long-high) modes of the *IRS* (Houck et al. 2004). Slit widths of 3.6 arcsec to 11.1 arcsec include much of the QSO hosts as well as the vicinity of the AGN. Our data reduction starts with the two-dimensional basic calibrated data (BCD) products provided by version 12 of the *Spitzer* pipeline reduction. We used our own IDL-based tools for removing outlying values for individual pixels and for sky subtraction, and SMART (Higdon et al. 2004) for extraction of the final spectra. Small multiplicative corrections were applied to stitch together the individual orders of the low-resolution and high-resolution spectra, as well as additive corrections for residual offsets still found between the low-resolution spectra and the SH and LH high-resolution spectra after zodiacal light correction of the latter. Paper I discusses in greater detail the *Spitzer* IRS observations and our data reduction procedure.

Object	$z$	$D_L$ Mpc	$\log(L_{5100}/\text{ergs}^{-1})$	radio loud (L)/quiet (Q)
(1)	(2)	(3)	(4)	(5)
PG0026+129	0.1420	672	44.66	Q
PG0050+124 (IZw1)	0.0611	274	44.30	Q
PG0838+770	0.1310	615	44.16	Q
PG0953+414	0.2341	1170	45.11	Q
PG1001+054	0.1605	768	44.25	Q
PG1004+130	0.2400	1203	45.23	L
PG1116+215	0.1765	853	45.13	Q
PG1126-041 (Mrk1298)	0.0600	269	43.82	Q
PG1229+204 (Mrk771)	0.0630	283	44.13	Q
PG1302-102	0.2784	1425	45.17	L
PG1309+355	0.1840	893	44.81	L
PG1411+442	0.0896	410	44.31	Q
PG1426+015	0.0865	395	44.44	Q
PG1435-067	0.1260	590	44.39	Q
PG1440+356 (Mrk478)	0.0791	359	44.22	Q
PG1613+658 (Mrk876)	0.1290	605	44.70	Q
PG1617+175	0.1124	522	44.29	Q
PG1626+554	0.1330	626	44.44	Q
PG1700+518	0.2920	1505	45.68	Q
PG2214+139 (Mrk304)	0.0658	296	44.40	Q
B2 2201+31A	0.2950	1553	45.91	L
PG2251+113	0.3255	1706	45.63	L
PG2349-014	0.1740	840	45.21	L

Table 9.1: QSO sample: Col. (1) — Source name; Col. (2) — Redshift; Col. (3) — Luminosity distance in Mpc for a  $H_0=70\text{km s}^{-1}\text{Mpc}^{-1}$ ,  $\Omega_m = 0.3$  and  $\Omega_\Lambda = 0.7$  cosmology; Col. (4) — Continuum luminosity  $\lambda_{L_\gamma}$  at  $5100\text{\AA}$  rest wavelength (from spectra by T. Boroson, taken from Netzer et al. (2007)); Col. (5) — radio loudness for PG QSOs taken from Sanders (1989) and for B2 2201+31A from Hutchings & Neff (1992)

## 9.3 Modeling the PG QSO IRS Spectra

### 9.3.1 Model Components

We have developed a procedure to fit the spectra of our sources with different components that account for the presence of optically thick AGN-heated dust emission, silicate dust emission and reprocessed stellar emission from the dust in star-forming regions of the host galaxy.

Following recent AGN models (e.g., Siebenmorgen & Efstathiou 2005; Hoenig et al. 2006; Elitzur & Shlosman 2006), we assume a hot dust component located near the central accretion disk that is mainly responsible for the shortest wavelength infrared continuum emission. AGN models typically consider this dust to be located within a torus-like structure. The sublimation temperature for silicate dust grains ranges from 800 K to 1500 K (Kimura et al. 2002). This is also the temperature range expected for dust located at the inner surface of the torus with a typical sublimation radius of roughly  $R_{sub} \simeq 0.5 \cdot \sqrt{L_{bol46}}$  pc, where the bolometric luminosity,  $L_{bol46}$ , is given in units of  $10^{46}$  erg/s (e.g., Barvainis 1987, 1992; Granato et al. 1997; Nenkova et al. 2002, with dependence on grain material and size). To account for this component, we introduce a hot black body spectrum with a temperature restricted to range between 1000 K and 1700 K. To take the temperature distribution within the torus into account as well, we introduce two additional black bodies as fit components (Section 9.3.2) with temperatures between 150 K and 1000 K. In the PG QSOs, these three components represent the bulk of the torus emission. The black body temperatures are free parameters allowed to vary continuously between their specified limits.

The fourth component represents cool dust. As explained in paper I and in Netzer et al. (2007) (hereafter paper II), this component is assumed to be dominated by reprocessed stellar emission from star forming regions in the host galaxy. To account for this component we introduce a cool black body with temperature limited to 35-65 K, a typical range in starburst galaxies. In paper I we demonstrated that on average the 7.7PAH/FIR ratio in our PG QSOs is the same as in starburst dominated, local ULIRGs. This fact indicates similar properties for the star formation in both galaxy types. Hence the assumption of a cool black body (T=35-65 K) to account for the reprocessed stellar emission from star forming regions within the host galaxy is reasonable. We note that the IRS spectra do not include a substantial part of the FIR emission of the QSOs. This limitation tends to shift the inferred best-fit temperature of this component towards higher values. In addition to intrinsic variations of the temperature of starburst dust, this bias is the reason we introduce a limited temperature range for this component.

To account for the contribution of star forming regions to the 4-40  $\mu$ m spectra of our sources, we use the ISO-SWS mid-IR spectrum of M82 (from Sturm et al. 2000) as a starburst template spectrum. In particular, this template is used to fit the broad polycyclic aromatic hydrocarbon (PAH) emission features found in the *Spitzer*-IRS range, which are clearly seen in some of our objects. These features are typical indicators for recent star formation. The ratio of PAH emission to FIR emission in galaxies is related to the average radiation field intensity, echoed

in the 60/100  $\mu\text{m}$  flux ratio tracing the large grain temperature (Lu et al. 2003). By scaling the contribution of the cool black body relative to the contribution of the M82 template, the fitting routine has the freedom to take such a difference between M82 and the PG QSOs into account. Using starburst-dominated ULIRG templates instead of M82 would be an alternative possibility. To exclude ambiguities regarding the power source (AGN or starburst) of the template spectrum, we prefer here to use M82 which, is a well studied, typical starburst galaxy. We have also tested the fits using the starburst template of Brandl et al. (2006). We found no significant differences (in  $\chi^2$  or the contributing components) compared to the fits using the M82 template. This is due to the overall small contribution of the starburst template and the similarity between M82 and the Brandl template. The contribution of the M82 starburst template is found to be consistent with the PAH detections in paper I.

An important new ingredient of the present work is dust emission from the NLR. To fit the silicate emission, which is visible in nearly all of our QSO spectra, we use dust NLR models based on those of Groves et al. (2006). In contrast to torus models, our NLR models account for cooler, optically thin dust that is located further away from the central AGN. The code used to generate these models, MAPPINGS<sub>III</sub>, encompasses all dust-related processes, including stochastic heating, which allows individual small grains to reach high temperatures when heated by energetic photons. For the fits to the IRS spectra, we have removed the line emission in order to concentrate on the IR continuum and the silicate features. The main physics of the AGN IR modeling, including the dust composition and incident AGN spectrum, have been discussed in detail in Groves et al. (2006), and we briefly recapitulate the main parameters here.

In Figure 9.1 we show the incident heating spectrum, which is a fit by Groves et al. (2006) of two power-laws with exponential cut offs to the observations of Elvis et al. (1994). We assume the gas abundances have their solar values (Asplund et al. 2005). Similarly, the dust depletions are based on local measurements (Kimura et al. 2003) for these models (see Table 1 in Groves et al. 2006). We note that the actual metallicities of the QSOs in our sample may be higher, and the actual dust depletions uncertain. The NLR models assume a mixture of siliceous and graphitic dust (Laor & Draine 1993; Draine 1984; Weingartner & Draine 2001) with a grain size distribution arising from a modified grain shattering profile, leading to a smooth exponential cut-off in terms of the grain mass at both ends of the distribution:

$$dN(a)/da = ka^{-3.3} \frac{e^{-(a/a_{\min})^{-3}}}{1 + e^{(a/a_{\max})^3}}, \quad (9.1)$$

with  $k$  defined by the dust-to-gas ratio and  $a$  being the grain size. The minimum and maximum grain sizes are 0.01 $\mu\text{m}$  and 0.25 $\mu\text{m}$  respectively, for both grain types considered. PAHs are assumed to be destroyed within the harsh NLR environment.

In contrast to previous constant-pressure cloud models, we have assumed a constant density structure of  $n(\text{H}) = 10^4 \text{cm}^{-3}$  for simplicity, and explored a range of 13 ionization parameters<sup>1</sup> (incident fluxes) ranging from  $\log U = 1$  to  $-3$  in

---

<sup>1</sup>The ionization parameter is a dimensionless ratio relating the ionizing flux to the particle

Model Number	$\log(U)$	$\log\left(\frac{\text{Incident Flux}}{\text{ergs cm}^{-2} \text{ s}^{-1}}\right)$
1	1.0	5.56
2	0.6	5.16
3	0.3	4.86
4	0.0	4.56
5	-0.3	4.26
6	-0.6	3.96
7	-1.0	3.56
8	-1.3	3.26
9	-1.6	2.96
10	-2.0	2.56
11	-2.3	2.26
12	-2.6	1.96
13	-3.0	1.56

Table 9.2: AGN IR Model Parameters. The NLR models assume a constant density of  $n(\text{H}) = 10^4 \text{cm}^{-3}$  for simplicity.

steps of 0.3 dex (see Table 9.2). These values are typical for NLRs, with  $\log U = 1.0$  being an extreme case, and  $\log U = -3$  becoming too cool to contribute any significant silicate emission. The 13 ionization parameters correspond to the 13 NLR models (see Table 9.2), that will be used later to fit the spectra. The density assumed is on the moderate to high end for NLRs, which are actually likely to be stratified in density (e.g., Groves et al. 2004). However, the assumption of constant density allows us to define accurately the incident ionizing flux, the dominant parameter controlling the dust temperature, and hence the emission. If a lower density of  $n(\text{H}) = 10^3 \text{cm}^{-3}$  is assumed, the general shape of the IR continuum appears the same for a given incident flux. However, the ionization parameter for a given incident flux increases by a factor of 10, resulting in stronger higher ionization lines. The assumed density has no influence on the estimated distances of clouds from the AGN and should be considered as an approximation. In Section 9.5, we will discuss the NLR properties also taking line emission (e.g., [NeV]) into account. Using the line emission, we find that a density of  $n(\text{H}) = 10^4 \text{cm}^{-3}$  is an upper limit for the density of the line emitting region.

As in the Groves et al. (2006) work, we have limited the column density of these models to  $N(\text{H}) = 10^{21.5} \text{cm}^{-2}$ . Fitting the QSO spectra with lower column densities (e.g.,  $N(\text{H}) = 10^{19} \text{cm}^{-2}$ ) leads to unreasonable large covering factors. Using a column density of  $N(\text{H}) = 10^{21.5} \text{cm}^{-2}$  results in a median covering factor of  $\sim 0.16$ . Both the ratio of IR to optical/UV flux and *Hubble Space Telescope* (*HST*) imaging of AGN (Kriss et al. 1992) suggest a  $\sim 30\%$  covering factor as an upper limit for the clouds in the NLR. Increasing the column depth of the NLR models will only affect our results minimally. By a column depth of  $N(\text{H}) = 10^{21.5} \text{cm}^{-2}$ , approximately 70 % of the heating flux has already been

---

density:  $U = \frac{F_{\text{ion}}}{n_{\text{H}}c}$ .

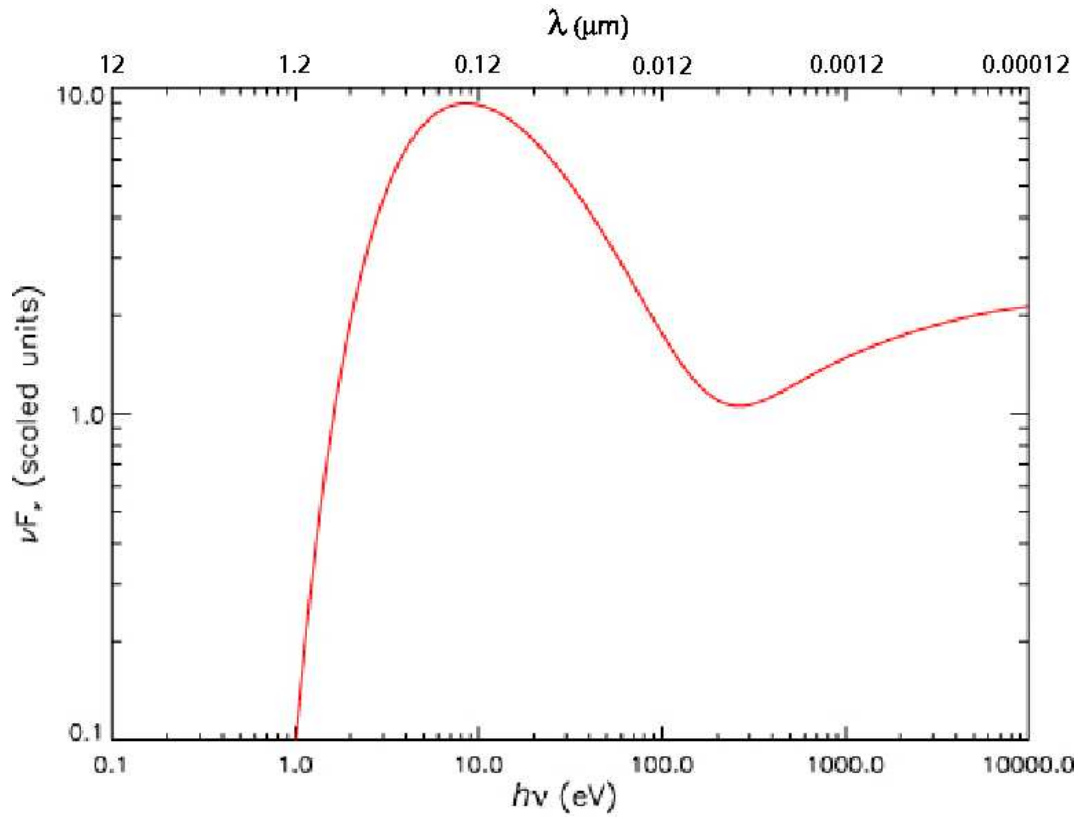


Figure 9.1: Incident accretion disk spectrum from Groves et al. (2006).

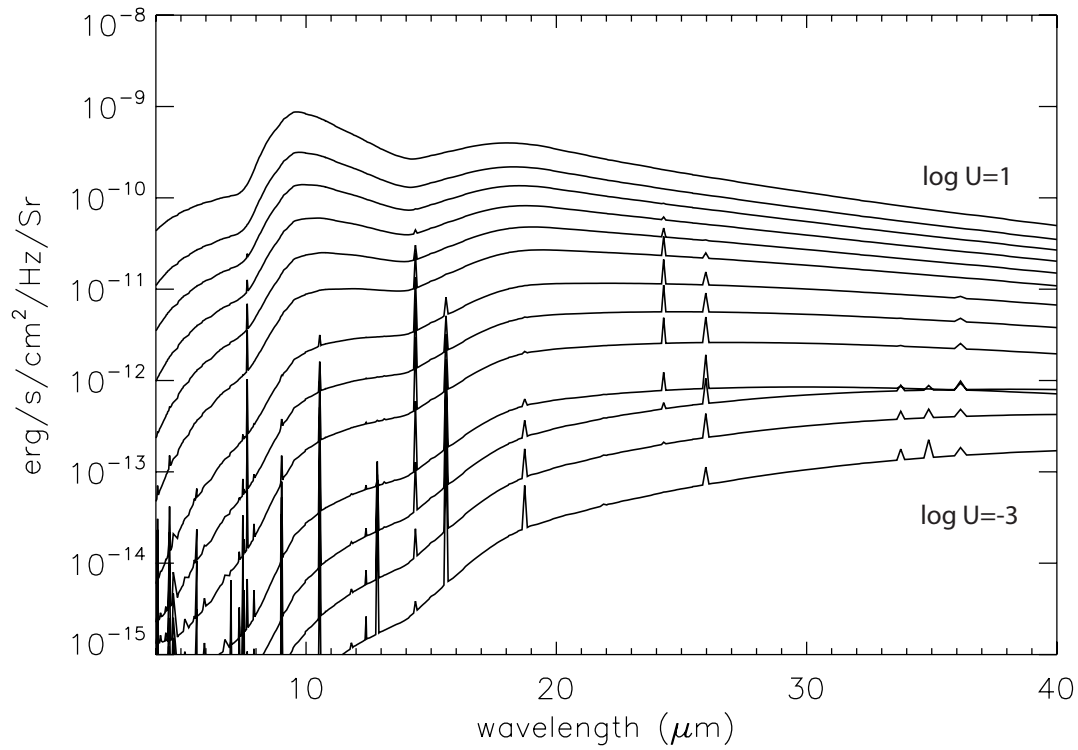


Figure 9.2: Model NLR IR spectra from  $\log U = 1.0$  (top model) to  $-3.0$  (bottom model) in steps of 0.3 dex.

absorbed and re-emitted by gas and dust, meaning that the preponderant shape of the IR emission is already in place. In addition, at larger column depths most of the dust is cool and emits most of its IR flux at wavelengths greater than  $30\mu\text{m}$ , outside the range of the *IRS* spectra.

The resulting nebular IR spectra are presented in Figure 9.2. They show the range in possible silicate emission, as well as the relevant emission lines possible under these conditions assuming the above gas density. We note again that our fits did not include the NLR emission lines, but in Section 9.5 we will discuss the implications for the NLR from a comparison of the modeled and measured line fluxes.

### 9.3.2 Fitting Procedure

To fit the QSO spectra with the components presented in the previous section we developed a template fitting tool based on the IDL routine MPFIT written by C.B. Markwardt<sup>2</sup>. This routine uses the Levenberg-Marquardt technique and we use it here to minimize a modified  $\chi^2$ -value (hereafter called  $\psi^2$ ) defined by

$$\psi^2 = \sum_{\lambda} \left( \frac{F_{\text{obs}}(\lambda) - F_{\text{mod}}(\lambda)}{\text{Err}(\lambda)} \right)^2, \quad (9.2)$$

where  $F_{\text{obs}}(\lambda)$  is the monochromatic QSO flux and  $F_{\text{mod}}(\lambda)$  is the model flux made of the rebinned M82 template spectrum, the four black body spectra and the NLR dust model spectra.

Thus

$$F_{\text{mod}}(\lambda) = \sum_{i=1}^{N_B} a_i \frac{B_i(\lambda, T_i[K])}{\max(B_i)} + \sum_{i=1}^{N_{\text{template}}} b_i \frac{F_i^{\text{model}}(\lambda)}{\max(F_i^{\text{model}})}, \quad (9.3)$$

where  $B_i$  are the Planck functions. All models and template spectra are binned to the IRS spectral resolution of our sources. The first term in  $F_{\text{mod}}(\lambda)$  sums over the four black bodies, while the second sum includes all possible templates (in our case M82 and one (or more) of the 13 NLR models). Each component of the model spectrum is normalized to its maximum within the IRS range and then scaled by a factor  $a_i$  or  $b_i$ . The normalization prevents large variations in these factors. The IRS spectra of our PG QSOs have been fitted using the IRS rest wavelength ranges plotted in Figure 9.5. These ranges vary from source to source depending on the intrinsic redshift of the object.

$\text{Err}(\lambda)$  usually represents the 1-sigma uncertainty on  $F_{\text{obs}}(\lambda)$ , but in our case it is defined in a different way. From tests with different weighting schemes, we found that we best achieved a reasonable weighting and a good fit quality using:

$$\text{Err}(\lambda) = \frac{F_{PL}(\lambda)}{\sqrt{\left(\frac{\Delta\lambda}{\lambda}\right)}} \quad (9.4)$$

<sup>2</sup><http://cow.physics.wisc.edu/~craigm/idl/idl.html>

The flux trend  $F_{PL}$  is from a power law fit to the IRS source spectrum and does not trace individual features. This choice has been made to achieve similar weights for the same relative flux deviations ( $\frac{F_{\text{obs}}(\lambda) - F_{\text{mod}}(\lambda)}{F_{PL}}$ ) at different flux levels  $F_{PL}$ .  $\Delta\lambda$  is the local wavelength sampling density in micrometers. To ensure that better sampled wavelength regions do not dominate the fit due merely to their finer sampling, we estimate  $\Delta\lambda$  using a neighborhood of five wavelength bins at each wavelength, and we make  $Err(\lambda)$  proportional to  $\sqrt{\frac{1}{\Delta\lambda}}$ . The 5-37 $\mu\text{m}$  IRS spectra have spectral resolution varying between  $\sim 60$  at the short wavelength end and  $\sim 600$  at the long wavelength end. Our weighting method ensures a good fit quality over the entire wavelength range while simultaneously being able to fit the PAH emission features located within lower flux regions. To further increase the fit quality at shorter wavelength,  $Err(\lambda)$  is proportional to  $\sqrt{\lambda}$ , which results in a stronger weighting at shorter wavelengths.

As we focus only on the continuum emission, we have removed all emission lines from the original spectra and the NLR models. All lines were cut from the spectra, with the resulting gaps not considered by the fitting routine. We fit each source with one NLR model plus the four black bodies and the M82 starburst template and repeat this procedure for all NLR models. To obtain the best fitting model template ( $F_{\text{mod}}$ ) for each of the NLR models, the contributions of the chosen NLR model and starburst template ( $b_i$ ) and the black bodies ( $a_i$ ) are allowed to vary, as well as the black body temperatures ( $T_i$ ) within their specified limits (i.e., hot: 1700 K-1000 K, warm<sub>1</sub> and warm<sub>2</sub>: 1000 K-150 K and cool: 65 K- 35 K). Finally, for each of our PG QSOs, we determined the best fitting (minimum  $\psi^2$ ) model template out of all the NLR models.

We do not consider the black body spectra used in our fits to be physically meaningful. Instead, they are a reasonable, physically motivated approximation to a smooth underlying continuum, necessary to achieve (in combination with the NLR models) a good fit quality for our spectra. To account for the strong emission found at the shortest wavelengths within the IRS range, we have to introduce a hot continuum component (the hottest black body) for all of our QSO spectra. The limited MIR wavelength range we cover prevents a robust determination of all parameters of this component, since the bulk of its emission is not covered by the IRS range. The same is true for the coolest black body. To achieve a good fit quality, we additionally introduce two black bodies with intermediate temperatures. Using just one black body of intermediate temperature leads to degeneracies within the 10 $\mu\text{m}$  region, with some sources having the  $\sim 10\mu\text{m}$  silicate feature reproduced by the black body instead of the NLR model. To prevent this, we introduce a second intermediate black body, which allows for a smoother underlying continuum emission. Including even more black bodies was not necessary since a satisfying level of fit quality is reached with only the four black bodies. Since we do not interpret the black bodies as real physical components and have only a limited wavelength range, we will not discuss their properties. Note that for some sources, the fitting routine automatically minimizes the contributions of certain fit components. This effect can be most dramatically seen in PG 1626+554, shown in Figure 9.5, for which only two components (one hot black body and one NLR model) contribute to the best fit model.

Beyond our standard fitting procedure, we investigated several alternatives. First, we tested the fits using grey bodies proportional to  $\lambda^{-\alpha}$  with  $\alpha = 0, 1, 2$  instead of black bodies. This change had no significant effect on the fit results ( $\psi^2$ , contributing components) or their interpretation. Next we tested for a non-thermal contribution to the mid-IR spectra of our sources by extrapolating a power-law model (based on radio data from NED) to the MIR. We found that for the radio-quiet objects, the non-thermal contribution is a factor 1000-10000 weaker than the MIR emission at  $10 \mu\text{m}$  and can be neglected. Three of the six radio-loud objects have an implied weak non-thermal contribution at  $10 \mu\text{m}$  at the level of 1-10% of the observed continuum. For the other three radio loud sources (PG1302-102, PG2251+113 and B2 2201+31A), the non-thermal contribution could be significant. These sources have been fitted using a power law, with the two intermediate temperature black bodies removed. We find that including a power law non-thermal component does not change our result, since it provides fairly smooth underlying emission similar to that provided by our black bodies. The identification of our sources as radio loud/quiet is listed in Table 9.1.

The fitting procedure also allows us to use multiple NLR models simultaneously. A comparison between use of one and multiple NLR models is discussed in Section 9.3.4. Additionally our fitting routine allows us to obscure single components by a foreground screen. The possible impact of extinction on our results is discussed in Section 9.3.4.

### 9.3.3 Cloud Distances and Covering Factors

To estimate the NLR cloud covering factors and distances (from the central source) we need to use the intrinsic AGN bolometric luminosity. In this context, we have to discriminate between primary radiation emitted by the accretion disk and secondary radiation like that reprocessed by the torus. For a detailed discussion of the bolometric correction, see paper II. We adopt here a bolometric correction defined by  $L_{bol} = 7 \times L(5100)$ , where  $L(5100)$  is the  $5100\text{\AA}$  rest wavelength continuum luminosity ( $\lambda L_{5100}$ ). As explained in paper II, this choice avoids a double counting problem, since it accounts only for primary radiation and does not include reprocessed dust emission. A larger bolometric correction would imply larger cloud distances and smaller covering factors. The values of  $L(5100)$  adopted here are based on the Boroson & Green (1992) observations, which used a relatively small aperture. Given the high luminosity AGN, the contributions of the host galaxies at this wavelength are negligible. Since the ground-based spectroscopy does not show any indication for a high extinction, the intrinsic  $L(5100)$  and the derived bolometric luminosities cannot be significant larger than the values used in this work. The values of  $L(5100)$  for the 23 sources are listed in Table 9.1.

Given the calculated integrated incident flux  $F_{in}$  (see Tab. 9.2) for the best  $\psi^2$  model, we can obtain the dust cloud distance,

$$R_{\text{dust}} = \sqrt{\frac{L_{\text{bol}}}{4\pi F_{\text{in}}}}, \quad (9.5)$$

This in turn allows us to calculate the required NLR covering factor  $c$  given the NLR dust luminosity:

$$c = \frac{F_{NLR_{fit}}}{F_{R_{dust}}} \cdot \frac{D_L^2}{R_{dust}^2} \quad (9.6)$$

where  $F_{NLR_{fit}}$  is the NLR model flux estimated by integrating the fitted NLR model over the observed IRS wavelength range and  $F_{R_{dust}}$  is the model flux, integrated over the rest-frame wavelength range, at the distance  $R_{dust}$  from the central source.  $D_L$  is the luminosity distance of the source (listed in Tab. 9.1). The distances and covering factors obtained in this way are listed in Table 9.3.

### 9.3.4 Fit Components and Uncertainties

In this section, we discuss the impacts of extinction and the use of multiple NLR components on the fits. We also demonstrate the fit quality by fitting different NLR models to the spectrum of PG1004+130.

#### The Effect of Extinction

All of our Type 1 QSOs show blue continuum emission, indicating a low extinction ( $A_V < 2$ ). Nevertheless, we tested the effect of a line of sight extinction on our fit results. For this we assume a uniform screen with fixed extinction in the range  $A_V = 0 - 5$ . This was applied to the hot and warm black bodies as well as to the NLR models using the extinction curve of Draine (2003). We then repeated the complete fitting procedure using the extinguished black body and model spectra. As expected, small ( $A_V < 2$ ) extinction does not affect the fit results. Using  $A_V = 2.5$  for some sources, the best fitting NLR model became slightly hotter. For the largest ( $A_V = 5$ ) case, we find that, on average, the best NLR model becomes slightly hotter, resulting in a cloud distance lower by a factor of  $\sim 2$ . We assume this factor to be the upper limit on the uncertainty in the estimated distance due to extinction. All fits of the PG QSOs presented in the following sections assume  $A_V = 0$  to match the low observed extinction. For comparison, we also tested the fits with the extinction curve of Chiar & Tielens (2006). In general, the fit quality became worse (larger  $\psi^2$ -values) compared to fits with the curve of Draine (2003), while the best fitting NLR model did not change significantly. Due to the better fit quality, we use the extinction curve of Draine (2003) in the following.

#### The Number of NLR Components

The fitting procedure described in Section 9.3.2 assumes a single NLR component to infer the silicate dust distances and covering factors. Another possibility is contributions from several dusty clouds at different distances from the central source. To test how such a cloud distribution would influence our conclusions, we repeated the procedure using multiple NLR components. The fitting procedure then minimizes the contributions of those NLR components that do not increase the fit quality. The best fitting NLR models derived from this procedure have

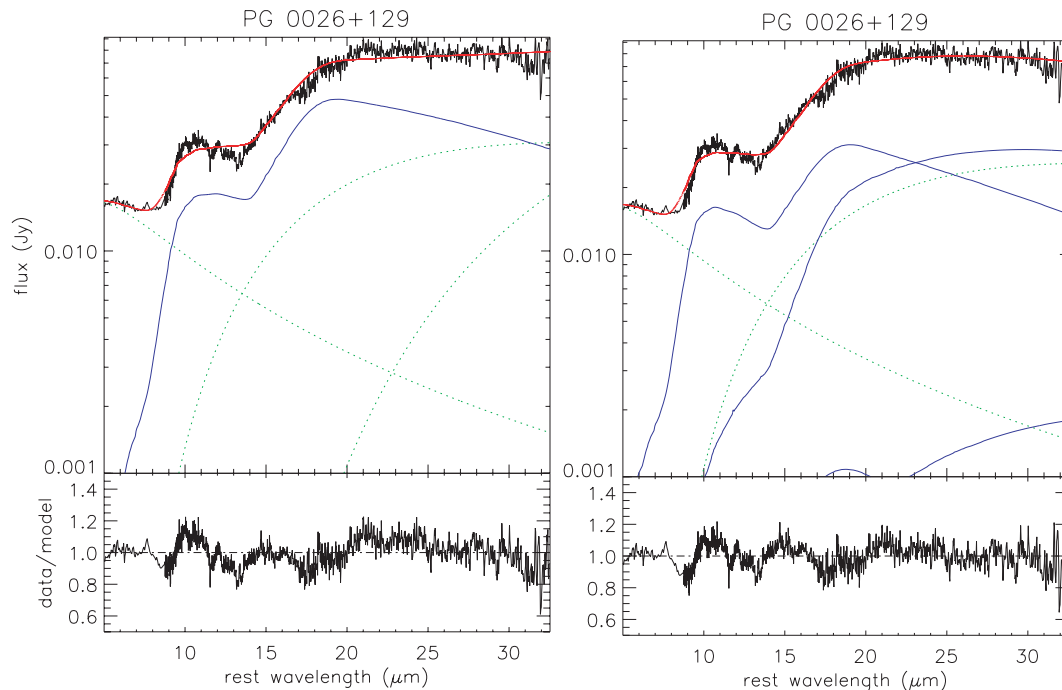


Figure 9.3: Comparison of a single (left) and a multiple NLR model fit (right). In both fits similar cool NLR models produce the silicate emission features. ( NLR model(s) (blue, solid curves); blackbodies (green, dotted curves); total model (red); observed spectrum (black) )

then been compared to the best fit single NLR model of the same source. We found that for most sources, the best fit single NLR model is also the main contributor in the multiple NLR model fit, but this is sometimes accompanied by a second model (with similar  $F_{in}$ ) but a smaller contribution. Also, in some sources the cool black body is replaced by a cool NLR component whose temperature is too low to contribute to the silicate emission. In three sources, the hottest and strongest NLR contributions come from components slightly hotter than those preferred by the single NLR fits. Figure 9.3 shows a comparison between single and multiple NLR fits for PG0026+129. The fit quality as judged by the value of  $\psi^2$  does not change significantly (single model fit  $\psi^2 = 0.0119$  ; multiple model fit  $\psi^2 = 0.0097$ ). In summary, our conclusion of extended silicate emitting dust is independent of the number of NLR components included in the fits. However, we cannot exclude the possibility of smaller contributions from other NLR components.

### Dependence on Cloud Distance

In Figure 9.4 we demonstrate the quality of the fit for PG1004+130, which has been chosen as more or less representative for the whole sample. We compare the best-fit model with two fits using models that differ by a multiplicative factor of  $\sqrt{10}$  in  $R_{dust}$ . Inspection of the residuals shows that these two fits are significantly worse than the best fit model. The mismatch can most clearly be seen at  $\sim 10\mu\text{m}$ ,

where the neighboring models differ significantly from the data. In the lower right panel of Figure 9.4 we show  $\psi^2$  as a function of dust cloud distance for this QSO. It can be seen that  $\psi^2$  is a smooth function with a quite well defined minimum at a dust distance of  $R_{dust}=52$  pc.

## 9.4 Results

In Figure 9.5 we present the best fits for the complete QSO sample. In the top half of each diagram, we show the best-fit model with the observed spectrum. The data are shown in black and the model in red. Also shown are the individual model components: the NLR models (blue, solid curve), the M82 starburst template with PAHs (blue, dashed curve) and the four black bodies in green (dotted). The lower part of each figure shows the fit quality across the spectrum. As can be seen, the fit is satisfactory (within 20% of the flux) for all sources.

Table 9.3 lists the best fitting NLR models for each source in our sample and the estimated cloud distances and covering factors. The cloud distances range from 9 pc (PG 0050+124) to 263 pc (PG 2251+113), with a median value of 40 pc. This is larger than the expected dimension of the inner torus (a few pc; Jaffe et al. 2004). These large radii are compatible with an extended silicate emission region. Since we do not use any torus model in our fits, we are not able to exclude the torus as the origin of the silicate emission. However, we have demonstrated that the NLR is a viable alternative as a source or contributor of the silicate emission. Using the average value of  $F_{in}$  computed from our fits and Eqn.9.5, the average scaling between radius and luminosity is given by:

$$R_{dust} \simeq 80(L_{bol46})^{1/2}pc \quad (9.7)$$

with the bolometric luminosity  $L_{bol46}$  given in units of  $10^{46}$  erg/s. In Figure 9.6, we plot the distribution of the best fit models for the 23 sources. Each NLR model is related to a scaling relationship  $R_{dust} \simeq x \cdot (L_{bol46})^{1/2}pc$ , where  $x$  is the scaling factor. The distribution peaks near  $x = 68$ , which corresponds to model # 5 with an incident flux of  $10^{4.26} \frac{erg}{cm^2s}$  (Tab. 9.2). The model number (#) is a running number (1-13) that identifies the NLR model. With increasing model number the NLR dust model becomes cooler and the scaling factor increases. In Table 9.2, the model number is listed together with the ionization parameter and the incident flux assumed for the respective model. From Figure 9.6, it can also be seen that the hottest model ( $x=15$ ) with the largest incident flux, is never the best fit model. The same holds true for models cooler than model # 9. This indicates that the range of incident fluxes tried here is adequate to fit the dust properties in the NLRs of our 23 QSOs. The range in  $R_{dust}$  defined by the hottest and coolest model is indicated by the dashed lines in Figure 9.7.

The good fits we obtain support the idea that the narrow line region is a possible candidate for hosting the relatively cool silicate dust seen in emission. In Figure 9.7, we plot the estimated dust cloud distances versus the bolometric luminosities of the PG QSOs. The solid line in this plot indicates the sublimation distance for the silicate grains calculated from  $R_{sub} \simeq 0.5(L_{bol46})^{1/2}$  pc (Section

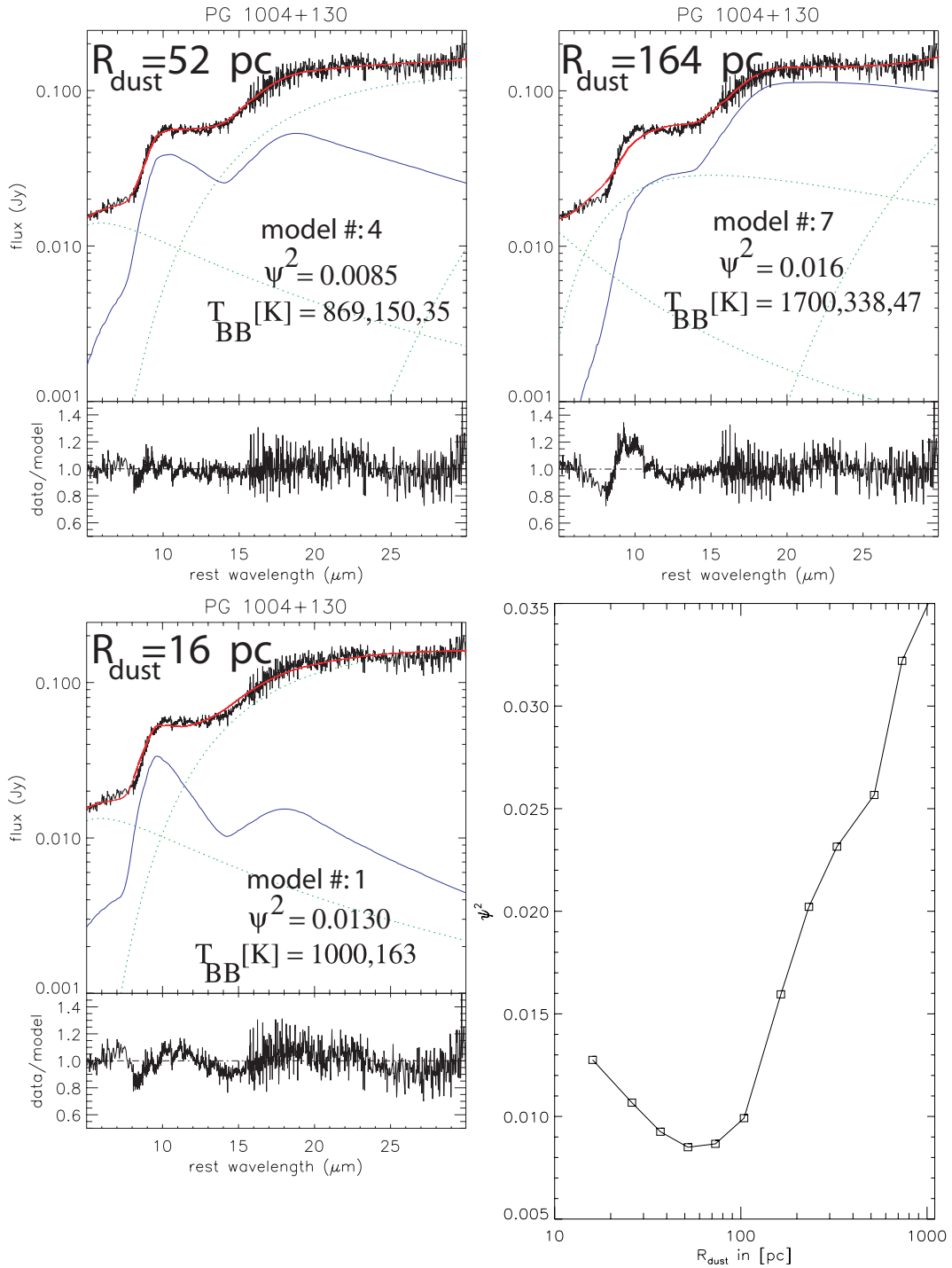


Figure 9.4: Comparison of fit results for PG 1004+130 using the best fit model ( $R_{dust}=52$  pc) or neighboring models differing by  $\sqrt{10}$  in radius ( $R_{dust}=16;164$  pc). Conversion from NLR model to radius is via Eq. 9.5.

9.3.1). Note that we assume here a direct exposure of the silicate grains by the central source. On average we find for the dust distance:

$$R_{dust} \simeq 170R_{sub} \quad (9.8)$$

The dashed lines in Figure 9.7 indicate the distance range covered by our NLR dust models. The typical NLR sizes in our sources are about 5-10 times larger than the largest distances we estimate for the NLR clouds. We refer to Section 9.5.3 for a discussion of the NLR size.

We also compared our results to other known observations. The lower triangle in Figure 9.7 is an upper limit on the torus radius estimated from MIR interferometric observations of the nucleus of the nearby Type 2 AGN, NGC 1068 (Jaffe et al. 2004). The upper triangle indicates the expected silicate dust distance as estimated from our average scaling relation for this source. This example shows that the torus dimension is much smaller than what is expected for the NLR dust cloud distance in an AGN of this particular luminosity. We will discuss this further in Section 9.5.1. The crosses in Figure 9.7 compare our estimate using the average scaling relation (upper cross) for the silicate dust cloud distance in the Type 1 QSO PG 0804+761 with an estimate of Marshall et al. (2007) (lower cross) using a decomposition technique similar to ours. For this comparison, we assumed the bolometric AGN luminosity given in Marshall et al. (2007) of  $L_{bol46} = 0.48$ . For PG 0804+761, the two estimates of  $R_{dust}$  differ by a factor of 2.9 and are in good agreement considering the expected uncertainties and the general scatter of the cloud distances.

The cloud covering factors are listed in Table 9.3. They range from 0.09 (B2 2201+31A) to 0.5 (PG1309+355), excluding PG1001+054 which is the only source with a covering factor of 1.16. This implausibly large value could be the result of the source variation (e.g. S. Kaspi et al. (2000), A. Wandel et al. (1999)) between the epochs of the optical and the *Spitzer* IRS observations. The median covering factor for the full sample, excluding PG 1001+054, is 0.16. In Figure 9.8, we show the distribution of the covering factor excluding PG1001+054.

Table 9.4 presents the contribution of the NLR dust components to the total spectrum in two ways. In the second column, we compare the relative contribution to the 6-25 $\mu$ m rest-frame wavelength range. In the third column, we list the NLR contribution to the 15 $\mu$ m rest-wavelength continuum source flux. The table also shows the relative contribution of the M82 starburst template to the 6-25  $\mu$ m rest-frame wavelength range. The upper limits for this contribution have been calculated by scaling the M82 template to match the  $3\sigma$  upper limits for the 7.7 PAH feature (paper I). The contribution of the starburst template is strongly correlated with PAH strength. Most objects which show clear PAH features in their spectra have a strong M82 contribution (see Fig. 9.5). The median contribution of the NLR dust to the 6-25  $\mu$ m restframe emission is 24 % and the full range is from 15 to 51 %.

In the literature, the strength of the silicate emission in AGN spectra has usually been expressed as an equivalent width of the 9.7 $\mu$ m feature after interpolation of the underlying continuum emission. However, caution is required in using this method, since the possibility of silicate emission hidden by the presence of star

---

formation may bias those estimates. For example, in the fits of PG1440+356 and PG1613+658 in Figure 9.5, it can be seen that this method would result in an underestimate of the silicate strength. The apparent smoothness of the spectrum around  $10\ \mu\text{m}$  is caused by the superposition of starformation related PAH features and a silicate dust contribution that is actually quite strong. To achieve a good estimate for the silicate strength in such composite sources, a decomposition procedure is desirable.

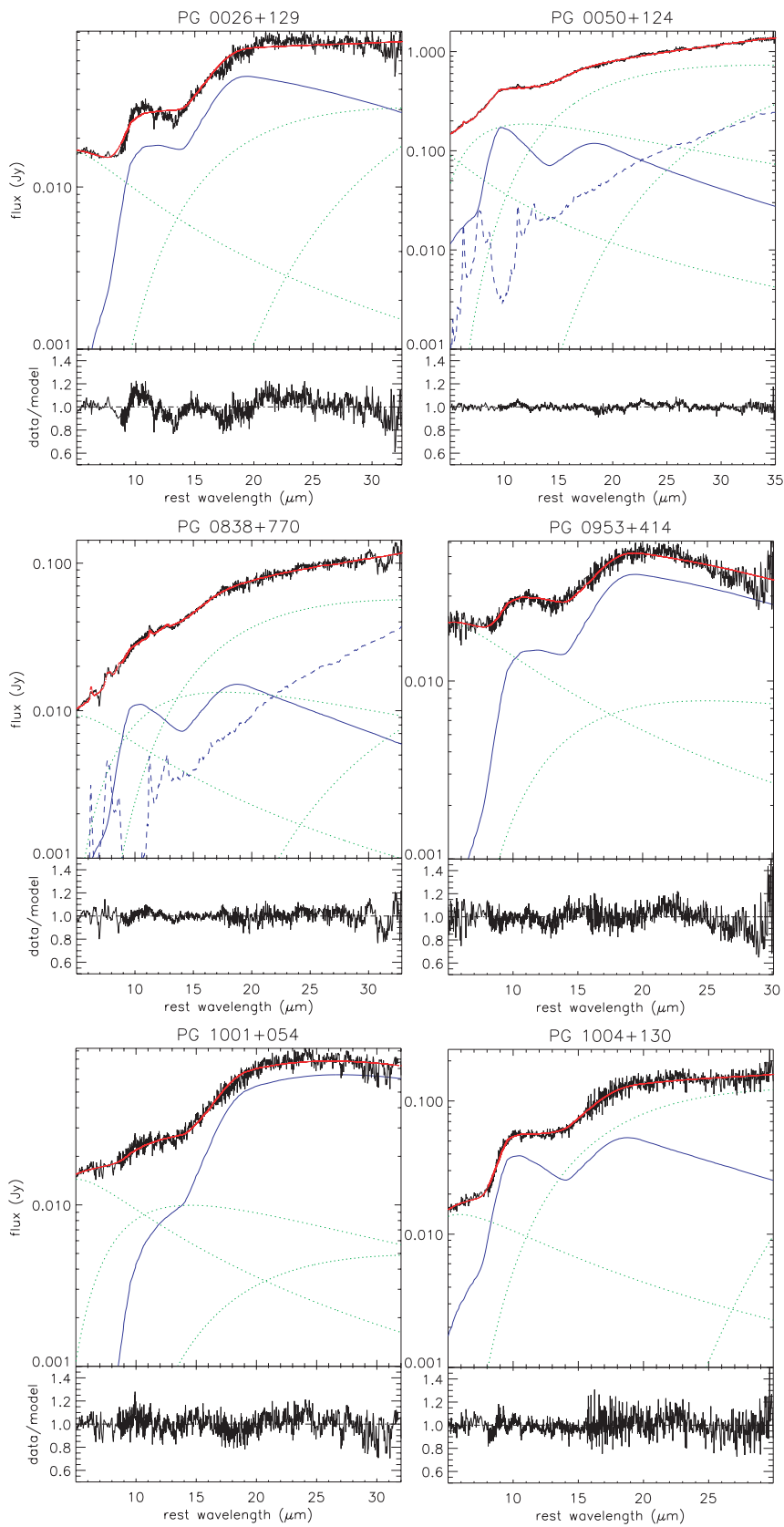


Figure 9.5: fit results: NLR model (blue, solid curve); M82 (blue, dashed curve); blackbodies (green, dotted curves); total model (red curve); observed spectrum (black curve)

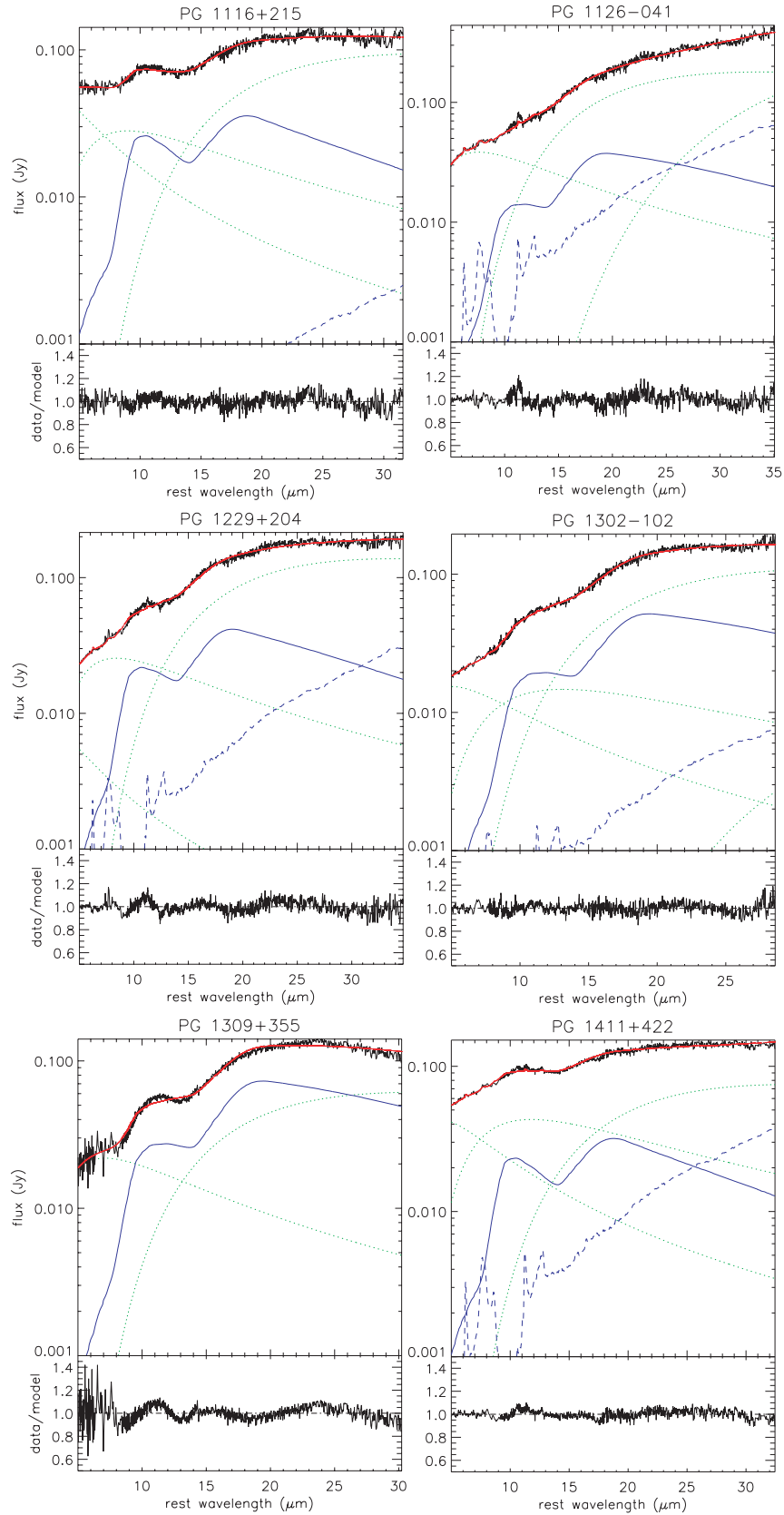


Figure 9.5: continued

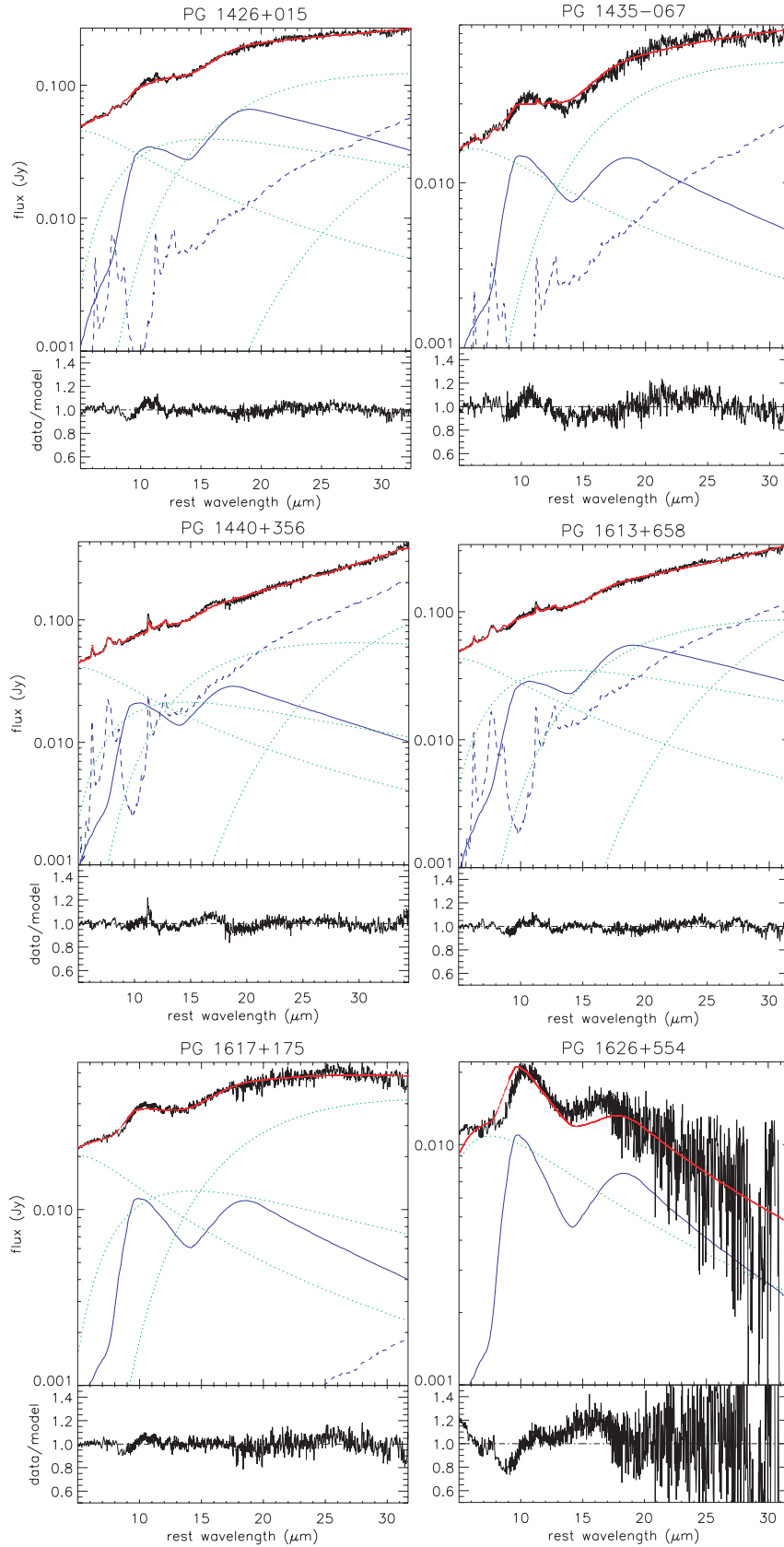


Figure 9.5: continued

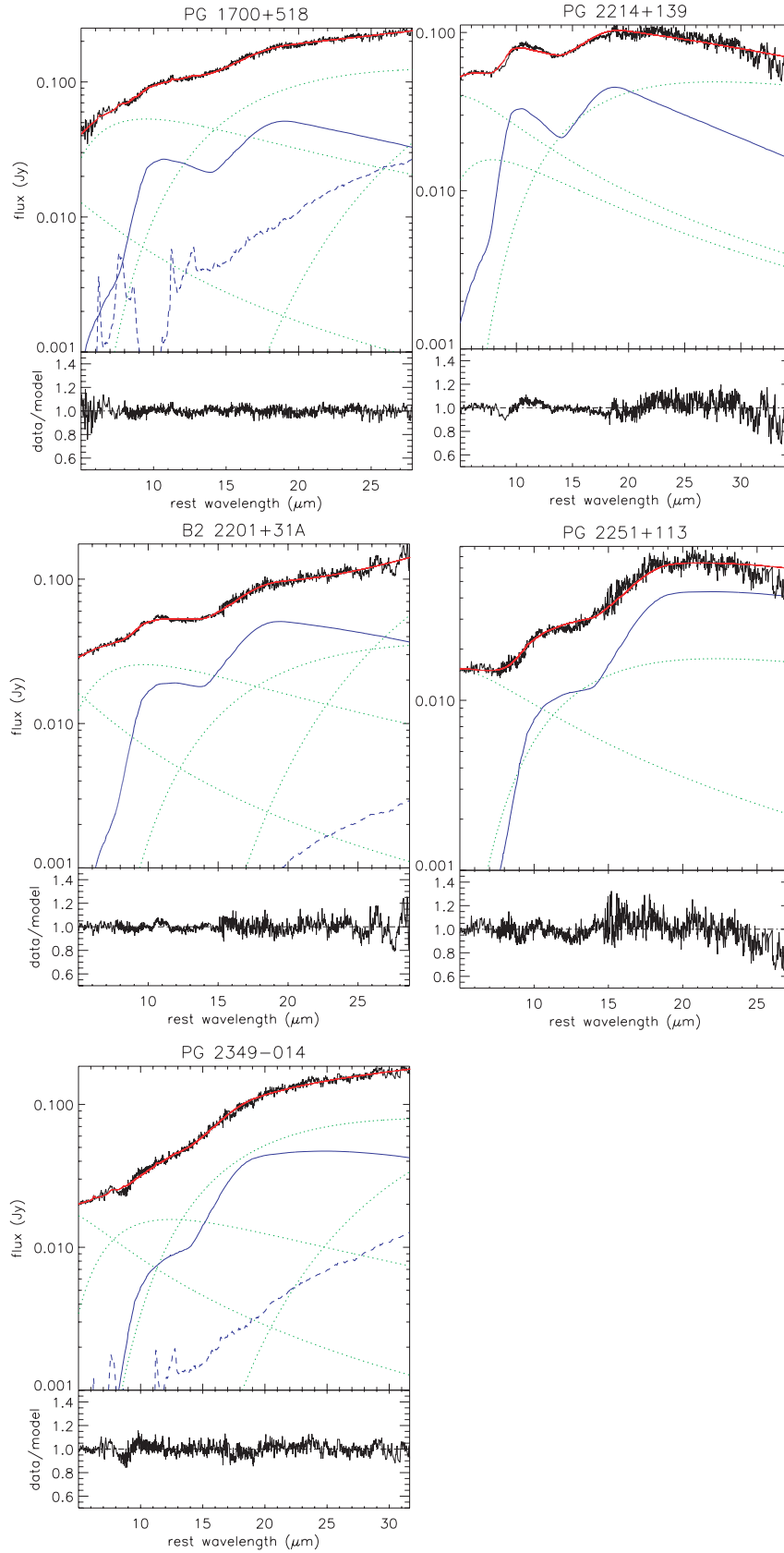


Figure 9.5: continued

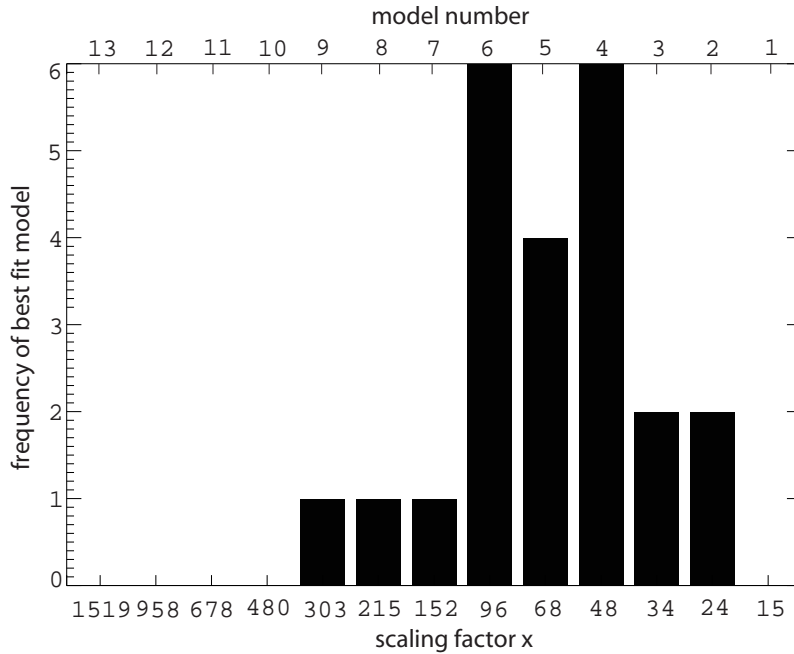


Figure 9.6: Best fit NLR model distribution: Each model is related to a scaling law  $R_{dust} \simeq x \cdot (L_{bol46})^{1/2} \text{pc}$  for the dust cloud distance where  $x$  is the scaling factor and  $L_{bol46}$  the bolometric AGN luminosity in units of  $10^{46} \text{erg/s}$ .

## 9.5 Discussion

We have successfully fitted the MIR *Spitzer* IRS spectra of 23 PG QSOs using cool NLR components to account for the silicate dust emission, in addition to components representing the underlying AGN continuum and the host galaxy's star formation. We have investigated the robustness of the fit results by showing that the fit quality has a clear optimum as a function of NLR model (i.e. distance from the central source, Fig. 9.4), and by probing for the effect of additional foreground extinction even for these optically unobscured Type-1 QSOs. Fitting our spectra with multiple NLR components simultaneously to allow for a dust cloud distribution, we confirm the typical cloud distances derived using one single NLR component but note that we cannot exclude smaller contributions from different components.

Our main result is that the silicate emission may arise in an extended region. The use of NLR models in conjunction with an underlying continuum is already suggestive of a model combining a central compact and hot dust continuum source with silicate-emitting clouds overlapping the NLR. Investigating in more detail the physical implications of the fit results can test this model as well as permit a discussion in the context of other scenarios of AGN dust emission, like more classical torus models or scenarios invoking disk winds (Koenigl & Kartje 1994; Elvis 2000; Elitzur & Shlosman 2006).

Object	Best Fit NLR Model # <sup>2</sup>	$\log\left(\frac{\text{Incident Flux}}{\text{ergs cm}^{-2} \text{s}^{-1}}\right)$	Cloud Distance pc	Covering Factor <sup>1</sup>
PG0026+129	6	3.96	54	0.25
PG0050+124 (IZw1)	2	5.16	9	0.42
PG0838+770	4	4.56	15	0.27
PG0953+414	6	3.96	91	0.23
PG1001+054	9	2.96	107	1.16
PG1004+130	4	4.56	52	0.33
PG1116+215	4	4.56	47	0.14
PG1126-041 (Mrk1298)	6	3.96	21	0.20
PG1229+204 (Mrk771)	5	4.26	21	0.14
PG1302-102	6	3.96	98	0.41
PG1309+355	6	3.96	64	0.50
PG1411+442	4	4.56	18	0.17
PG1426+015	5	4.26	30	0.21
PG1435-067	3	4.86	14	0.17
PG1440+356 (Mrk478)	4	4.56	16	0.14
PG1613+658 (Mrk876)	5	4.26	40	0.24
PG1617+175	3	4.86	13	0.12
PG1626+544	2	5.16	11	0.10
PG1700+518	5	4.26	124	0.15
PG2214+139 (Mrk304)	4	4.56	20	0.10
B2 2201+31A	6	3.96	229	0.09
PG2251+113	7	3.56	263	0.17
PG2349-014	8	3.26	229	0.09

Table 9.3: (1) — estimated covering factor assuming  $H_0=70\text{km s}^{-1}\text{Mpc}^{-1}$ ,  $\Omega_m = 0.3$  and  $\Omega_\Lambda = 0.7$ ; (2) — the model number is a running number (1-13) identifying the NLR model. Larger model numbers correspond to cooler dust (lower incident fluxes). In Table 9.2 the model numbers are listed together with the respective ionization parameters and the assumed incident fluxes.

Object	NLR 6-25 $\mu\text{m}$ %	NLR 15 $\mu\text{m}$ %	M82 6-25 $\mu\text{m}$ %
PG0026+129	51	63	<5
PG0050+124 (IZw1)	19	15	5
PG0838+770	21	19	11
PG0953+414	44	60	<15
PG1001+054	41	46	<8
PG1004+130	44	44	<5
PG1116+215	22	28	<9
PG1126-041 (Mrk1298)	15	17	7
PG1229+204 (Mrk771)	24	25	<4
PG1302-102	29	35	<3
PG1309+355	44	50	<13
PG1411+442	16	19	4
PG1426+015	23	25	5
PG1435-067	29	35	<8
PG1440+356 (Mrk478)	16	15	20
PG1613+658 (Mrk876)	20	24	13
PG1617+175	18	17	<5
PG1626+544	37	38	<9
PG1700+518	19	24	<4
PG2214+139 (Mrk304)	28	34	<3
B2 2201+31A	31	47	<3
PG2251+113	40	54	<5
PG2349-014	22	26	3

Table 9.4: — The total flux is measured across the same wavelength range as for the models. (1) — contribution of the NLR model to the total flux between 6 and 25  $\mu\text{m}$  (rest-frame); (2) — contribution of the NLR model to the total flux integrated between 14.95 and 15.05  $\mu\text{m}$  (rest-frame); (3) — contribution of the M82 template to the total flux between 6 and 25  $\mu\text{m}$  (rest-frame). Upper limits have been estimated from a conversion of the ( $3\sigma$ ) 7.7PAH upper limits presented in paper I.

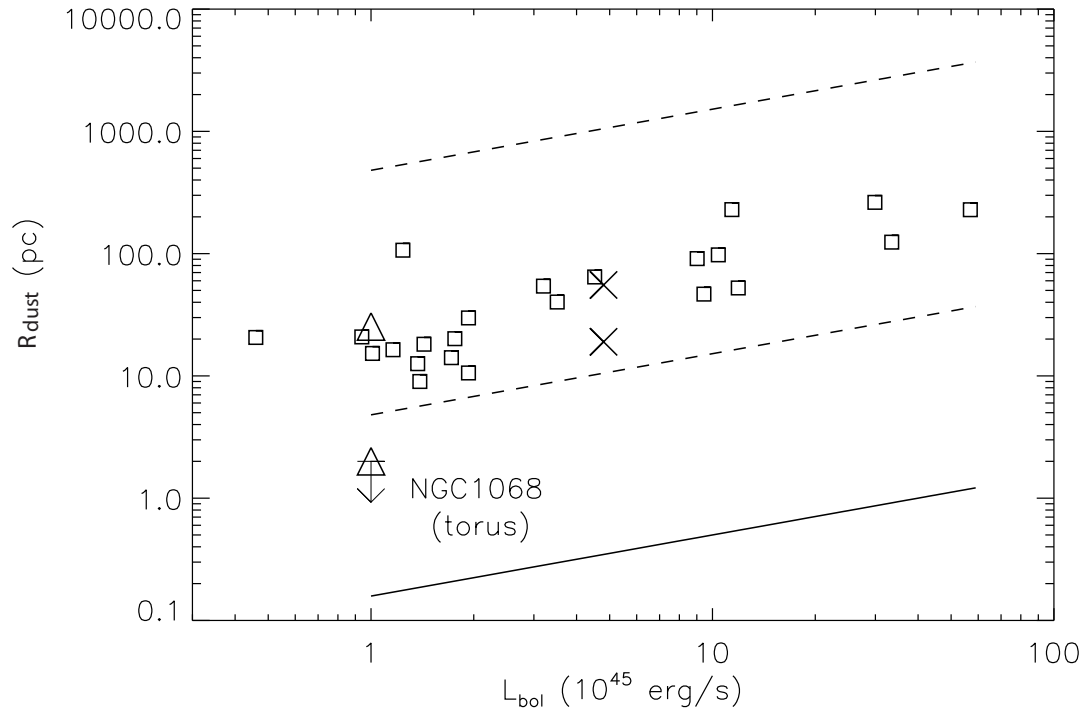


Figure 9.7: Cloud distance versus  $L_{bol}$ , compared to the dust sublimation distance  $R_{sub}$  (solid line). On average,  $R_{dust}$  is 170 times larger than  $R_{sub}$ . The dashed lines indicate the full distance range covered by the NLR models. The triangles indicate the upper limit for the torus size of NGC 1068 (Jaffe et al. 2004) (lower triangle) and the expected silicate dust distance at this AGN luminosity (upper triangle). The two crosses demonstrate the agreement for the silicate dust distance estimates for PG 0804+761 by Marshall et al. (2007) (lower cross) and based on our average scaling relation (upper cross) considering the general scatter of the estimated cloud distances.

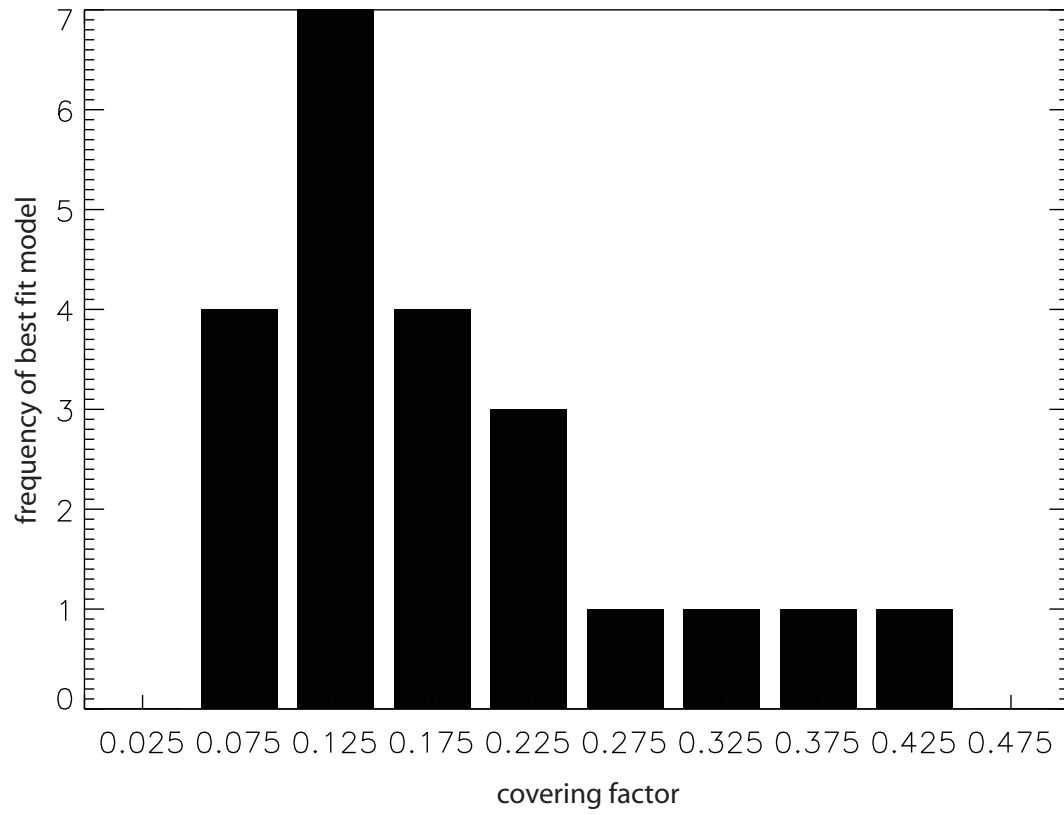


Figure 9.8: Distribution for the derived covering factors (excluding PG1001+054 with a derived covering factor of 1.16). Each bar has a width of 0.05 .

### 9.5.1 Dust Cloud Distances

The dust cloud distances we derive are on average 170 times larger than the dust sublimation distance, which for our PG QSO sample reaches at maximum  $\sim 1$  pc for the most luminous sources. From the distribution of the best fitting NLR models, we estimate an average scaling relation of  $R_{dust} \simeq 80(L_{bol46})^{1/2}$  pc for the cloud-source distance using the expression  $L_{bol} = 7 \times L(5100)$ . The resulting cloud-source distances range from  $\sim 10$  pc to  $\sim 260$  pc. The estimated distances and the good fit quality using our NLR models suggest that the NLR may host the silicate dust seen in emission. Figure 9.6 shows that the best-fit model distribution covers quite a narrow model range. This narrow range is also the reason for the quite small scatter if we plot cloud distance versus bolometric AGN luminosity (Eqn.9.5), as seen in Figure 9.7, and may be one of the most important findings. It reflects the fact that the range of models (and corresponding values of  $F_{in}$ ) that fit the data best is a small sub-set of the total number of models.

Our results are in good agreement with the estimates of Marshall et al. (2007) for the QSO PG 0804+761. These authors used a similar decomposition technique and estimated a silicate dust cloud distance of  $\sim 19$ pc, a factor  $\sim 2.9$  below the  $\sim 55$ pc obtained from our average distance-luminosity scaling relation. As an example, in NGC1068, MIR VLT interferometry (Jaffe et al. 2004) finds compact mid-infrared emission components within  $r \lesssim 2$ pc, which is much smaller than the expected distance of silicate emitting dust for an AGN of this luminosity (see Fig. 9.7), and also much smaller than the additional larger scale emission seen in standard mid-infrared images of this AGN (Cameron et al. 1993; Bock et al. 2000; Tomono et al. 2001). This discrepancy offers additional support for the idea of a separation between the torus and the silicate emission region. Also, the tens of percent of extended mid-infrared emission suggested in this and other mid-infrared imaging studies of nearby Seyferts (Radomski et al. 2003; Packham et al. 2005) are in plausible agreement with the fraction of 6-25 $\mu$ m emission ascribed to the NLR by our fits to PG QSOs (with somewhat higher luminosity). We emphasize that our method does not assume any special geometry. Thus, while we are able to reach reasonable conclusions about the distance of the silicate dust, we cannot derive information about the angular distribution of the dust.

### 9.5.2 Covering Factors

The median covering factor we derive for our QSO sample is 0.16 (excluding PG1001+054), with the overall distribution seen in Figure 9.8. These values agree with other estimates based on narrow emission line imaging and equivalent line width measurements, which suggest NLR covering factors of  $< 30\%$  (e.g., Kriss et al. 1992; Netzer & Laor 1993) We note that in our case, the derived covering factors depend on the assumed column density of our models. For this reason, the covering factor is uncertain due to the uncertainty of the real column density. Fitting our sources with lower column densities than that assumed here ( $N(\text{H}) = 10^{21.5} \text{cm}^{-2}$ ) leads to too large covering factors. On the other hand, increasing the column will only result in a small reduction in covering factor, since most of the incoming flux is absorbed by the dust in a cloud of  $N(\text{H}) =$

$10^{21.5}\text{cm}^{-2}$ . The covering factor is basically determined by the emitted flux of the model. A larger column depth means higher dust absorption and stronger IR emission, which results in a lower covering factor. However, the relationship is not linear due to the change of the dust opacity with wavelength and the cooling of dust at greater depths. Source variability between the epochs of optical and our *Spitzer* observations may introduce another uncertainty. On average, this effect should cancel out, but it may explain the large covering factor (1.16) derived for PG1001+0054. Differences between single and multiple NLR models indicate further uncertainties in the covering factor, since the contribution of each NLR component is somewhat lower in the multiple NLR model fit (the flux in multiple NLR model fits can be shared by similar components).

The distance to the center of the hottest dust is related to the AGN bolometric luminosity via our average scaling relation. If the cloud size is assumed to be constant, then its covering factor would decrease if the cloud is placed further away from the central source. Another possibility is that rather than having discrete clouds, the entire ionization cone could be filled with dust. In this case, the covering factor does not correlate with distance. To test if the covering factor is correlated with the NLR contribution to the total IR flux or the bolometric AGN luminosity, we tested for a correlation between the covering factor and the NLR contribution to the  $15\ \mu\text{m}$  continuum source flux as well as to the total AGN IR luminosity. No such correlation was found. The absence of a correlation may also reflect the uncertainty in our estimate of the covering factor

### 9.5.3 Silicate Emission and NLR Properties

The typical distance found here for the silicate emitting dust is some 170 times larger than the dust sublimation distance and hence much further than assumed in canonical torus models. However, it is also smaller than “typical” dimensions assumed for the NLR. For example, Bennert et al. (2002) have derived a luminosity dependent NLR dimension of roughly  $R(\text{NLR})=2.1L([\text{OIII}]_{42})^{0.5}$  kpc, where  $L([\text{OIII}]_{42})$  is the  $[\text{OIII}]5007\text{\AA}$  line luminosity in units of  $10^{42}\ \text{erg/s}$ . For the sources in our sample, this translates to a typical NLR dimension of 2 kpc (the full range covered in our sample, using this relationship, is about 1-3 kpc). Schmidt et al (2003) later investigated this relationship and found NLR dimensions that are about of factor 2 smaller for sources similar to the ones in our sample. These relationships were also discussed in Netzer et al. (2004) and shown to be inconsistent with dimensions derived for the most luminous AGN. Regardless of the exact value, it seems that the dimensions found here for the silicate emitting dust are 5-10 times smaller than the NLR size derived from the  $[\text{OIII}]5007\text{\AA}$  line luminosity.

We have also looked at the line emission expected from gas clouds situated at the distance of the silicate emitting dust. Observed line fluxes will be published in a forthcoming paper (Veilleux et al. 2008, in preparation). Our continuum fitting procedure can only indicate the cloud distance. The line emission depends on the level of ionization of the gas (the ionization parameter) and hence on the gas density. While a detailed study of the NLR properties in QUEST QSOs

is beyond the scope of the present work, we mention here several of the more important conclusions.

- Assuming a density of about  $10^4 \text{cm}^{-3}$ , gives for the typical incident flux found here, an ionization parameter of about  $10^{-0.5}$ . For this ionization parameter, the high excitation lines of [NeV] at 14.3 and 24.3  $\mu\text{m}$  can reach their observed luminosities, given the covering fractions we derive. However, the observed [NeV]24/[NeV]14 line ratio (typically found to be  $\sim 1$  in our sample) suggests that this density is too high.
- For a lower density gas, of about  $10^3 \text{cm}^{-3}$ , we get the required [NeV] line ratio but the implied ionization parameter is so high that the [NeVI]7.6  $\mu\text{m}$  line is predicted to be much stronger than observed.
- In all cases of  $N < 10^{4.5} \text{cm}^{-3}$ , the gas is too highly ionized to produce the strong observed lines of [OIV] 26  $\mu\text{m}$  and [NeIII] 15.6  $\mu\text{m}$ . These lines can be reproduced for much higher densities (lower ionization parameter) but, in this case, the [NeV] lines are predicted to be well below their observed luminosities.

In short, there is no way to produce all the strong observed NLR lines from a single density component situated roughly at the same distance as the silicate emitting dust. None of these conclusions are very sensitive to the gas metallicity, the exact shape of the ionizing continuum, the relative reddening of optical and IR emission lines, or the exact NLR geometry.

Given this analysis we conclude that the region emitting the strong silicate features cannot represent the entire NLR. It can perhaps be associated with gas in the innermost NLR and the region emitting ‘coronal’ lines from highly ionized species. In this scenario the extended portion of the NLR that produces most of the [OIII]5007 $\text{\AA}$  emission, and probably also the intermediate ionization IR lines like [NeIII] 15.6 and [OIV]26  $\mu\text{m}$ , is of much larger dimensions, perhaps by an order of magnitude or so. All this will be discussed in more detail in a forthcoming paper.

While detailed models designed to fit the IR spectrum of the QUEST QSOs are not yet available, some examples of the above line relationships can be found in the recent Groves et al. (2006) study of the IR spectrum of dusty NLR clouds.

#### 9.5.4 Silicate Emission from Torus Models

Our finding of an extended silicate emitting region does not necessarily contradict torus models, since modified torus models (e.g., Nenkova et al. 2002 - Nenkova, M., Sirocky, M., Ivezić, Z., Elitzur, M., 2007, submitted to ApJ) allow for weak or absent silicate emission within a certain parameter range (e.g., a certain clump distribution). This is also true for some face-on torus models with smooth dust distributions (Dullemond & van Bemmell 2005; Fritz et al. 2006) if certain parameters are assumed. A compact torus might be present and contribute strongly to the MIR continuum but less to the observed silicate emission.

Many of the published torus models cited above predict some level of silicate emission for nearly face-on Type-1 configurations, but often with a higher ratio of the 10 and 18 $\mu$ m silicate features than required by the apparently ‘cool’ dust found in our *Spitzer* spectra. In-depth comparison to the *Spitzer* spectra is needed and ongoing. To our knowledge, the first published result of this type is the fit of *Spitzer*-observed silicate emission features in two Type-1 AGN to a torus model presented by Fritz et al. (2006). These authors assume a flared disk with a continuous dust distribution, whose inner radius is defined by the sublimation radius of the dust, plus host galaxy emission (reprocessed stellar emission from dust in the host galaxy). They account for the different sublimation temperatures of silicate ( $T_{sub}=1000$  K) and graphite ( $T_{sub}=1500$  K) dust grains which can result in a minimum radius for the graphite grains that is up to five times smaller. This difference results in a dust layer composed only of graphite grains, which attenuates the X-ray and UV emission from the central source and is taken into account when the authors compute the silicate minimum radius.

Some of their fits (e.g., for PG1229+204 (Mrk771) and PG 2214+139 (Mrk304)) of Type-1 AGN, which are constrained only by broadband photometry, do not reproduce the silicate emission features observed with *Spitzer* (compare Fig. 9.5). For PG1229+204, their torus model shows silicate in absorption rather than in emission. The same is true for PG2214+139, which shows strong silicate emission features in its *Spitzer* spectrum. These discrepancies suggest that broad band data alone are not able to constrain properly the MIR dust properties, since the wavelength sampling is too low. In contrast, their fits to two Type-1 AGN with MIR *Spitzer* spectra (PG0804+761 and PG1100+772 = 3C249.1) are satisfactory for both the silicate features and the broad band SEDs.

Two elements of the Fritz et al. (2006) models may contribute to this successful fit. First, the separate treatment of graphite and silicate sublimation moves the innermost silicate dust out in radius and behind some shielding graphite-only dust, resulting in cooler temperatures. Results will sensitively depend on the exact values assumed for the sublimation temperatures. Second, the two successful fits to *Spitzer* spectra are characterized by a very steep decrease of the total radial column density from the equatorial plane of the flared disk to its edge. While the column  $N_H$  is several  $10^{23}\text{cm}^{-2}$  on the equator, it is about two orders of magnitude less near the surface. Both factors combined imply a noticeable covering factor by dust with a column of several  $10^{21}\text{cm}^{-2}$  at radii of order 1.2-36pc, with the silicate grains setting in only at  $\sim 5\text{pc}$ . While this still falls short by a fair factor from the radii  $\sim 75\text{pc}$  implied by our scaling relation (for comparison we assume here the bolometric AGN luminosity used in Fritz et al. 2006), it suggests that part of the successful fit by this torus model may be due to a related concept: a moderate column of dust away from the equatorial plane of the torus and well outside the sublimation radius. Their fits to the MIR *Spitzer* spectra of PG0804+761 and especially PG1100+772 are somewhat worse compared to our average fit quality, but we note that our assumed underlying continuum (black bodies) is less physical compared to a proper radiative transfer calculation.

A key challenge for torus models of silicate emission will be to explain silicate emission detected in some clear Type-2 AGNs (Sturm et al. 2006; Teplitz et al.

2006).

The MIR wavelength range is very important for constraining model parameters, since the silicate emission features are very sensitive to dust temperatures, geometries, and density distributions. Salient AGN properties linked to the circum-AGN region include the Type 1/2 ratio and the distribution of obscuring columns as determined from X-rays (e.g., Risaliti et al. 1999) or the optical/near-infrared obscuration of the BLR (e.g., Veilleux et al. 1997; Lutz et al. 2002). Models explaining silicate emission in terms of the torus alone need to fit those as well. A silicate emitting inner NLR of low optical depth, on the other hand, obviously has to be combined with obscuring structures that are plausibly related to the hot continuum in our decompositions. Finally, future high spatial resolution mid-infrared studies through 8m-class diffraction limited imaging, and interferometry with improved sensitivity will be essential to remove remaining ambiguities between the contributions of torus and NLR to the silicate emission.

Finally, while the match between our models and the source spectra is in general good, we find for some sources small deviations between the modeled and observed  $\sim 10 \mu\text{m}$  silicate peak position. Most clearly this can be seen in the fit of PG1626+554, where the observed silicate emission peaks somewhat redward from the modeled  $9.7 \mu\text{m}$  silicate peak. This has already been reported earlier (e.g., Sturm et al. 2005) and may be explained by our physical assumptions, such as the grain size distribution and the exact chemistry of the silicate grains.

## 9.6 Conclusions

Scenarios based on the unified model suggest that silicate emission in AGN arises mainly from the illuminated faces of the clouds in the torus at temperatures near sublimation. However, detections of silicate emission in Type 2 QSOs, and the estimated cool dust temperatures, argue for an origin in a more extended region. To investigate this issue, we have presented the *Spitzer*-IRS spectra of 23 QSOs. We have matched physically-based models to the mid-infrared spectra and found that the silicate emission observed in these objects can be reproduced by emission from clouds, outside the central torus. This extended silicate-emitting region is possibly associated with the innermost NLR region or the intermediate dusty region proposed by Netzer & Laor (1993).

The dust cloud distances found here scale with the AGN luminosity as  $R_{dust} \sim 80 \cdot L_{bol46}^{0.5}$  pc, with the bolometric luminosity  $L_{bol46}$  given in units of  $10^{46} \text{ ergs}^{-1}$ . We have estimated the median distance of the dust cloud responsible for the silicate emission to be 40 pc, while for individual sources distances up to 260 pc are possible. The smallest cloud distance is 9 pc for PG 0050+124. The calculated covering factors for the dust clouds have a median of 0.16 and are in agreement with an NLR origin of the silicate emission.

Our models do not exclude the possibility of a torus contribution to the observed silicate emission, but rather emphasize the good agreement and perhaps the necessity of a larger-scale contribution to this emission.

Finally, future high spatial resolution infrared observations and further cross-checks including the comparison to Type 1/2 ratios as well as distributions and

individual values for the obscuring columns in X-rays and the near infrared are needed to resolve the remaining ambiguities between torus and NLR emission.

Acknowledgements: We thank Tod Boroson for kindly allowing us to use his optical data for PG QSOs.

Funding for this work has been provided by the Israel Science Foundation grant 232/03. H. N. acknowledges a Humboldt Foundation prize and thanks the host institution, MPE Garching.

This research has made use of the NASA/IPAC Extragalactic Database (NED) which is operated by the Jet Propulsion Laboratory, California Institute of Technology, under contract with the National Aeronautics and Space Administration.

This work is based on observations carried out with the *Spitzer Space Telescope*, which is operated by the Jet Propulsion Laboratory, California Institute of Technology, under NASA contract 1407. Support for this work was provided by NASA through contract 1263752 (S.V.) issued by JPL/Caltech.

# Chapter 10

## *Spitzer* Quasar and ULIRG Evolution Study (QUEST): I. The Origin of the Far Infrared Continuum of QSOs

M. Schweitzer, D. Lutz, E. Sturm, A. Contursi, L.J. Tacconi, M.D. Lehnert, K. Dasyra, R. Genzel, S. Veilleux, D.S. Rupke, D. -C. Kim, A.J. Baker, H. Netzer, A. Sternberg, J. Mazzarella, S. Lord, 2006, ApJ, 649, 79

### Abstract

This paper addresses the origin of the far-infrared (FIR) continuum of QSOs, based on the Quasar and ULIRG Evolution Study (QUEST) of nearby QSOs and ULIRGs using observations with the *Spitzer Space Telescope*. For 27 Palomar-Green QSOs at  $z \leq 0.3$ , we derive luminosities of diagnostic lines ([Ne II]  $12.8\mu\text{m}$ , [Ne V]  $14.3\mu\text{m}$ , [O IV]  $25.9\mu\text{m}$ ) and emission features (PAH  $7.7\mu\text{m}$  emission which is related to star formation), as well as continuum luminosities over a range of mid- to far-infrared wavelengths between 6 and  $60\mu\text{m}$ . We detect star-formation related PAH emission in 11/26 QSOs and fine-structure line emission in all of them, often in multiple lines. The detection of PAHs in the average spectrum of sources which lack individual PAH detections provides further evidence for the widespread presence of PAHs in QSOs.

Similar PAH/FIR and [NeII]/FIR ratios are found in QSOs and in starburst-dominated ULIRGs and lower luminosity starbursts. We conclude that the typical QSO in our sample has at least 30% but likely most of the far-infrared luminosity ( $\sim 10^{10...12}L_{\odot}$ ) arising from star formation, with a tendency for larger star formation contribution at the largest FIR luminosities.

In the QSO sample, we find correlations between most of the quantities studied including combinations of AGN tracers and starburst tracers. The common scaling of AGN and starburst luminosities (and fluxes) is evidence for a starburst-AGN connection in luminous AGN. Strong correlations of far-infrared continuum

and starburst related quantities (PAH, low excitation [NeII]) offer additional support for the starburst origin of far-infrared emission.

## 10.1 Introduction

The infrared properties of luminous active galactic nuclei (AGN) and ultraluminous infrared galaxies (ULIRGs) hold clues for the understanding of galaxy formation, the star formation history of the universe and the connection between black hole and galaxy formation and evolution. Physical insight into the co-evolution of AGN and star formation can be gained by study of the low redshift members of these populations. The Infrared Astronomical Satellite (*IRAS*) and the Infrared Space Observatory (*ISO*) have allowed the first comprehensive far-infrared (FIR) studies of extragalactic sources and some high quality mid-infrared (MIR) observations on the brighter sources (see e.g. the review of Genzel & Cesarsky 2000). Issues discussed in *IRAS* and *ISO* studies include the nature of ultraluminous infrared galaxies and their starburst and AGN energy sources (Genzel et al. 1998; Klaas et al. 2001), and the SEDs of QSOs and their evolutionary implications (Haas et al. 2003). A 2.5 to 45  $\mu\text{m}$  spectral inventory of starburst and AGN prototypes (Sturm et al. 2000) and detailed mid-infrared spectroscopic investigations of local lower luminosity AGN (Clavel et al. 2000; Sturm et al. 2002, hereafter S02) have addressed AGN unification and the starburst-AGN connection.

The *Spitzer Space Telescope* (hereafter *Spitzer*) has enabled us to build upon previous work with significantly improved sensitivity. This work is part of a series of papers describing the results of the Quasar and Ulirg Evolution Study (QUEST), focussing on mid-infrared spectroscopy of a sample of 54 QSOs and ULIRGs at redshifts  $z \leq 0.3$  with the Infrared Spectrograph *IRS* onboard *Spitzer*. The sample was selected with the aim of investigating the possible connections between those two groups of luminous ( $L_{\text{Bol}} \geq 10^{12} L_{\odot}$ ) objects in the nearby universe, and is closely connected to optical and near-infrared studies of the morphology and dynamical properties of these two populations (e.g., Dasyra et al. 2006a,b; Veilleux et al. 2006). The purpose of the present paper is to study starburst signatures in QSO host galaxies and to show that most, and in some cases all, of the far-infrared luminosity in QSOs showing strong PAH features is due to starburst activity. A forthcoming complementary paper addresses the spectral energy distribution (SED) of QSOs including the clear far-infrared starburst contribution to the  $\lambda > 30\mu\text{m}$  continuum of QSOs.

To investigate the link between AGN activity and star formation and the extent to which they occur simultaneously, it is important to quantify the star formation activity in QSO hosts. Such measurements are made difficult, however, by the observational problems of detecting star formation tracers in the presence of extremely powerful AGN emission. SED studies based on the *IRAS* and *ISO* space missions have established QSOs as sources of (sometimes) strong far-infrared emission. (e.g., Neugebauer et al. 1986; Haas et al. 2003). In addition to a nonthermal continuum that is detectable in the infrared only in flat spectrum radio-loud QSOs (e.g., Haas et al. 1998), a strong far-infrared emission component is often observed, at varying levels with respect to the strong AGN

mid-infrared continuum. Due to its steep falloff in the submillimeter regime, the origin of this far-infrared emission must be thermal emission of optically thin dust (Chini et al. 1989; Hughes et al 1993). While the warmer  $T \sim 200\text{K}$  dust, which dominates the mid-infrared SEDs of QSOs, is generally accepted to be predominantly AGN heated, there is still considerable dispute about the origin of the cooler  $T \sim 50\text{K}$  emission often dominating the far-infrared. Direct heating by the powerful AGN, but at distances ensuring sufficiently low temperatures, is one possibility (e.g., Sanders et al. 1989; Haas et al. 2003; Ho 2005). Other models prefer an origin in vigorous star formation in the QSO host (e.g., Rowan-Robinson 1995). Rowan-Robinson (1995) used radiative transfer modelling to infer an SED of AGN heated dust that, in  $\nu L_\nu$  units, peaks in the mid-IR and decays towards the far-infrared, a feature shared by many other such models. In the QSO SEDs that are often flat over a wide wavelength range including the far-infrared, the far-infrared component is then plausibly ascribed to a component with an SED similar to that of a star-forming galaxy, in accordance with evidence for coexistence of star formation and AGN in spatially resolved lower luminosity AGN. Rowan-Robinson (1995) found a tight correlation of AGN optical emission and mid-infrared continuum and a weaker correlation between optical and far-infrared emission, which is supporting the view that the far-infrared does not result directly from AGN heating but that there is a connection between AGN and starburst luminosities in the QSOs.

Our goals are to quantify star formation in QSO hosts and to estimate its contribution to the the far-infrared emission. In the mid-infrared, the contrast between the emission from possibly dust-obscured star formation and from the central AGN is favourable, and established star formation tracers are available. We use two such tracers:

(1) The mid-infrared broad aromatic ‘PAH’ emission features arise in regions of the interstellar medium of a galaxy where their aromatic carriers are present, and where their transient excitation is made possible by a non-ionizing ( $< 13.6\text{eV}$ ) soft UV radiation field. This is the case in the photodissociation regions (PDRs) that accompany Galactic star formation regions (e.g., Verstraete et al. 1996), as well as in the diffuse interstellar medium where they are excited by the general interstellar UV radiation field that has leaked from its OB star origins to large scales (e.g., Mattila et al. 1996). PAHs have been used as a quantitative tracer of star formation in galaxies (e.g. Genzel et al. 1998; Foerster Schreiber et al. 2004; Calzetti et al. 2005). Metallicity above 0.2 solar is a prerequisite for strong PAH emission (Engelbracht et al. 2005), a condition that is probably safely met for local QSO hosts. Destruction of the PAH carriers in energetic environments but survival in starburst PDRs (though not in H II regions proper) is key for the use of PAH features as diagnostic. The PAH features are absent from the hard radiation environment of AGNs according to both empirical (e.g. Roche et al. 1991; Le Floc’h et al. 2001; Siebenmorgen et al. 2004a) and theoretical (Voith 1992) studies. The latter suggest that PAH molecules hit by single energetic EUV/X-ray photons can be efficiently destroyed by photo-thermo dissociation or Coulomb explosion. Since AGN are copious emitters of hard photons, PAH molecules near AGN will be destroyed unless shielded by a large obscuring column.

(2) The low excitation fine-structure emission lines like [Ne II]  $12.8\mu\text{m}$  are among the dominant emission lines of HII regions. Observations of starburst galaxies, as well as a combination of evolutionary synthesis and photoionization modelling, show [Ne II]  $12.8\mu\text{m}$  to be stronger than higher excitation mid-infrared lines ([Ne V], [O IV], [Ne III]) in typical ionized regions excited by young stellar populations (Thornley et al. 2000; Verma et al. 2003). Use of low excitation lines as star formation tracers requires, however, the consideration of possible contributions from the AGN Narrow Line Region (NLR) which can be significant despite the generally higher excitation of such regions (e.g., Spignolio & Malkan 1992; Alexander et al. 1999) compared to starburst H II regions.

Section 10.2 of the paper describes the sample, observations and data reduction used to obtain the line and continuum fluxes in our sources. Emission lines that are relevant to the present study are tabulated for all sources. In Section 10.3 we discuss the widespread presence of PAH emission and its relation to other components of the QSO spectra. Finally, Section 10.4 addresses the issue of star formation in host galaxies of QSOs, shows the importance of this process and compares our results with earlier findings. In a forthcoming paper, we discuss the implications of our results for QSO SEDs in general. We adopt  $\Omega_m = 0.3$ ,  $\Omega_\Lambda = 0.7$  and  $H_0 = 70 \text{ km s}^{-1} \text{ Mpc}^{-1}$ .

## 10.2 The QUEST PG QSO Sample: Observations and Reduction

### 10.2.1 The Sample

As part of the *Spitzer* spectroscopy project QUEST (PID 3187, PI Veilleux) we are studying QSOs, ultraluminous infrared galaxies, and the possible evolutionary connection between the two using the infrared spectrograph *IRS* (Houck et al. 2004). The QSO sample is largely drawn from that of Guyon et al (2002) and Guyon et al. (2006). It consists of Palomar-Green (PG) QSOs (Schmidt & Green 1983) and covers the full ranges of bolometric luminosity ( $\sim 10^{11.5-13} L_\odot$  based on the B band absolute magnitude and the SED of Elvis et al. 1994), radio loudness, and infrared excess ( $\log(\nu L_\nu(60\mu\text{m})/L_{\text{Bol}}) \sim 0.02-0.35$ ) spanned by the local members of the PG QSO sample (see also Jester et al. 2005, for a recent view on selection effects in the PG sample). B2 2201+31A is not a PG QSO but is in the sample because its B magnitude actually satisfies the PG QSO completeness criterion of Schmidt & Green (1983). It is one of the five radio-loud systems in our sample. At the sample's maximum redshift of 0.325, important emission lines like [O IV]  $25.89\mu\text{m}$  stay within the IRS spectral range for all objects. The QUEST sample used in this paper includes 23 of 32 objects from the Guyon sample. We exclude here two recently observed QUEST objects that are not yet fully processed by the *Spitzer* pipeline. We add two Palomar-Green objects from the Guyon et al. sample previously observed by *Spitzer* (PG0050+124 = IZw1; Weedman et al. (2005) and PG0157+001 = Mrk1014; Armus et al. (2004)) and two PG QSOs from another project (PID 20241, PI Lutz). Table 10.1 lists

names and redshifts of all 27 QSOs in our sample. In total, our sample covers a range from  $M_B$  -21 to -26, with median -23.3. In the remainder of this paper, we will compare some aspects of the PG QSOs to ultraluminous infrared galaxies whose properties will be presented in more detail in an upcoming paper based on QUEST data (Veilleux et al., in preparation).

### 10.2.2 Data Reduction and Line and Continuum Measurements

For the QUEST sample, spectra were taken both at 5-14 $\mu\text{m}$  in the low resolution (SL short-low) mode and at 10-37 $\mu\text{m}$  in the high resolution (SH short-high and LH long-high) modes of the *IRS*. Slit widths of 3.6'' to 11.1'' include much of the QSO hosts as well as the vicinity of the AGN. Our data reduction starts with the two-dimensional basic calibrated data (BCD) products provided by version 12 of the *Spitzer* pipeline reduction. We used our own IDL-based tools for removing outlying values for individual pixels and for sky subtraction and SMART (Higdon et al. 2004) for extraction of the final spectra. Small multiplicative corrections were applied to stitch together the individual orders of the low resolution and high resolution spectra, as well as additive corrections for residual offsets still found between the low resolution spectra and the SH and LH high resolution spectra after zodiacal light correction of the latter. Emission line fluxes were measured using fits of Gaussian lines superposed on a local continuum. PAH fluxes were mostly measured by simultaneously fitting Lorentzians to the main 6.2, 7.7, and 8.6 $\mu\text{m}$  features superposed on a 5.3 to 9.6 $\mu\text{m}$  (rest frame) continuum approximated by a second order polynomial, and in a few cases by combined Lorentzian and continuum fits over smaller ranges. We use below the flux for the brightest (7.7 $\mu\text{m}$ ) feature as PAH strength indicator  $F_{\text{PAH}}$ . In PG0050+124, where this feature was present but difficult to quantify in the presence of strong silicate emission, we have estimated the flux scaling from the flux of the well-detected 6.2 $\mu\text{m}$  PAH feature, using the 7.7/6.2 feature ratio measured in the starburst/AGN NGC 6240 (Lutz et al. 2003; Armus et al. 2006). Flux upper limits ( $3\sigma$ ) were derived adopting typical widths for the lines ( $\sim 600\text{km/s}$ ) and broad features ( $\sim 0.6\mu\text{m}$  for the 7.7 $\mu\text{m}$  feature). In one source (PG1307+085) we could only analyse the high resolution spectra since low resolution data are proprietary to another program. This limits our sample to 26 objects for analysis related to PAH emission. QUEST data for ultraluminous infrared galaxies that are used for comparison with the QSOs were processed in the same way.

Figure 10.1 shows individual example spectra of two PG QSOs illustrating the broad differences between QSOs with strong and weak PAH emission. Table 10.1 also lists the continuum flux densities in several mid- and far-infrared bands. In the mid-infrared, the quality of the *IRS* spectra is superior to most pre-existing *IRAS* or *ISO* photometry. For that reason and to characterise the continuum at wavelengths reasonably free of emission features, we have derived average observed flux densities over narrow bands ( $\Delta\lambda/\lambda \sim 0.07$ ) centered at several rest wavelengths. The shortest wavelength continuum point at 6 $\mu\text{m}$  is shortward of the main PAH complex; the 15 $\mu\text{m}$  point is between the two silicate

Object (1)	z (2)	S <sub>6</sub> mJy (3)	S <sub>15</sub> mJy (4)	S <sub>30</sub> mJy (5)	S <sub>60</sub> mJy (6)	S <sub>100</sub> mJy (7)	Ref (8)	D <sub>L</sub> Mpc (9)	log( $\nu L_\nu(60\mu\text{m})$ ) $L_\odot$ (10)
PG0026+129	0.1420	16.2	35.8	74	<162	<129	H00	672	<11.10
PG0050+124 (IZw1)	0.0611	178.3	515.1	1183	2243	2634	FSC	274	11.45
PG0157+001 (Mrk1014)	0.1630	32.1	217.3	1352	2224	2164	FSC	781	12.39
PG0838+770	0.1310	12.1	46.3	105	167	180	N86,H03	615	11.06
PG0953+414	0.2341	21.3	33.0	34	<129	<315	N86	1170	<11.71
PG1001+054	0.1605	16.8	34.5	69	140	146	H03	768	11.18
PG1004+130	0.2400	17.2	74.8	164	191	<284	S89	1203	11.74
PG1116+215	0.1765	54.5	78.4	113	<219	<285	H03	853	>11.50
PG1126-041 (Mrk1298)	0.0600	37.2	101.9	311	669	1172	N86	269	10.93
PG1229+204 (Mrk771)	0.0630	28.2	88.3	183	241	317	H03	283	10.52
PG1244+026	0.0482	15.8	66.7	194	368	362	H03	214	10.44
PG1302-102	0.2784	21.3	80.4	201	343	343	S89,H00	1425	12.14
PG1307+085	0.1550		50.2	101	212	155	S89,H03	739	11.29
PG1309+355	0.1840	22.1	70.9	106	<162	<192	H03	893	>11.40
PG1411+442	0.0896	61.4	96.9	139	147	140	H00	410	10.62
PG1426+015	0.0865	55.1	135.3	251	350	312	H03	395	10.96
PG1435-067	0.1260	18.3	33.3	77	304	<333	H03	590	11.28
PG1440+356 (Mrk478)	0.0791	55.1	135.3	251	597	780	H03	359	11.13
PG1448+273	0.0650	19.0	70.1	117	117	<252	S89	292	10.22
PG1613+658 (Mrk876)	0.1290	55.7	120.2	298	591	1002	H00	605	11.64
PG1617+175	0.1124	24.4	41.0	56	<98	<252	S89	522	>10.77
PG1626+554	0.1330	11.7	14.0	3	<156	70	H03	626	10.66
PG1700+518	0.2920	51.4	127.8		348	374	H03	1505	12.22
PG2214+139 (Mrk304)	0.0658	56.0	76.8	80	337	<282	N86	296	10.68
B2 2201+31A	0.2950	32.2	58.4		<295	<870	SP	1553	<12.43
PG2251+113	0.3255	15.4	35.6		<67	<214	N86	1706	<11.92
PG2349-014	0.1740	21.2	59.8	167	271	290	S89	840	11.55

Table 10.1: Col. (1) — Source name.; Col. (2) — Redshift.; Cols. (3-5) — Observed narrow band continuum flux densities around 6, 15, and 30  $\mu\text{m}$  rest wavelength, extracted from the *IRS* spectra. Missing entries are outside the rest wavelength range available for a given object.; Cols. (6-8) — *ISO* or *IRAS* fluxes at observed 60 and 100  $\mu\text{m}$ , and related references: FSC – IRAS Faint Source Catalog, H00 – Haas et al. (2000), H03 – Haas et al. (2003), N86 – Neugebauer et al. (1986), S89 – Sanders et al. (1989), SP – from IRAS Addscan/Scampi; Col. (9) — Luminosity distance in Mpc for a  $H_0=70\text{km s}^{-1}\text{Mpc}^{-1}$ ,  $\Omega_m=0.3$  and  $\Omega_\Lambda=0.7$  cosmology; Col. (10) — Far infrared luminosity. See text for treatment of limits.

emission peaks at about 10 and  $18\mu\text{m}$  (Siebenmorgen et al. 2005; Hao et al. 2005; Sturm et al. 2005), but still partly affected by silicate emission if present. The longest wavelength point at  $30\mu\text{m}$  is near the long end of the *IRS* spectra and already beyond the strongest part of the longer wavelength silicate feature. We later use continuum luminosities at these rest wavelengths:  $6\mu\text{m}$ ,  $15\mu\text{m}$ , and  $30\mu\text{m}$ , defined as  $\nu L_\nu$ .

Far-infrared fluxes have been taken from the literature, usually giving preference to *ISO* based results over *IRAS* based ones, because the smaller effective *ISO* beams reduced the susceptibility to cirrus contamination at  $100\mu\text{m}$ . The far IR luminosity,  $L(\text{FIR})$ , is often obtained from  $F_{\text{FIR}}$  which is defined as  $F_{\text{FIR}} = 1.26(S_{100} + 2.58 \times S_{60}) \times 10^{-18} \text{W}/\text{cm}^2$ , where  $S_{100}$  and  $S_{60}$  are flux densities in Jy (e.g., Sanders & Mirabel 1996). In order to use a consistent definition over the full  $z \leq 0.33$  redshift range of our sample and to reduce the sensitivity to galactic cirrus contamination that is most problematic at  $100\mu\text{m}$ , we adopt a far-infrared luminosity  $\nu L_\nu$  which is solely based on the flux at rest wavelength  $60\mu\text{m}$  interpolated from the photometry in the literature. Even nearby QSOs are typically close to the far-infrared detection limits of the previous space missions. In six cases where only one of  $S_{100}$  or  $S_{60}$  was detected we estimated the other flux as the lower of the measured limit and an extrapolation using the detected flux and the ratio  $S_{60}/S_{100} = 0.93$  that is the median for the part of the sample detected in both bands. The flux at  $60\mu\text{m}$  rest wavelength was interpolated linearly between the observed 60 and  $100\mu\text{m}$  points. For seven PG QSOs in our sample that are undetected in both bands, upper limits on  $\nu L_\nu$  at  $60\mu\text{m}$  rest wavelength were derived in an analogous way interpolating linearly between the limits at observed wavelengths of 60 and  $100\mu\text{m}$ . Since QSO fluxes are close to the detection limits of the original *IRAS* and *ISO* references and because of residual cirrus contamination, uncertainties of order 30-50% for the far-infrared fluxes may well occur.

## 10.3 Results

Table 10.2 lists the intensities of the three emission lines used in the present analysis, [Ne II]  $12.8\mu\text{m}$ , [Ne V]  $14.3\mu\text{m}$ , [O IV]  $25.9\mu\text{m}$  and of the emission feature PAH  $7.7\mu\text{m}$ . The table includes detections as well as upper limits. A more comprehensive list including more lines will be given in a forthcoming paper.

### 10.3.1 PAH Emission is Common in QSOs

As is clear from inspection of Table 10.2, some of the QSOs in our sample show only high excitation lines, likely originating in the NLRs of these objects. Others (11 of 26) show prominent PAH  $7.7\mu\text{m}$  and other PAH features, indicative of significant star formation. The existence of “composite” sources (see S02 for definition and references to ISO-based studies) that show both AGN and starburst properties, has been known for several years. Such sources contain both powerful star forming regions, giving rise to the observed PAH emission through near-UV heating, and high luminosity NLRs that are excited by the central radiation

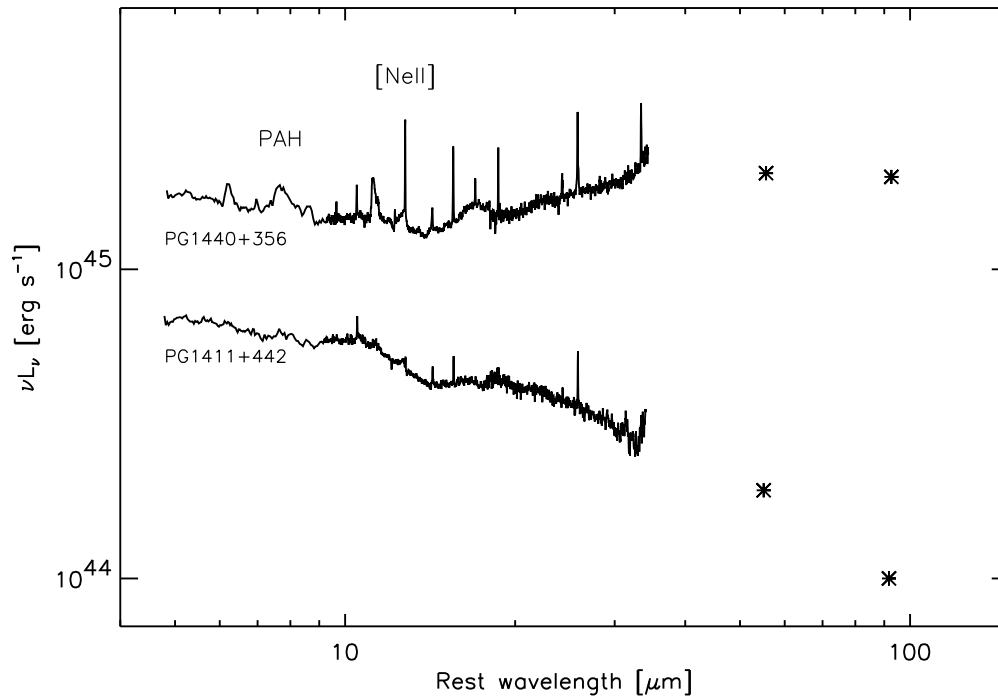


Figure 10.1: IRS spectra of two PG QSOs, combined with far-infrared photometric fluxes. These two nearby sources were selected to illustrate the full range between sources with strong PAH, [NeII], and far-infrared emission and others with weak emission in all these tracers. The spectrum of PG1440+356 has been multiplied by a factor 4 for clarity.

source. Since the star forming activity is a property of the host galaxy, and the NLR line luminosities scale with the AGN continuum luminosity, the intensity of the starburst emission features relative to the continuum might be expected to be weaker in AGN whose luminosities are in the QSO regime. Because the S02 sample included only three objects with QSO-like luminosities (i.e.  $L(\text{FIR}) > 5 \times 10^{11} L_{\odot}$ ) and suffered from the limited S/N achievable with *ISO*, a quantitative verification of this idea was not possible up to now.

Our new sample includes 27 high luminosity AGN and it is therefore important that the fraction of clear PAH emitters in the sample is large. This is strengthened further by the detection of PAH  $7.7\mu\text{m}$  and  $11.3\mu\text{m}$  peaks in the average spectrum of the 15 QSOs not showing *individual* PAH detections (Fig. 10.2, bottom). Since this average spectrum excludes sources with individual PAH detections, the PAH emission seen is unlikely to be due to a few PAH-strong sources only, in an otherwise largely PAH-free group. It also has the implication that typically the true PAH fluxes of the PAH nondetections cannot be far below our limits. This high incidence of PAH emission is our first major conclusion and is further discussed in the following sections.

Object	[Ne II] 12.8 $\mu$ m W cm $^{-2}$	[Ne V] 14.3 $\mu$ m W cm $^{-2}$	[O IV] 25.9 $\mu$ m W cm $^{-2}$	PAH 7.7 $\mu$ m W cm $^{-2}$
PG0026+129	2.29E-22	4.73E-22	2.14E-21	<8.70E-21
PG0050+124	1.94E-21	5.50E-21	2.75E-21	7.29E-20
PG0157+001	5.52E-21	5.18E-21	1.17E-20	5.93E-20
PG0838+770	4.11E-22	3.24E-22	1.30E-21	1.04E-20
PG0953+414	<1.70E-22	<1.90E-22	5.08E-22	<2.33E-20
PG1001+054	4.00E-22	<1.20E-22	5.19E-22	<1.32E-20
PG1004+130	<2.43E-22	<2.76E-22	2.10E-21	<1.47E-20
PG1116+215	<3.20E-22	<2.90E-22	1.10E-21	<3.50E-20
PG1126-041	1.39E-21	4.34E-21	1.59E-20	1.49E-20
PG1229+204	6.13E-22	9.06E-22	2.77E-21	<1.40E-20
PG1244+026	9.42E-22	5.31E-22	1.51E-21	6.02E-21
PG1302-102	3.56E-22	4.87E-22	2.60E-21	<8.52E-21
PG1307+085	3.98E-22	5.63E-22	7.38E-22	
PG1309+355	5.07E-22	2.69E-22	<4.95E-22	<3.80E-20
PG1411+442	3.61E-22	9.56E-22	1.49E-21	1.02E-20
PG1426+015	1.29E-21	1.25E-21	3.43E-21	2.36E-20
PG1435-067	<1.05E-22	5.22E-22	3.88E-22	<5.20E-21
PG1440+356	4.11E-21	1.33E-21	6.26E-21	7.38E-20
PG1448+273	5.07E-22	2.67E-21	1.01E-20	1.55E-20
PG1613+658	3.88E-21	1.13E-21	4.89E-21	3.86E-20
PG1617+175	2.89E-22	<1.70E-22	3.92E-22	<1.05E-20
PG1626+554	6.91E-23	<6.90E-23	<1.97E-22	<7.10E-21
PG1700+518	1.21E-21	<2.30E-22	1.68E-21	<2.40E-20
PG2214+139	2.26E-22	2.70E-22	1.27E-21	<1.30E-20
B2 2201+31A	9.64E-23	5.31E-22	5.62E-22	<7.89E-21
PG2251+113	1.69E-22	4.90E-22	3.08E-21	<8.00E-21
PG2349-014	1.44E-21	7.05E-22	3.87E-21	1.66E-20

Table 10.2: Measured emission features

### 10.3.2 Trends with Level of PAH Emission

Before embarking on an analysis of the correlations of different starburst and AGN tracers, we use the two average spectra of the PG QSOs that are individually detected in PAH emission (11 objects) or individually undetected in PAH emission (15 objects) (Fig. 10.2) to identify some of the salient trends in our data. The two spectra have been obtained by averaging the individual spectra after normalizing to the same total flux in the mid-infrared 5-25 $\mu$ m rest wavelength region. We caution that significant variations are present also within those two groups.

(i) PAH 7.7 $\mu$ m is 2.5 times stronger (relative to the total 5-25 $\mu$ m mid-infrared flux) in the average of the objects with individual PAH detections. This is a natural consequence of the object grouping for the two average spectra. As noted, the relatively small difference argues for the presence of PAH emission in most of the objects that did not have individual detections.

(ii) The far-infrared continuum emission is relatively stronger compared to the

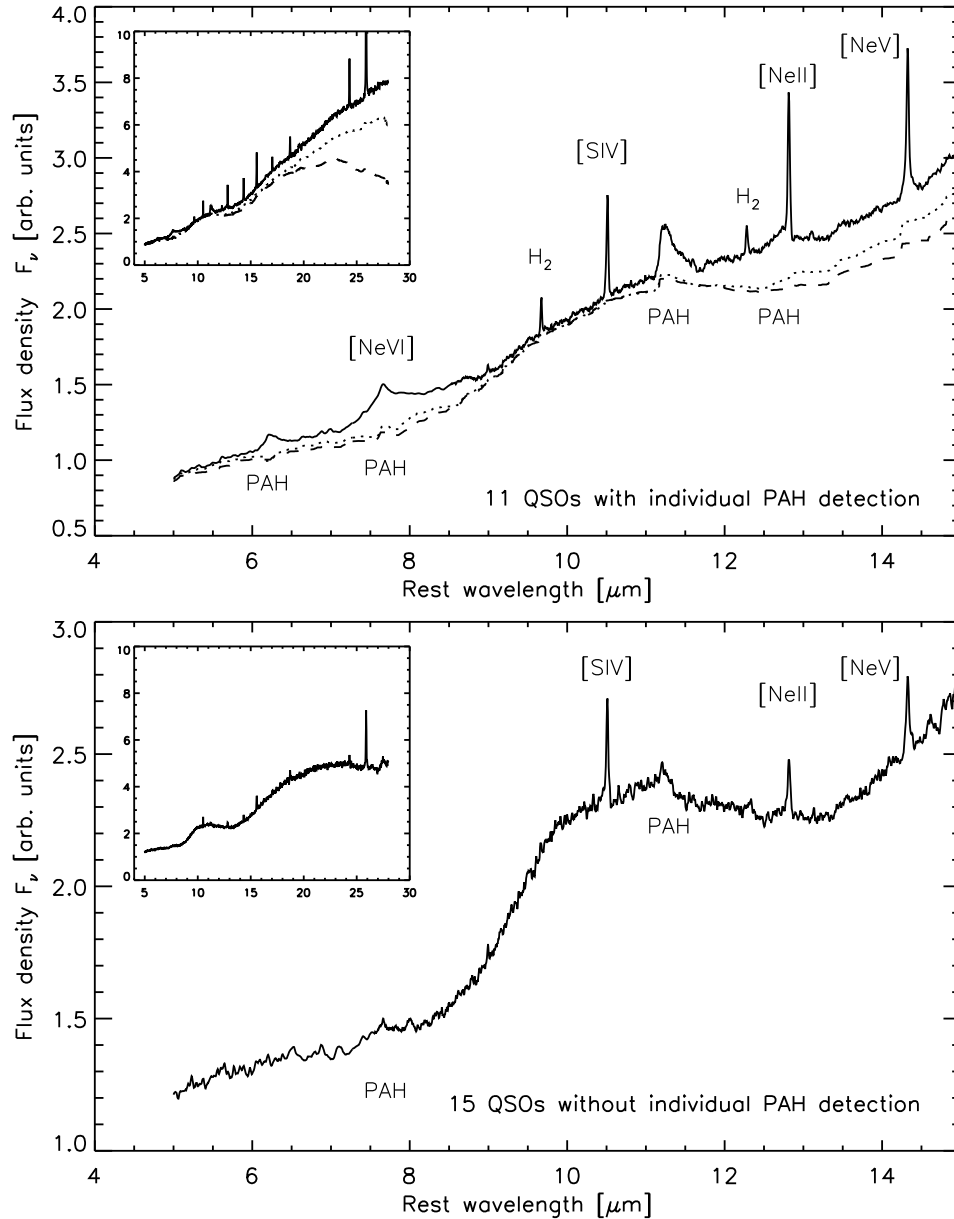


Figure 10.2: Average spectra of QSOs. Individual spectra have been normalized to the same total 5–25 $\mu\text{m}$  flux before averaging. Note the change in spectral resolution from low at short wavelengths to high at  $\geq 9\mu\text{m}$  rest wavelength. Top: 11 QSOs for which PAH7.7 $\mu\text{m}$  is detected in the individual spectra. The dotted line is the same spectrum after subtracting an M82 spectrum scaled to the PAH features, and the dashed line after subtracting a starburst-dominated ULIRG spectrum scaled to the PAH features. Emission line residuals have been removed for clarity. The inset repeats the same spectra with different plot scaling, emphasizing the wider range SED trends. Bottom: 15 QSOs for which PAH7.7 $\mu\text{m}$  is not detected individually. A broad maximum near 7.7 $\mu\text{m}$  rest wavelength as well as an 11.3 $\mu\text{m}$  feature is detected in the average, however, indicating a high incidence of PAH emission in the contributing spectra.

mid-infrared continuum in the objects with PAH detections. This is apparent in several ways. Firstly, all PAH detections are also far-infrared ( $60\mu\text{m}$  rest-frame) detections while 7 of 15 PAH nondetections are also not detected in the far infrared. Secondly, the mean ratio  $\nu F_\nu(60\mu\text{m})/\nu F_\nu(6\mu\text{m})$  is  $1.72\pm 0.54$  for the 11 PAH detections,  $1.00\pm 0.15$  for the 8 FIR-detected PAH nondetections,  $< 0.88$  for the 7 objects undetected in both far-infrared and PAH, and finally  $< 0.94$  for all 8+7 PAH nondetections. The values for the two upper limits assume that the far-infrared fluxes are less than or equal to the measured limits for the individual far-infrared nondetections. Thirdly, inspection of the average *IRS* spectra in Fig. 10.2 shows significant differences in the extrapolation to  $60\mu\text{m}$ : The average spectrum of the PAH detections continues to rise beyond  $25\mu\text{m}$ , while there is an indication for a downturn in the average of the PAH nondetections beyond this wavelength. Regardless of uncertainties in the extrapolation that are related to the assumed intrinsic spectral shape and to technical issues like *IRS* spectral response calibration and zodiacal light subtraction, the  $60\mu\text{m}$  to  $6\mu\text{m}$  flux density ratio must be significantly larger in the average spectrum of the sources with detected PAHs. We estimate that this ratio is larger for the PAH detections by a factor 2 to 3.

We have also tentatively grouped the PAH nondetections into two average spectra for the 8 far-infrared-detected and 7 far-infrared-nondetected sources. While the statistics and S/N are poorer in these samples, there are indications that the sources undetected in both tracers are at the end of the physical trends described in (i) and (ii) – little PAH, weak far-infrared, and indication for more of a downturn at  $\lambda > 25\mu\text{m}$ ; that is, they are not just fainter overall.

(iii) The lower excitation [NeII] line is stronger in the QSOs detected in PAHs. Normalized by the higher excitation lines [SIV] and [OIV], the [NeII] line is 1.9 and 1.7 times stronger in the QSOs detected in PAHs compared to those undetected in PAHs.

(iv) The broad  $10\mu\text{m}$  silicate emission peak is apparently weaker in the sources with detected PAHs. We argue this is largely an artefact of having a stronger starburst component with its PAH emission. This is illustrated by the dotted line in the upper panel of Fig. 10.2, which shows the average spectrum after subtracting a PAH-dominated M82 spectrum (Sturm et al. 2000) roughly scaled to the PAH features, and the dashed line, which shows the equivalent result using the average of 12 starburst-dominated QUEST ULIRGs (see §10.4.1) as a starburst template. As noted by, e.g., Sturm et al. (2000), a main difference between different starburst templates is in the level of increase of the  $\lambda \geq 12\mu\text{m}$  very small grain continuum, even for similar shorter wavelength PAH spectra. Our two choices illustrate the effect of such a template variation. The two PAH complexes around 7 and  $12\mu\text{m}$  and the far-infrared upturn serve to ‘fill in’ the minima between and around the two silicate emission peaks. This is analogous to the well-known difficulty of quantifying silicate *absorption* in spectra with strong PAH emission. We note that subtracting a starburst spectrum from the PAH-strong average QSO spectrum, in addition to recovering the correct pronounced silicate emission, also indicates a flatter or decreasing extrapolation to beyond  $25\mu\text{m}$ , similar to what is seen in the PAH-weak average QSO spectrum.

(v) Molecular hydrogen emission in the S(1), S(2) and S(3) rotational lines has a larger equivalent width in the PAH-strong average spectrum, by factors 3-5 comparing these detections with the detections/limits for the PAH-weak average spectrum.

All these trends are consistent with a starburst component (containing strong PAH and far-infrared continuum, low excitation fine-structure line, and possibly molecular hydrogen emission) being superimposed in increasing proportion on a pure AGN spectrum (consisting of warm and hot dust continuum, silicate, and high excitation line emission).

## 10.4 Discussion

### 10.4.1 Nature of the QSO Far-Infrared Emission and the Starburst-AGN Connection

We use our sample to compare several AGN- and starburst related quantities observed in the PG QSOs, in an attempt to identify the likely origin of the far-infrared emission. We compare the starburst tracers in these QSOs with those of pure starbursts from two samples: (i) A subset of starburst-dominated QUEST ULIRGs observed with *IRS* ('SB-ULIRGS'). In order to restrict ourselves to the ULIRGs with the highest starburst contribution to their infrared luminosity, we require these objects to have no [O IV]  $25.9\mu\text{m}$  detection, a peak ratio of the PAH  $7.7\mu\text{m}$  feature to its local continuum of at least 1, and a  $5\text{-}10\mu\text{m}$  spectrum in which visual inspection shows that the absorption features like the  $6\mu\text{m}$  ice feature are not dominant, although sometimes present. The last criterion is used to avoid ambiguities concerning the internal energy sources of the most heavily obscured ULIRGs (Spoon et al. 2004a,b). (ii) A small sample of six *ISO*-observed local starbursts (M82, NGC253, NGC1808, IC342, NGC3256, NGC7552) for which the PAH emission is measured without significant aperture corrections relative to the far-infrared data from *IRAS*, *ISO* or the Kuiper Airborne Observatory *KAO*. The ratio of PAH and far-infrared emission is known to vary somewhat with physical conditions (see e.g. discussion in §4.2 of Lutz et al. 2003), decreasing with the average intensity of the radiation field (e.g. Dale et al. 2001). Because of these trends with ISM conditions, we add as another group of comparison objects (iii) twelve 'FIR quiescent' galaxies (with particularly low  $L_{FIR}/L_B$  and low  $S_{60}/S_{100}$ ) from the sample of normal galaxies of Lu et al. (2003), for which we convert their PAH fluxes measured in ISOPHOT-S spectra to our measurement procedure and apply aperture corrections based on their PAH-dominated ISOCAM LW2 images. We add to this group NGC 891 that has been mapped with ISOPHOT-S by Mattila et al. (1999), arriving at a sample of 13 FIR-quiescent objects. The three comparison samples cover a range in luminosity as well as in the average intensity of their interstellar radiation fields that is reflected in their mid-to far-infrared SEDs.

An important new result is the clear correlation between  $L(\text{PAH } 7.7\mu\text{m})$  and  $L(\text{FIR})$  for the PAH-containing QSOs. Figs. 10.3 and 10.4 compare the luminosities and fluxes of PAH  $7.7\mu\text{m}$  and  $60\mu\text{m}$  continuum. The QSOs with PAH

detections and the starburst-dominated ULIRGs follow the same trend. Fig. 10.5 shows the equivalent continuous trend from QSOs to starburst-dominated ULIRGs for the comparison of [Ne II]  $12.8\mu\text{m}$  and  $60\mu\text{m}$  continuum.

These trends also imply almost identical mean ratios for the QSO and starburst-dominated ULIRG populations. For the 11 QSOs with both PAH and far-infrared emission detected we find  $\langle L(\text{PAH})/L(\text{FIR}) \rangle = 0.0110 \pm 0.0021$  while for the 12 starburst-dominated ULIRGs we get  $\langle L(\text{PAH})/L(\text{FIR}) \rangle = 0.0130 \pm 0.0015$ . Similarly, comparing [Ne II]  $12.8\mu\text{m}$  and far-infrared emission we get for the 18 QSOs with both quantities detected  $\langle L([\text{NeII}])/L(\text{FIR}) \rangle = (5.15 \pm 0.73) \times 10^{-4}$  and for the 12 starburst-dominated ULIRGs  $\langle L([\text{NeII}])/L(\text{FIR}) \rangle = (4.22 \pm 0.57) \times 10^{-4}$ . In both cases, the ratio of the star formation indicator and far-infrared emission is the same in QSOs and in starburst-dominated ULIRGs – the observations are consistent with starbursts producing all of the QSO far-infrared emission if their specific properties are similar to those in starburst dominated ULIRGs. This argument depends on the adopted specific properties of the comparison starforming galaxies, because of the changes of the PAH to  $60\mu\text{m}$  ratio with ISM properties mentioned above. For ULIRG starbursts we obtained  $\langle L(\text{PAH})/L(\text{FIR}) \rangle = 0.0130 \pm 0.0015$ . For the six lower luminosity starbursts for which the ratio of PAH and far-infrared can be derived from *ISO* data without significant aperture corrections, we obtain  $\langle L(\text{PAH})/L(\text{FIR}) \rangle = 0.0399 \pm 0.0087$ . Finally, for the sample of 13 FIR-quiet normal galaxies we get  $\langle L(\text{PAH})/L(\text{FIR}) \rangle = 0.126 \pm 0.016$  with individual objects like NGC 891 reaching up to a value 0.2.

Comparing these three ratios to the average of the QSOs, we find that almost all, at least  $\sim 30\%$ , and at least  $\sim 10\%$  of the QSO far-infrared emission would be due to non-AGN sources (that is current and recent star formation), adopting the values for ULIRGs, starbursts and FIR-quiet normal galaxies as templates. Irrespective of the adopted template, PAH-based values are lower limits since for QSOs there is the interesting possibility of additional weakening of PAH emission in star-forming regions that are also exposed to AGN radiation, by destruction of the PAH molecules. This may be particularly relevant if some of the far-infrared emission is generated by star formation occurring in compact clusters or disks very close to the AGN (Davies et al. 2004a,b). This makes values towards the upper end of the range for the non-AGN contribution more likely.

Using only PAH and far-infrared evidence, a formal solution is possible which maximizes the AGN fraction of the far-infrared emission by assigning the PAH emission to a very FIR-quiet normal galaxy. The QSO PAH luminosities are on average larger than those of the FIR quiet normal galaxies, but the most luminous quiet normal objects are of a similar PAH luminosity as the typical QSOs (Fig. 10.3). Comparing these objects to QSOs, the AGN would then contribute roughly 90% of the QSO far-infrared flux. These objects yield biased comparisons, however, since they are specifically selected for FIR quietness. A fairer comparison would need to populate the PAH/FIR plane of Fig. 10.3 with a large and complete sample of non-AGN galaxies. While such a sample is currently not available, we qualitatively indicate in Fig. 10.3 the expected locus of such non-AGN galaxies by connecting the locations of the averages of our three small comparison samples (dotted line).

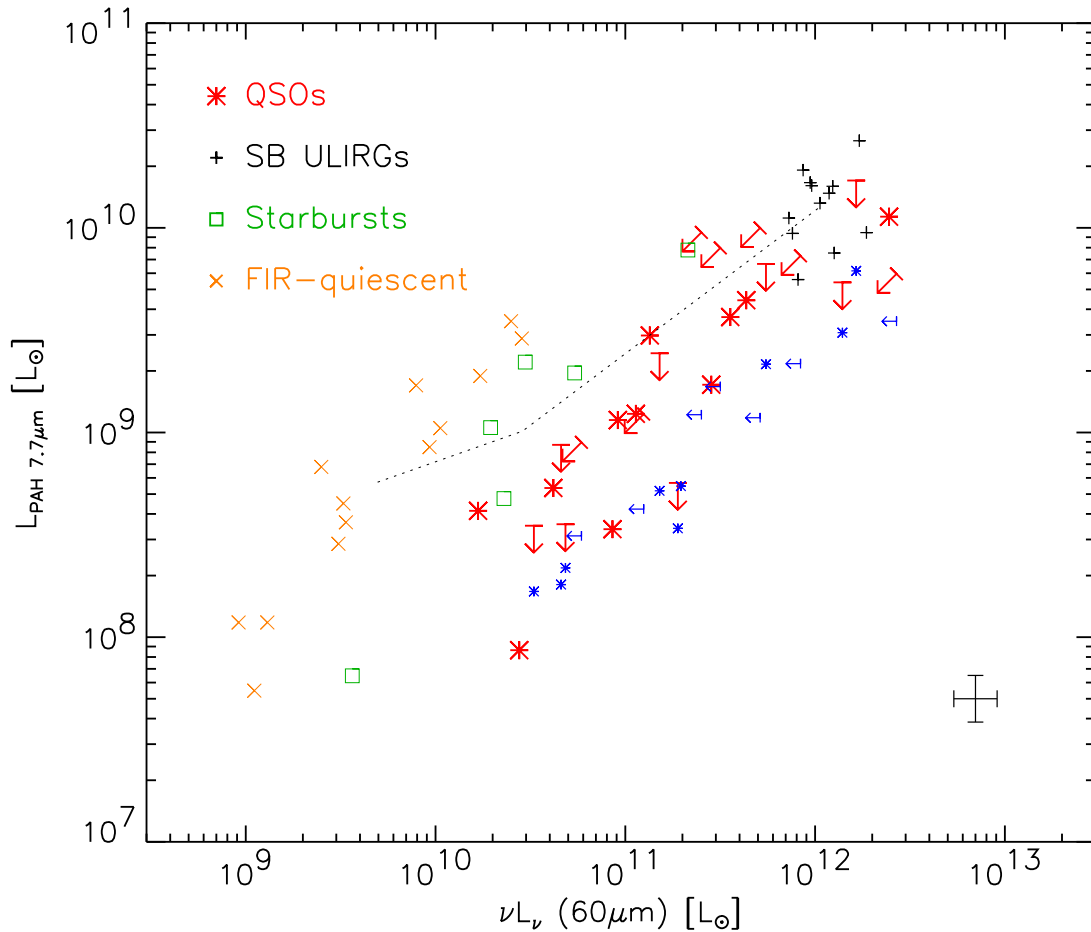


Figure 10.3: Luminosities  $L(\text{PAH } 7.7\mu\text{m})$  vs.  $L(60\mu\text{m})$  for the QSOs. Starburst dominated ULIRGs, lower luminosity starbursts, and FIR-quiet galaxies are added for comparison. The thin dotted line connects the mean locations of these three groups of comparison objects. The small blue symbols repeat the QSOs without individual PAH detections, but assuming that the individual ratios of PAH  $7.7\mu\text{m}$  to rest frame  $5\text{--}25\mu\text{m}$  flux are the same as in the average spectrum of Fig. 10.2 (bottom). A 30%  $1\sigma$  uncertainty is indicated in the lower right corner.

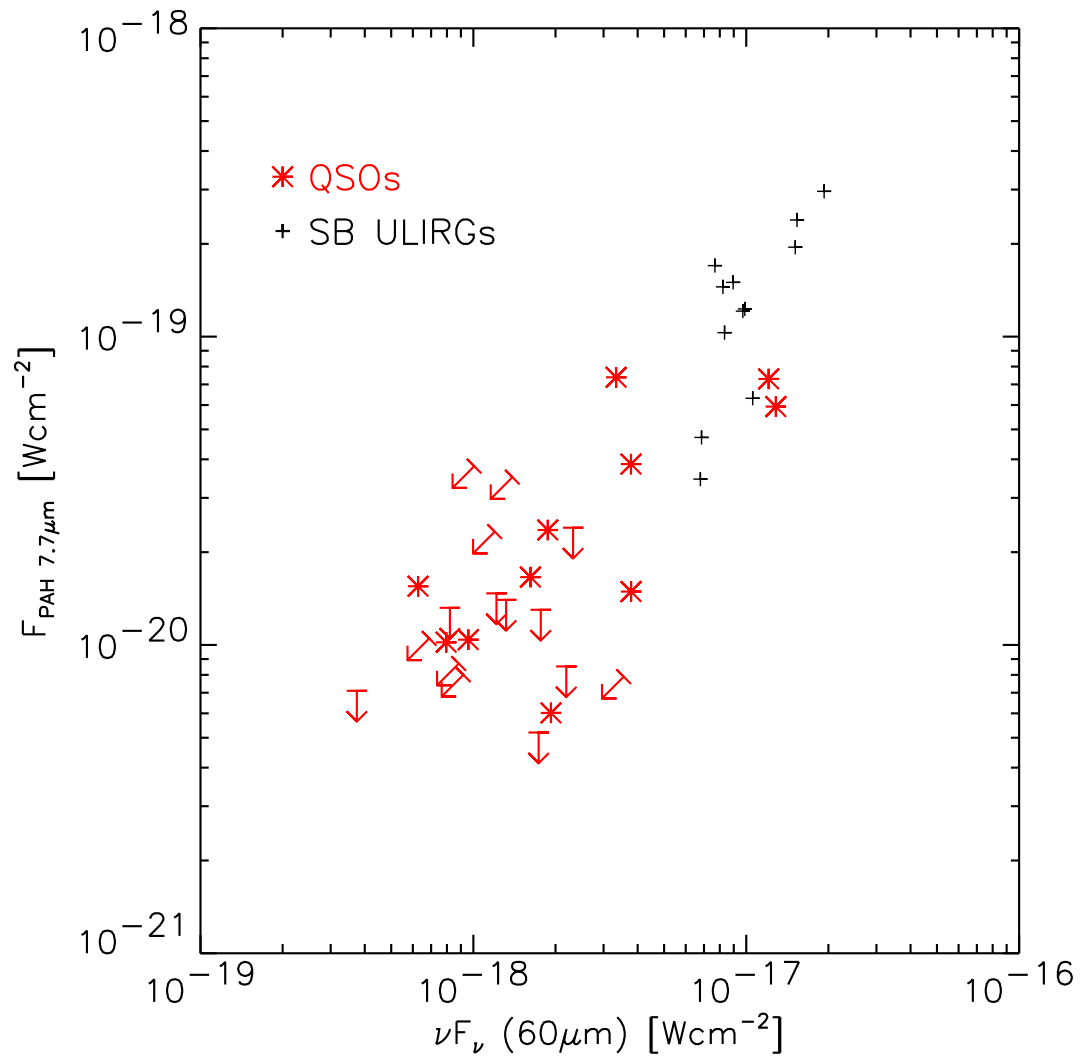


Figure 10.4: Fluxes  $F(\text{PAH } 7.7\mu\text{m})$  vs.  $F(60\mu\text{m})$  for the QSOs and for starburst dominated ULIRGs.

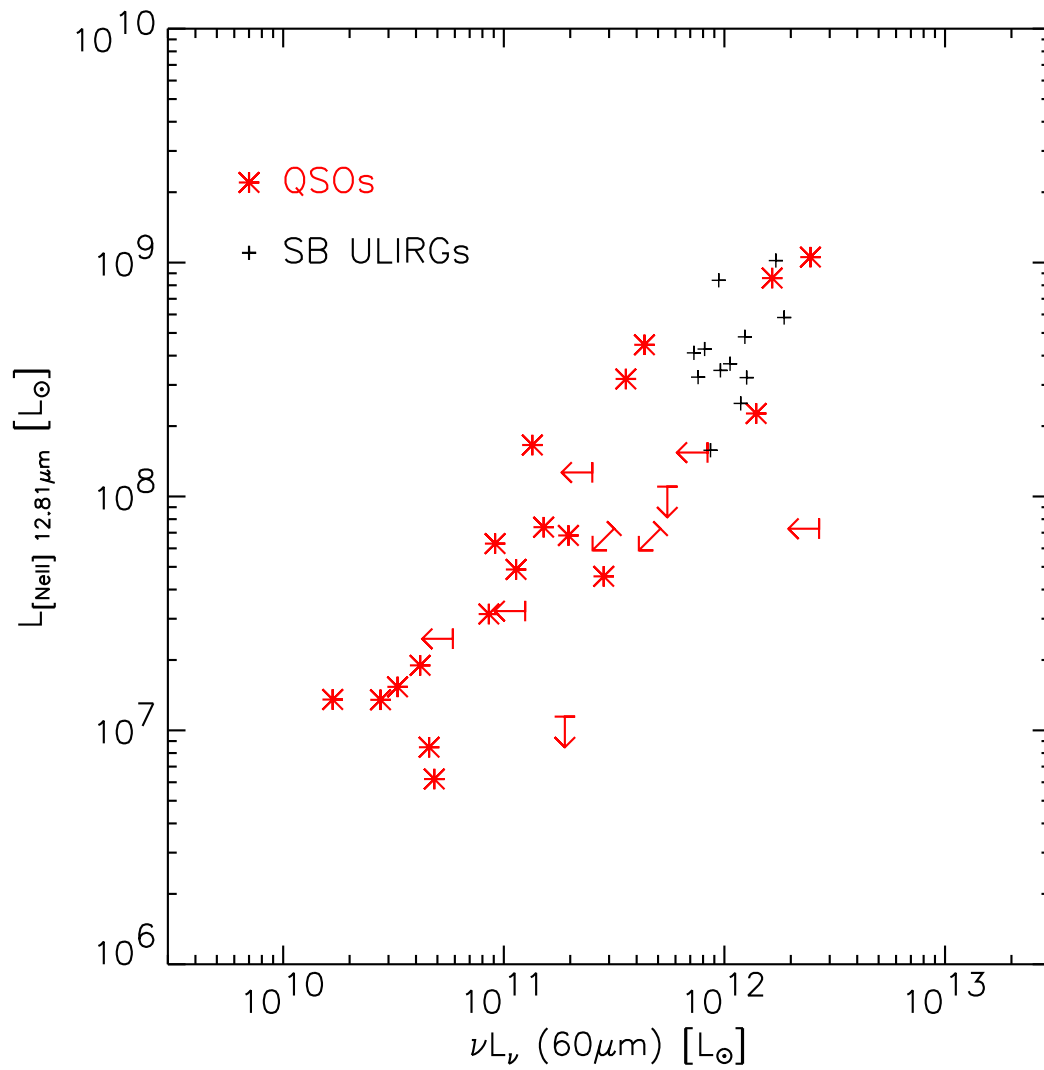


Figure 10.5: Luminosities  $L([\text{NeII}] 12.8\mu\text{m})$  vs.  $L(60\mu\text{m})$  for the QSOs and for starburst dominated ULIRGs.

While the FIR quiescent objects are likely more PAH luminous than the average galaxy of the same FIR luminosity, and thus their point placed too high, the overall trend of PAH flux with FIR flux is certainly robust, and the slope of this relation for non-AGN galaxies less than 1, in agreement with the photometric relation between total infrared and ISOCAM LW2 emission studied by Chary & Elbaz (2001). Applying such a luminosity-dependent ratio of PAH to FIR luminosity to QSOs is consistent with our finding of star formation dominating the FIR emission in many of our QSOs. The alternate scenario, in which host galaxies are all PAH luminous but FIR-quiescent and the far-infrared emission of QSOs is AGN dominated, is both complex and inconsistent with some of the evidence presented in §10.3.2. Specifically, it cannot explain why both the far-infrared *and* the PAH emission rise together relative to the mid-IR continuum (i.e. AGN) luminosity (see also Figure 10.2). Moreover, this scenario does not agree with the multiwavelength evidence for active star formation mentioned in §10.4.3.

Considering these trends and the fact that the far-infrared luminosities of the PG QSOs are typically in the  $\geq 10^{11} L_{\odot}$  regime, we conclude that for the average QSO in the sample the star formation contribution to the FIR emission is at least 30% (applying the starburst PAH to  $60\mu\text{m}$  conversion), and that star formation may well be dominant. Comparing the locus of QSOs in Fig. 10.3 with the trend for star-forming comparison objects suggests a tendency for the star formation contribution to be largest in the most FIR-luminous QSOs.

Similar considerations can be made for the comparison of [Ne II]  $12.8\mu\text{m}$  and far-infrared emission in QSOs and ULIRGs (Fig.10.5). Here, the sources of uncertainty are the NLR contribution to [Ne II]  $12.8\mu\text{m}$  for the QSOs and the possibility of different extinction in the QSO starbursts and the ULIRGs which show considerable mid-IR extinction (Genzel et al. 1998).

The similarity between QSOs and starburst-dominated ULIRGs in trends and ratios based on PAH  $7.7\mu\text{m}$ , [Ne II]  $12.8\mu\text{m}$ , and far-infrared continuum no longer holds when we plot a clearly AGN-related quantity on one axis. Fig. 10.6 shows that the ratio of PAH and  $6\mu\text{m}$  continuum differs between QSOs and starburst-dominated ULIRGs by more than an order of magnitude, and that the two classes separate clearly in the diagram. An additional strong non-starburst component is required in the QSOs which clearly is the AGN-heated warm dust continuum. We note, however, a clear correlation between the luminosities of AGN  $6\mu\text{m}$  continuum and starburst PAH among the QSOs. We will now argue on the basis of a more comprehensive comparison that this correlation is indirect, caused by a starburst-AGN connection in QSOs.

In a flux-limited sample selected based on an emission component that is directly due to the AGN, as is the case for the PG sample (selected by pointlike appearance, B magnitude and blue U-B color), we expect correlations between the luminosities of the various AGN tracers to arise directly as a consequence of the sample selection. Correlations are not expected when comparing AGN- and starburst-related quantities unless there is a real physical correlation.

A summary of correlation coefficients among the continua, PAH and line fluxes measured in the QSOs is given in Table 10.3. Some of the relations are also shown

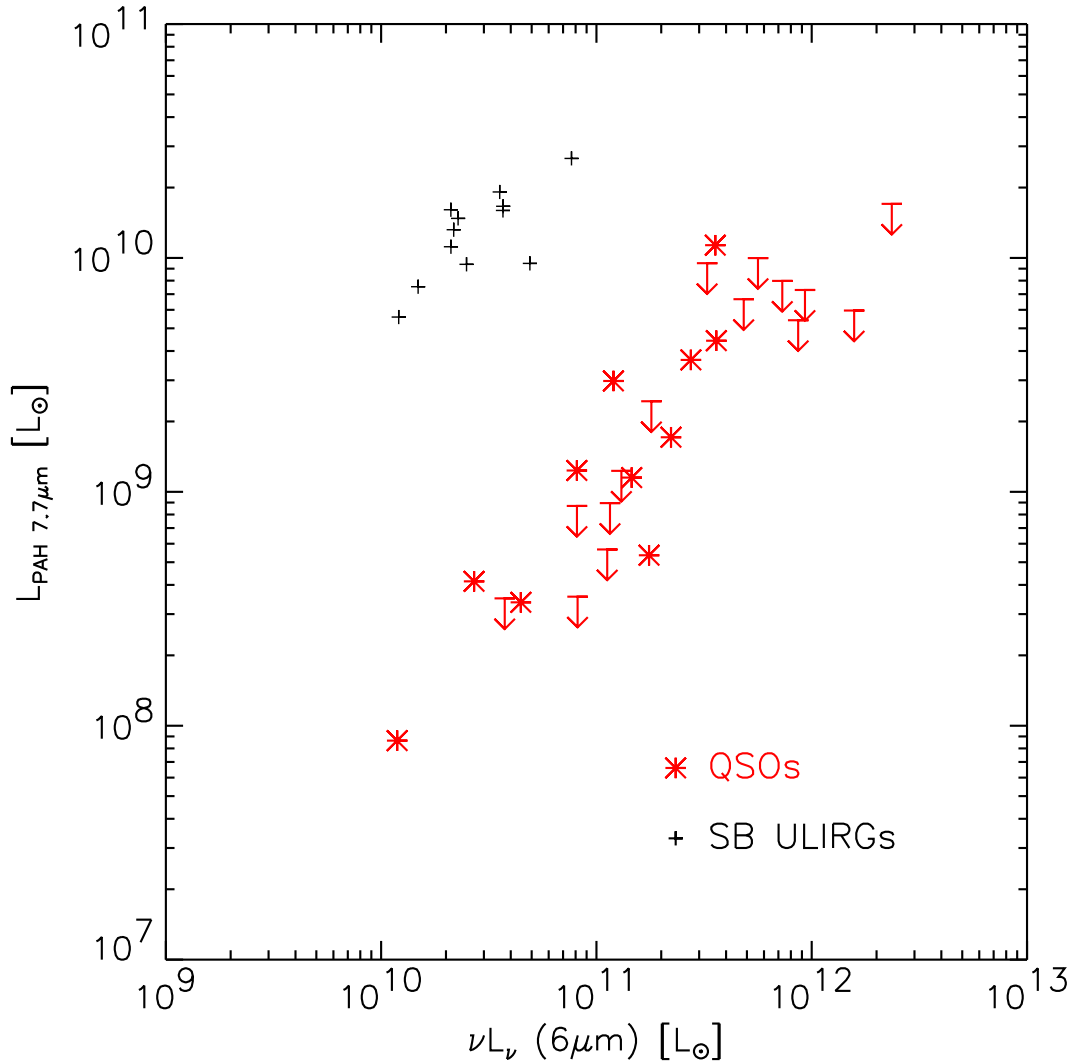


Figure 10.6: Luminosities  $L(\text{PAH } 7.7\mu\text{m})$  vs.  $L(6\mu\text{m})$  for the QSOs and for starburst dominated ULIRGs.

in Figs. 10.3 to 10.7. In Table 10.3 we list Spearman rank correlation coefficients for the detected objects and their significance both for luminosities and for the observed fluxes. Given the selection of the PG sample over a relatively narrow flux range, the correlations in flux are generally less tight, but agree with the findings based on luminosities. Our dataset includes upper limits, in particular for feature measurements and far-infrared fluxes, as well as trends between luminosity and distance caused by the flux limited selection. For these reasons, we also list in Table 10.3 partial correlation coefficients (explicitly excluding the effect of distance) that have been computed using the formalism of Akritas & Siebert (1996) which provides partial correlation analysis for censored data. The results from this analysis of the full censored dataset are in agreement with those from the detections only.

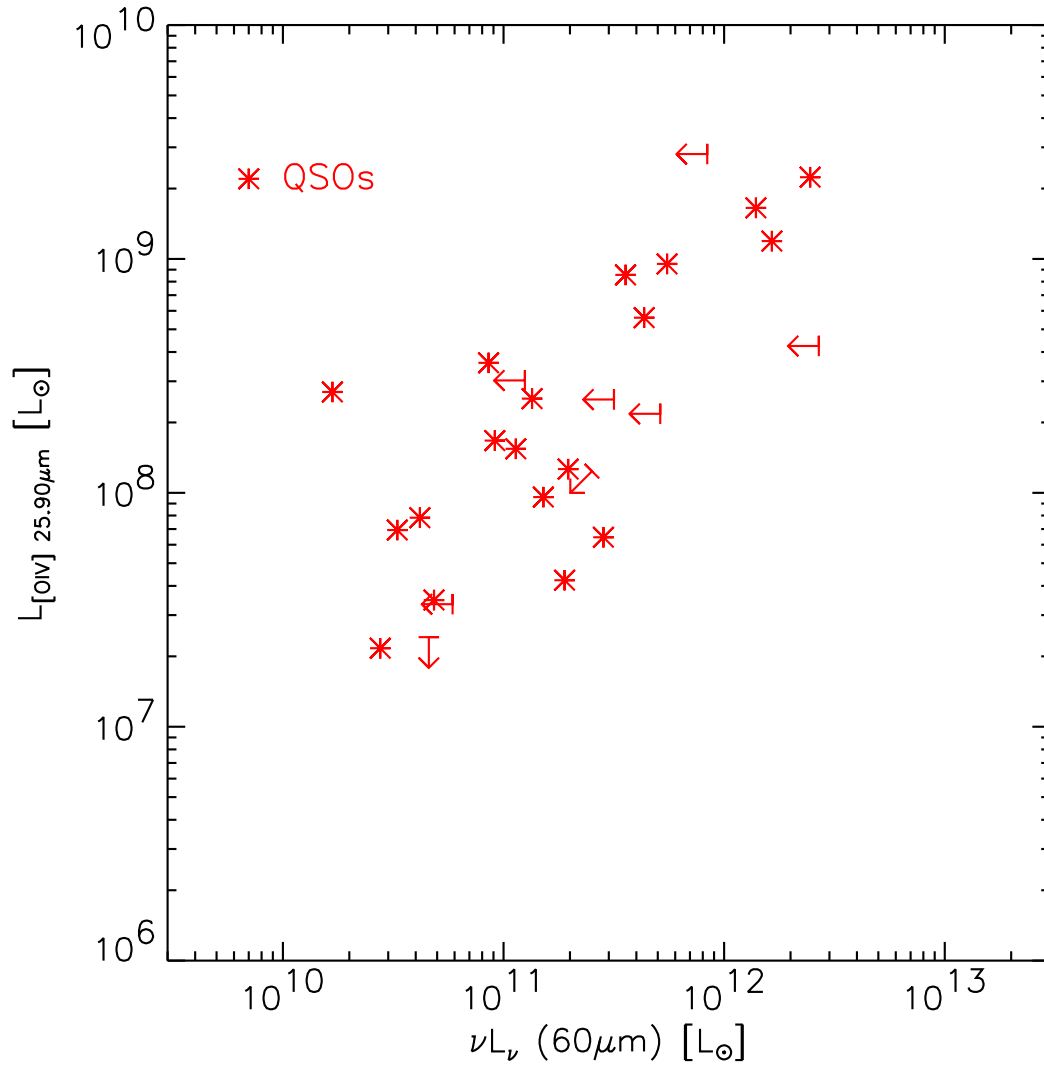


Figure 10.7: Luminosities  $L([\text{O IV}] 25.9\mu\text{m})$  vs.  $L(60\mu\text{m})$  for the QSOs

Property A	Property B	Number Detect.	$R_S$ Lumin.	Probability Lumin.	$R_S$ Flux	Probability Flux	Dispersion	Number All	PKT	Probability
(1)	(2)	(3)	(4)	(5)	(6)	(7)	(8)	(9)	(10)	(11)
60 $\mu$ m	PAH	11	0.945	1.1E-5	0.582	6.0E-2	0.293	26	0.248	5.7E-3
60 $\mu$ m	6 $\mu$ m	19	0.894	2.4E-7	0.567	1.1E-2	0.303	26	0.321	1.6E-2
60 $\mu$ m	15 $\mu$ m	20	0.938	9.8E-10	0.746	1.6E-4	0.212	27	0.441	2.8E-4
60 $\mu$ m	30 $\mu$ m	19	0.926	1.3E-8	0.825	1.4E-5	0.384	24	0.530	4.6E-5
60 $\mu$ m	[NeII]	18	0.899	4.0E-7	0.744	4.0E-4	0.284	27	0.329	1.1E-3
60 $\mu$ m	[OIV]	19	0.670	1.7E-3	0.493	3.2E-2	0.422	27	0.267	1.4E-2
60 $\mu$ m	[NeV]	16	0.788	2.9E-4	0.456	7.6E-2	0.345	27	0.257	3.1E-2
PAH	6 $\mu$ m	11	0.873	4.6E-4	0.473	1.4E-1	0.283	26	0.174	6.2E-2
PAH	15 $\mu$ m	11	0.927	1.0E-5	0.800	3.1E-3	0.219	26	0.277	5.3E-3
PAH	30 $\mu$ m	11	0.927	4.0E-5	0.636	3.5E-2	0.268	23	0.346	1.6E-3
PAH	[NeII]	11	0.936	2.2E-5	0.845	1.1E-3	0.246	26	0.287	1.1E-3
PAH	[OIV]	11	0.600	5.1E-2	0.436	1.8E-1	0.397	26	0.186	2.6E-2
PAH	[NeV]	11	0.682	2.1E-2	0.636	3.5E-2	0.352	26	0.214	1.2E-2
6 $\mu$ m	[OIV]	24	0.657	4.8E-4	0.147	4.9E-1	0.482	26	0.264	8.4E-3
6 $\mu$ m	[NeV]	19	0.770	1.2E-4	0.484	3.6E-2	0.366	26	0.256	4.0E-2

Table 10.3: Correlation of measured properties: (column explanation see next page)

Column explanation of Table 10.3:

- Col. (1) — First variable. Wavelengths stand for continuum at that rest wavelength.  
 Col. (2) — Second variable.  
 Col. (3) — Number of sources detected in both quantities.  
 Col. (4) — Spearman’s rank correlation coefficient for luminosities, for detected sources.  
 Col. (5) — Probability of exceeding the measured correlation coefficient for luminosities in the null hypothesis of uncorrelated data. Smaller values indicate more significant correlations.  
 Col. (6) — Spearman’s rank correlation coefficient for fluxes.  
 Col. (7) — Probability of exceeding correlation coefficient for fluxes in the null hypothesis.  
 Col. (8) — Dispersion of  $\text{Log}_{10}(A/B)$  for the detected sources.  
 Col. (9) — Total number of sources measured (detections and limits).  
 Col. (10) — Partial Kendall  $\tau$  coefficient describing correlation between luminosities A and B, excluding the effect of distance. Value computed using the formalism of Akritas & Siebert (1996) that extends the Kendall  $\tau$ -coefficient to partial correlation in the presence of censored data (i.e. data including upper limits).  
 Col. (11) — Probability of exceeding partial correlation coefficient in the null hypothesis.

A first and expected finding is the significant correlations between various luminosities tracing the AGN components, e.g.  $6\mu\text{m}$  continuum and the high excitation emission lines. There is a noticeable spread in the ratio of mid-infrared continuum emission and emission in the mid-infrared high excitation lines [O IV]  $25.9\mu\text{m}$  and [Ne V]  $14.3\mu\text{m}$ , however, equivalent to a spread in equivalent width of these lines. This is not uncommon in other AGN narrow emission lines like [O III]  $\lambda 5007$  (e.g. Boroson & Green 1992; Baskin & Laor 2005) and has implications for the reliability of NLR lines as direct tracers of AGN bolometric luminosity. Netzer et al. (2006) discuss this large spread of [O III]  $\lambda 5007$  equivalent width which is likely a general property of AGN and also a function of source luminosity (the ‘Baldwin-effect’) and emission line reddening.

Clear correlations are also seen between quantities tracing starburst activity (PAH  $7.7\mu\text{m}$  being the cleanest) and others that in the QSOs must be almost fully dominated by the AGN (like  $6\mu\text{m}$  continuum or high excitation lines). Such correlations are not caused by the PG sample selection by B-band flux and U-B color, and must indicate a true relation of more luminous QSOs on average being associated with more luminous star formation. In the presence of such a “starburst-AGN connection”, evidence on the causal links connecting the correlated observables has to be obtained from the quality of the correlations, and in particular from comparing the absolute values of the correlated quantities with templates as done above for far-infrared and PAH.

While the size of the present sample is modest, Table 10.3 shows that the correlation between PAH  $7.7\mu\text{m}$  and far-infrared luminosities is one of the tighter among the combinations we investigated. Consistent with this trend is the stronger correlation of [Ne II]  $12.8\mu\text{m}$  with far-infrared than is the case for far-infrared with either [O IV]  $25.9\mu\text{m}$  or [Ne V]  $14.3\mu\text{m}$ . [Ne II]  $12.8\mu\text{m}$  is a line that is emitted both in the NLR of AGN (Sturm et al. 2002), with higher excita-

tion lines usually being stronger, and as the strongest mid-infrared line in the spectra of most starbursts (Thornley et al. 2000; Verma et al. 2003). The good correlation of [Ne II] 12.8 $\mu$ m and far-infrared thus indicates a strong starburst contribution to both [Ne II] 12.8 $\mu$ m and far-infrared emission, reinforcing the conclusion reached from the starburst-like ratios of these quantities. In a larger sample, these considerations could be expanded to a more rigorous test on the basis of the quality of the correlations. Even in the presence of a starburst-AGN connection, starburst tracers should usually correlate more tightly with other starburst tracers than with AGN tracers. Our sample is not big enough for robust conclusions of this type. Looking at the probability of exceeding the partial correlation coefficients for the full censored dataset in the null hypothesis of uncorrelated data (column 11 of Table 10.3), it is nevertheless reassuring but certainly tentative that the seven least significant of the 14 correlations discussed are 60 $\mu$ m vs. 6 $\mu$ m, 60 $\mu$ m vs. [O IV] 25.9 $\mu$ m, 60 $\mu$ m vs. [Ne V] 14.3 $\mu$ m, PAH vs. 6 $\mu$ m, PAH vs. [O IV] 25.9 $\mu$ m, PAH vs. [Ne V] 14.3 $\mu$ m, 6 $\mu$ m vs. [Ne V] 14.3 $\mu$ m. With the exception of the last, these less significant correlations are all of the type starburst tracer vs. AGN tracer, in the superposition scenario outlined in §10.3.2, and provided that the far-infrared is counted as a star formation tracer.

We conclude that, while there are also ‘indirect’ correlations caused by a global correlation of AGN and starburst luminosity in our PG sample, the relation between PAH, [Ne II], and far-infrared is real and reflects the starburst component. The most important support for this interpretation is the starburst-like ratios of these three quantities. Starbursts contribute at least  $\sim 30\%$  and likely most of the far-infrared emission in the average QSO in our sample. An upper limit to the starburst contribution is imposed by the need for a realistic continuation to longer wavelengths of the AGN mid-IR continuum, which cannot fall off more steeply than the Rayleigh-Jeans like emission of optically thin dust of an appropriate temperature. The true slope is likely somewhat shallower due to variation in temperature and due to non-negligible optical depth in part of the mid-IR emitting region. We feel that the origin and interplay of silicate emission and continuum in the SED of the AGN is not yet well enough measured or modelled for an accurate AGN continuum extrapolation of this type. This is also due to the need for unambiguous decomposition of starburst, silicate, and AGN continuum. Nevertheless, we consider the minimum pure AGN far-infrared continuum required by the data to be consistent with our global conclusion from the PAH 7.7 $\mu$ m and [Ne II] 12.8 $\mu$ m emission.

### 10.4.2 Mid-infrared Diagnostics and the Starburst-AGN Connection in QSOs

Extending earlier ground-based work (e.g., Roche et al. 1991, Genzel et al. (1998) and Laurent et al. (2000) presented the first empirical versions of the tools now used to separate AGN-powered from starburst-powered infrared galaxies. The basis of these tools is that the intensity of the PAH features in starburst-powered systems traces the starburst’s (far-infrared) luminosity, while these features are easily destroyed by the strong and hard AGN radiation. Our present study widens

the scope of the Genzel et al. (1998) work by focusing on star formation signatures in high luminosity bona-fide AGNs. We have used our QUEST QSO sample to look for three starburst signatures, strong PAH features, strong [NeII] lines and strong far-infrared continuum. Although two of those ([NeII] and far-infrared) can also partly originate in AGN environments, we have argued in §10.4.1 that the three quantities scale with each other and are tracing significant star formation in most objects of our PG QSOs sample. The measured far-infrared luminosity  $\nu L_\nu(60\mu\text{m})$  ranges between  $1.7 \times 10^{10}$  and  $2.5 \times 10^{12} L_\odot$ , covering a wide range of starburst luminosity up to the ULIRG regime, and limits for the remaining QSOs are consistent with starburst emission in the same range of luminosities.

An important result is the correlation of PAH (starburst) luminosity and AGN luminosity in our sample. This extends to higher luminosity a similar result obtained by S02 on the basis of *ISO* spectroscopy of mostly lower luminosity Seyferts, and of a wide range of optical and near-infrared studies suggesting elevated starburst activity in Seyferts (e.g. Heckman et al. 1997; Oilva et al. 1999; Gonzalez-Delgado et al. 2001; Imanishi 2003; Kauffmann et al 2003). Such a connection between small scale AGN feeding and larger scale starburst activity is plausible (e.g., Norman & Scoville 1988) and may play a role in establishing the black hole mass to bulge velocity dispersion relation in galaxies. Its details are far from trivial, however, and warrant observations with higher spatial resolution to elucidate the spatial structure of star formation in these QSOs (see for example Cresci et al. 2004).

Another effect of this connection relates to the interpretation of correlations between QSO properties measured at different wavelengths. Some observed correlations may be indirect, driven by the starburst-AGN connection, as argued for example by Rowan-Robinson (1995) for optical and far-infrared continua. Haas et al. (2003), however, have used among other arguments the observed correlation between rest frame mid-infrared and far-infrared continuum in their QSO sample to argue for an AGN origin of the latter. The sensitivity of the *ISO* spectroscopic data they had available did not allow for a conclusive test on the basis of PAH emission. While we confirm the mid- to far-infrared correlation for QSOs for our PG sample (e.g., Fig. 10.8), we use our higher sensitivity *Spitzer* PAH  $7.7\mu\text{m}$  and [Ne II]  $12.8\mu\text{m}$  data to argue for an indirect nature of this correlation for the luminosity range covered by our sample, induced by a starburst-AGN connection. A similar test remains to be done for the highest luminosity members of the Haas et al. (2003) sample, which are not sufficiently represented in our local PG sample or in the IRS spectra of radio galaxies and radio-loud QSOs of Haas et al. (2005). Such high quality mid-infrared spectra of highest luminosity QSOs should also be able to test whether a trend for decreasing FIR to MIR ratio at highest optical luminosity (as suggested by Fig. 4 of Haas et al. 2003) reflects an increase in relative AGN intensity compared to the host and its star formation. A central question in the study of QSOs and ULIRGs is their possible evolutionary relation (e.g., Sanders et al. 1988). Our finding of luminous starburst activity in many QSOs is clearly consistent with such an evolutionary link between ULIRGs (which show ultraluminous star formation and frequent coexisting AGN) and QSOs (which show ultraluminous AGN and frequent coexisting

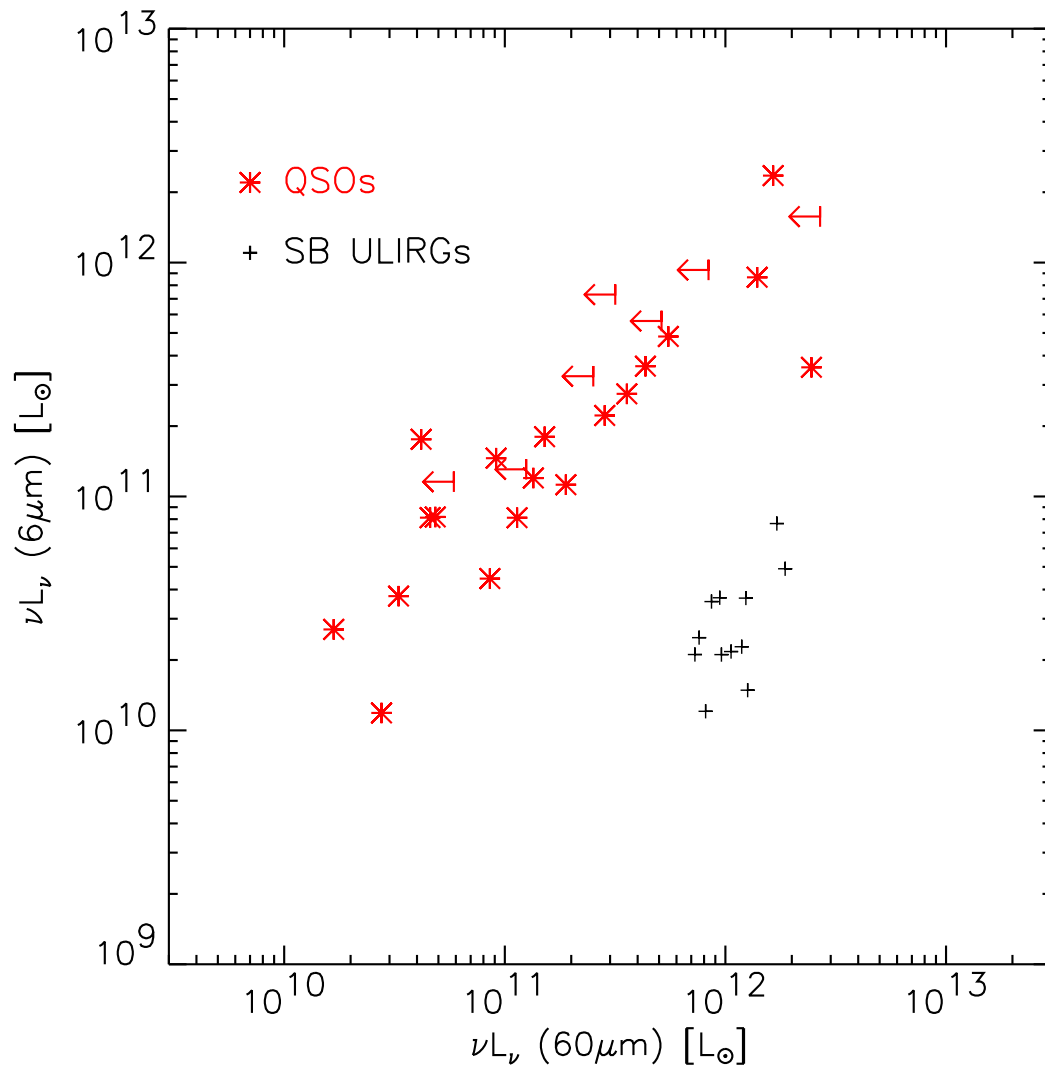


Figure 10.8: Luminosities  $L(6\mu\text{m})$  vs.  $L(60\mu\text{m})$  for the QSOs and for starburst dominated ULIRGs.

starbursts). From such basically energy-related considerations, an evolutionary path with a clear time arrow is, however, difficult to demonstrate and distinguish from more random processes. Including structural and dynamical information, e.g. from other elements of the QUEST program, will better probe this link.

### 10.4.3 Direct AGN Heating of Cold Dust and PAHs ?

Several models have proposed a direct AGN heating of the far-infrared emission of QSOs (e.g., Sanders et al. 1989). A basic feature of such models, needed in order to fit QSO SEDs with moderately strong far-infrared emission, is a significant covering factor by obscuring dust at relatively large (few kpc) distances from the central AGN that is not shadowed by matter closer in. In the model of Sanders et al. (1989), for example, this is accomplished by invoking a dusty galactic disk that is warped into the unshielded AGN radiation on such scales. In such a scenario, the star formation activity and associated PAH emission would be low. The PAH to far-infrared correlation that we find would have to be due to PAH excitation by the AGN itself at this relatively large distance. The required emission is significant - as we argued above, the ratio of PAH and far-infrared is similar to that in starburst-dominated systems, and far-infrared is a significant fraction of the bolometric luminosity for our sample ( $\sim 10\%$  mean for the systems with far-infrared detections).

A main argument against this scenario is the likely destruction mechanism of PAH by AGN radiation: If this process works through destruction by individual EUV and X-ray photons, then the PAH carriers cannot survive at even kpc distances unless shielded by a large column able to stop the deeply penetrating hard photons (Voith 1992). Such a large absorbing column ( $N_{\text{H}} \geq 10^{22} \text{cm}^{-2}$ ) would, however, prevent the heating of a significant far-infrared emitting dust component at large distance, by absorbing the UV ‘big blue bump’ bulk part of the AGN SED. It would also absorb the near-UV ( $< 13.6 \text{eV}$ ) radiation needed to actually excite infrared feature emission from the shielded PAH molecules. As argued by Voit (1992) and Maloney (1999), PAH molecules can survive even relatively close to a powerful AGN if placed behind large obscuration. Such high obscuring columns could be plausibly identified with the anisotropic obscuring structure postulated by unified AGN models. Exciting these surviving PAH molecules will however require a separate near-UV source, for example by reintroducing a circumnuclear starburst. An indirect transport of AGN near-UV radiation to this shielded material, for example by scattering of UV emerging into the AGN ionisation cones, appears unlikely to produce the required large PAH luminosities for  $\sim 1\%$  scattering efficiency, as often assumed on the basis of polarimetric AGN studies (e.g. Pier et al. 1994).

Freudling et al. (2003) and Siebenmorgen et al. (2004b) present observations and models of radio-loud AGN in which they ascribe the full infrared SED including sometimes present PAH emission to the AGN, without invoking additional star formation. Their models (see discussion in Siebenmorgen et al. 2004a) invoke a different treatment of PAH destruction in the AGN radiation field. While this issue certainly deserves future study, their models may underestimate PAH

destruction by the AGN. They predict strong PAH emission from optically thin dust illuminated by an AGN at a typical NLR distance, as well as significant PAH emission from an optically thick model for the central region of a nearby AGN which has most of its mid-infrared emission arising in a compact ( $\sim 10$  pc) region (Fig. 20, 21, 22 of Siebenmorgen et al. 2004a). In contrast, spatially resolved observations put very strong limits on the PAH emission from such regions of some nearby AGN (Le Floc'h et al 2001; Siebenmorgen et al. 2004a; Weedman et al. 2005; Mason et al. 2006).

Our interpretation is also consistent with other, partly circumstantial, evidence for star formation in QSOs. Canalizo & Stockton (2001) find optical spectroscopic evidence for relatively recent  $\leq 300$  Myr star formation in a sample that ranges from ULIRGs to some of the moderately FIR-bright PG QSOs of our sample. Veilleux et al. (2006) find some PG QSOs brighter than the H-band fundamental plane, possibly indicating circumnuclear star formation. Molecular gas detections of PG QSOs (e.g., Evans et al. 2001; Scoville et al. 2003), while not directly probing star formation, suggest sufficient material to power the far-infrared emission if star formation is efficient.

#### 10.4.4 Comparison to QSO Star Formation Estimates Based on [OII]

Our finding that star formation activity is able to power the far-infrared emission is in contrast to the result of Ho (2005). For a PG-based sample partly overlapping with our sample, he found insufficient star formation from an analysis using the [O II]  $\lambda 3727$  line as a star formation tracer. Large and uncertain corrections for extinction of this tracer are likely the main contributor to this discrepancy.

Ho (2005) used [O II]  $\lambda 3727$  fluxes for his QSOs from the literature and the calibration of Kewley et al. (2004) for *extinction-corrected* [O II]  $\lambda 3727$  as a star formation indicator that is also a function of metallicity:  $\text{SFR}([\text{OII}], Z)$ . Kewley et al. (2004) base their work on a sample of nearby field galaxies with detailed integrated optical spectroscopy, and star formation rates spanning 4 orders of magnitude centered on  $\sim 1 M_{\odot} \text{yr}^{-1}$ . They demonstrate that [O II]  $\lambda 3727$  is a star formation indicator as good as  $\text{H}\alpha$  over this range, provided extinction can be corrected for individual objects, and individual metallicities are known.

To apply this calibration to QSOs whose optical spectra are strongly dominated by AGN emission, Ho (2005) made three assumptions: (1) Screen attenuation of  $A_V=1$  towards the star forming regions, (2) metallicity twice solar, (3) one third of the [O II]  $\lambda 3727$  emission comes from star formation. Another implicit assumption is (4) aperture corrections to [O II]  $\lambda 3727$  can be ignored for the hosts of this QSO sample with median  $z \sim 0.09$  observed with  $2 - 5''$  optical spectroscopic apertures. Under these assumptions, Ho (2005) infers star formation rates of at most  $20 M_{\odot} \text{yr}^{-1}$  but often much less, and typically an order of magnitude below those inferred by ascribing the far-infrared emission to star formation.

While all four assumptions contribute to the uncertainties of this approach, we believe that assumption (1) about the reddening to the star forming regions is the key to the systematic difference to our *Spitzer* results. As noted, e.g., by Kewley

(2004), extinction is a strong function of intrinsic [O II]  $\lambda 3727$  luminosity. At the short wavelength of [O II]  $\lambda 3727$  where  $A_\lambda \sim 1.5 \times A_V$ , increased dust extinction can relatively easily offset much of an increase in intrinsic line luminosity. Since the far-infrared luminosities of our quasars reach beyond  $10^{11} L_\odot$ , it is instructive to compare to the systematic optical spectroscopic study of a complete sample of luminous infrared galaxies by Poggianti & Wu (2000), which is addressing objects with  $L_{FIR} \sim 10^{11.5} L_\odot$  for our cosmology. More than half of their objects have so-called e(a) optical spectra, characterized by absorption in the higher Balmer lines, weak [O II]  $\lambda 3727$ , and significant obscuration of the emission lines.  $E(B-V)$  is  $\sim 1.11$  even in the simplifying screen assumption, which still ignores regions in such highly dusty objects that are too obscured to contribute to the optical lines. With observed  $L(H\alpha) \sim 10^{41} \text{erg s}^{-1}$  and [O II]  $\lambda 3727/H\alpha \sim 0.23$ , they are in the regime of or below the portion (1/3) of the QSO [O II]  $\lambda 3727$  luminosities that Ho (2005) ascribes to star formation, already considering that [O II]  $\lambda 3727$  aperture corrections may be more significant for the Poggianti & Wu (2000) sample which has median  $z=0.0324$  and similar spectroscopic apertures. Similar arguments apply, to a lesser degree, to the Poggianti & Wu (2000) objects with spectral classifications other than e(a). There is a large population of dusty luminous starbursts that could fit the weak [O II]  $\lambda 3727$  emission of the Ho (2005) QSOs.

In summary, while the QSO optical data are consistent with the low star-formation rate interpretation of Ho (2005), they are also consistent with much higher star formation rates. This is because the optical analysis of Ho (2005) is based on a single line that is strongly extinction sensitive, and no extinction constraints are available for this component from the optical data. Less extinction sensitive data like the *Spitzer* infrared spectra are needed to break this degeneracy, and suggest more substantial star formation rates. Some of the QSO host optical spectra may share properties of infrared galaxies with e(a) optical spectra: little obscuration towards the stellar continuum spectra dominated by an older post-burst component, but still significant obscuration of the active star forming regions Poggianti & Wu (2000).

### 10.4.5 Implications for High Redshift QSOs

Deep submm and mm photometry has led to the detection of rest frame submm and far-infrared dust emission from radio-quiet QSOs at redshifts up to 6.42 (e.g. Omont et al. 2001; Isaak et al. 2002; Bertoldi et al. 2003). It has been variously argued through indirect arguments like CO content that this emission is star formation powered (e.g. Walter et al. 2003), implying that these QSOs coexist with extremely powerful  $\geq 10^{13} L_\odot$  starbursts. Our results support a starburst origin of QSO far-infrared emission, but do not extend to this luminosity and redshift regime. If the ratio of PAH to far-infrared emission for these QSOs is similar to the one in the local QSOs and in ULIRGs, detection of PAH emission on top of a strong continuum may be within reach of *Spitzer* spectroscopy. PAH emission from similar luminosity SMGs is detectable at ULIRG-like ratios to the far-infrared emission (Lutz et al. 2005). Luminous PAH emission has also been reported in mid-infrared selected samples of  $z \sim 2$  infrared galaxies (Yan et

al. 2005). Probing for PAH emission may currently be the only way to verify the assumption of simultaneous strong star formation and QSO activity in high redshift QSOs.

## 10.5 Conclusions

Sensitive *Spitzer* mid-infrared spectroscopy reveals the widespread presence of aromatic ‘PAH’ emission features in  $z \leq 0.3$  QSOs from the Palomar-Green sample, indicating the presence of powerful ( $\nu L_\nu(60\mu\text{m}) \sim 1.7 \times 10^{10}$  to  $2.5 \times 10^{12} L_\odot$ ) star formation activity in these systems. Starburst and AGN activity are connected in QSOs up to these high luminosities. By comparing the ratios of PAH  $7.7\mu\text{m}$ , [Ne II]  $12.8\mu\text{m}$ , and far-infrared emission in QSOs with starbursts we conclude that for the average QSO in our sample at least 30% and likely most of the QSO far-infrared emission is due to star formation. The data suggest a trend with the star formation contribution being the largest in the most FIR-luminous QSOs.

Acknowledgements: We thank Aprajita Verma, Natascha Förster Schreiber and Helene Roussel for help with comparison starburst data. We are grateful for comments by the referee.

This work is based on observations carried out with the Spitzer Space Telescope, which is operated by the Jet Propulsion Laboratory, California Institute of Technology, under NASA contract 1407. Support for this work was provided by NASA through contract 1263752 (S.V.) issued by JPL/Caltech. The authors wish to recognize the very significant cultural role that Theresienwiese has always had with the indigenous Bavarian community.

HN acknowledges a Humboldt Foundation prize and thanks the host institution, MPE Garching, where this work has been done. AJB acknowledges support from the National Radio Astronomy Observatory, which is operated by Associated Universities, Inc., under cooperative agreement with the National Science Foundation.



# Chapter 11

## Conclusions

The first part of this work introduced the Far-Infrared Field Imaging Line Spectrometer (FIFI-LS). The optical design of the internal calibration source (for internal flat fielding) was presented. Its design parameters were selected such that the expected background level produced by the relative warm telescope (with an assumed emissivity of 15%) is reproduced.

Another goal of this thesis was the optical alignment of the long wavelength channel of FIFI-LS. This has been achieved with a precision of a few percent of the beam diameter throughout the optical path.

In addition the optical design of a telescope simulator was performed in the context of this thesis. This instrument allows one to test the spectral and imaging properties of FIFI-LS in the FIR. Performing measurements with the telescope simulator we found a good agreement between the expected and measured properties of FIFI-LS. Using the telescope simulator we measured the spatial resolution of FIFI-LS by scanning a FIR point source through the field of view. In addition a gas-cell (filled with air or CO) has been used to measure the spectral resolution and calibrate the wavelength scale of FIFI-LS.

- For the FWHM of the PSF we found  $\text{FWHM}_x \sim 4.3$  mm and  $\text{FWHM}_y \sim 3.7$  mm in the detector plane of FIFI-LS while the calculated values are  $\text{FWHM}_x \sim 4.9$  mm and  $\text{FWHM}_y \sim 4.5$  mm. The small deviations may be explained by the error within the magnification factor (between the focal plane of FIFI-LS and telescope simulator), a somewhat different diffraction situation within the simulator compared to the SOFIA telescope, and a slightly smaller effective pixel size caused by the behavior of the light-cones located in front of each pixel. Also a slightly different wavelength, due to a small deviation from the center position of the grating, may contribute to the deviation between measurement and calculation.
- Using the gas-cell (filled with laboratory air), we achieved a spectral calibration of FIFI-LS. Multiple water lines were identified from the measured line pattern and used for the calibration. To perform the calibration, we fitted the measured grating positions for the centroids of the lines to their theoretical wavelengths using the grating equation and a consistent set of fit parameters. As fit parameters, we assumed a variable grating period  $g'$

in mm/groove to account for the thermal contraction of the grating. Due to the uncalibrated offset of the grating position readout a constant angle offset  $\alpha$  from the actual measured position is also considered. The final calibration was successfully achieved with  $g' = 0.117$  mm and  $\alpha = 20.957^\circ$ .

- To determine the spectral resolution of FIFI-LS the CO line at  $163 \mu\text{m}$  (J=16-15) at a gas pressure of about 20 mbar was measured. The FWHM of the CO line has been measured to  $\sim 0.136 \mu\text{m}$ . This corresponds to a resolution of  $R = 1200$  which agrees quite well with the calculated resolution of  $R = 1268$ .

The second part of this thesis presented the investigation of active galaxies with the Infrared Spectrograph (IRS) on board of the Spitzer Space Telescope. In summary our main findings are:

Silicate emission can be strong in low luminosity AGN which counters suggestions that silicate emissions are present only in the most luminous AGN. The silicate dust properties we investigated in the LINER (NGC 3998) are inconsistent with the standard ISM dust emission and may be explained by dust processing within the AGN environment. We investigated the origin of the silicate dust emission in a sample of 23 local PG QSOs using a template fitting program developed in the context of this thesis. We found that the silicate dust emission is fully consistent with a cool emission ( $T \sim 200\text{K}$ ) originating from the NLR with distances up to 260 pc to the central source. This is large compared to expectations for an origin within the torus ( $\sim 1\text{pc}$ ). From a further investigation of the PG QSOs we found that for the average QSO in our sample at least 30% and likely most of the QSO far-infrared emission is due to star formation. In addition we found that AGN and starburst activity are connected in PG QSOs pointing to a common feeding mechanism for the AGN and the star formation.

In more detail the conclusions are :

### 1. The first detection of silicate dust emission in a LINER (NGC 3998)

In the unifying scheme for AGN it is postulated that an “obscuring torus” usually surrounds the accreting massive black hole. In particular, the tori are predicted to exhibit prominent silicate dust features in either absorption or emission, depending on whether an AGN is viewed with the torus edge-on (Type 2) or face-on (Type 1).

Here we reported on the first detection of  $\sim 10$  and  $\sim 18 \mu\text{m}$  silicate dust emission features in a low-luminosity active galactic nucleus (AGN) of the Type 1 LINER galaxy NGC 3998. Silicate emissions in AGN have only recently been detected in several quasars. Our detection counters suggestions that silicate emissions are present only in the most luminous AGN. Silicate emission can be equally strong in low luminosity AGN. By comparing the continuum subtracted spectra of NGC 3998 and the QSO 3C273 (from Hao et al. (2005)) we found that without any further scaling the two spectra are virtually identical in the  $10 \mu\text{m}$  feature, but at wavelengths  $> 20 \mu\text{m}$  they

deviate significantly from each other. We have also compared NGC 3998 to the standard ISM emission of amorphous silicates, olivines of larger grain size and a Herbig Be star (HD163296) spectrum. In general we found that the  $10\ \mu\text{m}$  feature in NGC 3998 cannot be fitted with any of these templates since its peak emission is shifted towards longer wavelengths. In addition is the  $10\ \mu\text{m}$  feature of the standard ISM emission to narrow to fit the dust emission in NGC 3998. We have tried to fit the continuum subtracted spectrum of NGC 3998 with the product of a black body and the ISM silicate opacity's (optical thin dust emission). We found that while the relative intensities of the 10/18 peaks in NGC 3998 can be reproduced by such a fit with a temperature of  $\sim 180\text{K}$ , the emission in the blue wing of the  $10\ \mu\text{m}$  feature and longwards of  $\sim 20\ \mu\text{m}$  is significantly over-predicted. We conclude that, due to dust processing, the dust giving rise to the emission features in NGC 3998 may deviate from pristine galactic ISM dust. The case of NGC 3998 with its low AGN luminosity and different SED shape at longer wavelengths compared to QSOs may place important new constraints on the three-dimensional radiative transfer models of AGN emission.

## 2. The origin of the silicate dust emission in PG QSOs

Scenarios based on the unified model suggest that silicate emission in AGN arises mainly from the illuminated faces of the clouds in the torus at temperatures near sublimation. However, detections of silicate emission in Type 2 QSOs, and the estimated cool dust temperatures (see also Sturm et al. 2005), argue for an origin in a more extended region. To investigate this issue, we have presented the *Spitzer*-IRS spectra of 23 QSOs. We have matched physically-based models to the mid-infrared spectra and found that the silicate emission observed in these objects can be reproduced by emission from clouds, outside the central torus. This extended silicate-emitting region is possibly associated with the innermost NLR region or the intermediate dusty region proposed by Netzer & Laor (1993). The dust cloud distances found here scale with the AGN luminosity as  $R_{dust} \sim 80 \cdot L_{bol46}^{0.5}$  pc, with the bolometric luminosity  $L_{bol46}$  given in units of  $10^{46}\ \text{ergs}^{-1}$ . We have estimated the median distance of the dust cloud responsible for the silicate emission to be 40 pc, while for individual sources distances up to 260 pc are possible. The smallest cloud distance is 9 pc for PG 0050+124. The calculated covering factors for the dust clouds have a median of 0.16 and are in agreement with an NLR origin of the silicate emission. Our models do not exclude the possibility of a torus contribution to the observed silicate emission, but rather emphasize the good agreement and perhaps the necessity of a larger-scale contribution to this emission. Finally, future high spatial resolution infrared observations and further crosschecks including the comparison to Type 1/2 ratios as well as distributions and individual values for the obscuring columns in X-rays and the near infrared are needed to resolve the remaining ambiguities between torus and NLR emission.

### 3. The origin of the FIR emission in PG QSOs

We presented the detection of aromatic ‘PAH’ emission features in  $z \leq 0.3$  QSOs from the Palomar-Green sample, indicating the presence of powerful ( $\nu L_\nu(60\mu\text{m}) \sim 1.7 \times 10^{10}$  to  $2.5 \times 10^{12} L_\odot$ ) star formation activity in these systems. We found that starburst and AGN activity are connected in QSOs up to these high luminosities. By comparing the ratios of PAH  $7.7\mu\text{m}$ , [Ne II]  $12.8\mu\text{m}$ , and far-infrared emission in QSOs with starbursts we conclude that for the average QSO in our sample at least 30% and likely most of the QSO far-infrared emission is due to star formation. The data suggest a trend with the star formation contribution being the largest in the most FIR-luminous QSOs. By subtracting a starburst spectrum (e.g. M82) from our average QSO spectrum (with strong PAH emission) we found that silicate emission in the spectrum can be masked by the admixture of PAH emission from star forming regions. Thus the investigation of silicate emission requires a careful decomposition technique like presented in Chapter 9.

# Acknowledgements

Firstly, I am very grateful to Prof. Reinhard Genzel for the opportunity to prepare my thesis in his wonderful group and for his friendly support. I would also like to thank my supervisors Dr. Dieter Lutz, Dr. Albrecht Poglitsch and Dr. Eckhard Sturm for the really great support they have given to me. It has been a pleasure to learn from their great experience and it has also been a big pleasure to travel together (e.g. to Cologne, Berlin, Xi'an) where we had a lot of fun. I also would like to thank Prof. Hagai Netzer for his very pleasant and fruitful cooperation and Prof. Sylvain Veilleux for the productive discussions we had in our innumerable video conferences.

Especially I would like to thank Dr. Leslie Looney, Katie Dodds-Eden, Dr. Rene Fassbender and Dr. Giovanni Cresci for their big help with corrections.

Many thanks also ...

to all the current and past members of the QUEST collaboration, for a great and productive time. To Dr. Walfried Raab for many illuminating discussions about physics and life. To Dr. Norbert Geis for sharing his optical expertise and his deep insight into ZEMAX. To those who supported the management of my thesis, namely Dr. Linda Tacconi and Susanne Harai-Ströbel. To Dr. Thomas Ott for his support with computer problems. To the workshop and especially to Armin Goldbrunner and Heinz Dohnalek for their great support with the design and fabrication of hardware parts. To Francisco Müller-Sanchez, Yohei Harayama and Katie Dodds-Eden for being wonderful office mates. To Peter Buschkamp, Alessandra Contursi, Giovanni Cresci, Rene Fassbender, Natascha M. Förster Schreiber, Fabio Fumi, Stefan Gillessen, Rainer Hönle, Sebastian Rabien, Sascha Trippe and Elisabetta Valiante for their friendship and many joyful hours. To the PACS group for the funny coffee sessions. To all the other members of the IR group for sharing their expertise and for the pleasant atmosphere.

And finally but not least to my mother, for all her love, support, and encouragement and to Michaela for her loving support during hard times.



# Bibliography

- Akritas, M.G., Siebert, J. 1996, MNRAS, 278, 919
- Alexander, T., Sturm, E., Lutz, D., Sternberg, A., Netzer, H., Genzel, R. 1999, ApJ, 512, 204
- Armus, L., et al. 2004, ApJS, 154, 178
- Armus, L., et al. 2006, ApJ, 640, 204
- Antonucci, R. 1993, ARA&A, 31, 473
- Asplund, M., Grevesse, N., & Sauval, A. J. 2005, Cosmic Abundances as Records of Stellar Evolution and Nucleosynthesis, 336, 25
- Barvainis, R. 1987, ApJ, 320, 537
- Barvainis, R. 1992, ApJ, 400, 502
- Baskin, A., Laor, A. 2005, MNRAs, 358, 1043
- Bennert, N., Falcke, H., Schulz, H., Wilson, A. S., & Wills, B. J. 2002, ApJL, 574, L105
- Bertoldi, F., Carilli, C.L., Cox, P., Fan, X., Strauss, M.A., Beelen, A., Omont, A., Zylka, R. 2003, AAP, 406, L55
- Bock, J. J., Marsh, K. A., Ressler, M. E., & Werner, M. W. 1998, ApJL, 504, L5
- Bock, J.J., et al. 2000 AJ, 120, 2904
- Boroson, T.A., Green, R.F. 1992, APJS, 80, 109
- Calzetti, D., et al. 2005, ApJ, 633, 871
- Cameron, M., Storey, J. W. V., Rotaciuc, V., Genzel, R., Verstraete, L., Drapatz, S., Siebenmorgen, R., & Lee, T. J. 1993, ApJ, 419, 136
- Canalizo, G., Stockton, A., 2001, ApJ, 555, 719
- Chary, R., Elbaz, D. 2001, ApJ, 556, 562
- Chini, R., Kreysa, E., Biermann, P.L., 1989, AAP, 219, 87

- Clavel, J., et al. 2000, *A&A*, 357, 839
- Cresci, G., Maiolino, R., Marconi, A., Mannucci, F., Granato, G.L. 2004, *AAP*, 423, L13
- Dale, D.A., Helou, G., Contursi, A., Silbermann, N.A., Kolhatkar, S. 2001, *ApJ*, 549, 215
- Dasyra, K.M., et al. 2006a, *ApJ*, 638, 745
- Dasyra, K.M., et al. 2006b, *ApJ*, 651, 835D
- Davies, R.I., Tacconi, L.J., Genzel, R. 2001, *ApJ*, 602, 148
- Davies, R.I., Tacconi, L.J., Genzel, R. 2001, *ApJ*, 613, 781
- Draine, B. T. & Li, H.M. 1984, *ApJ*, 285, 89
- Draine, B. T. 2003, *ARAA*, 41, 241
- Draine, B. T., & Li, A. 2007, *ApJ*, 657, 810
- Dullemond, C.P., van Bemmell, I. 2005, *AAP*, 436, 47
- Efstathiou, A., & Rowan-Robinson, M. 1995, *MNRAS*, 273, 649
- Efstathiou, A. 2006, *MNRAS*, 371, L70
- Elitzur, M., & Shlosman, I. 2006, *ApJL*, 648, L101
- Elvis, M., et al. 1994, *APJS*, 95, 1
- Elvis, M. 2000, *ApJ*, 545, 63
- Engelbracht, C.W., Gordon, K.D., Rieke, G.H., Werner, M.W., Dale, D.A., Latter, W.B. 2005, *ApJ*, 628, L29
- Evans, A.S., Frayer, D.T., Surace, J.A., Sanders, D.B. 2001, *AJ*, 121, 3286
- Fabbiano, G., Fassnacht, C., & Trinchieri, G. 1994, *ApJ*, 434, 67
- Förster Schreiber, N.M., Roussel, H., Sauvage, M., Charmandaris, V. 2004, *AAP*, 419, 510
- Freudling, W., Siebenmorgen, R., Haas, M. 2003, *ApJ*, 599, L13
- Fritz, J., et al. 2006, *MNRAS*, 366, 767
- Genzel, R., et al. 1998, *ApJ*, 498, 579
- Genzel, R., Cesarsky, C. J. 2000, *ARAA*, 38, 761
- Gonzalez-Delgado, R.M., Heckman, T., Leitherer, C. 2001, *ApJ*, 546, 845
- Granato, G.L., Danese, L., 1994, *MNRAS*, 268, 235

- Granato, G.L., Danese, L., Franceschini, A. 1997, *ApJ*, 486, 147
- Groves, B. A., Dopita, M. A., & Sutherland, R. S. 2004, *ApJS*, 153, 75
- Groves, B., et al. 2006, *AA*, 458, 405
- Guyon, O. 2002, PhD Thesis, Univ. Paris VI
- Guyon, O., Sanders, D.B., Stockton, A. 2006, *ApJS*, 166, 89G
- Haas, M., Chini, R., Meisenheimer, K., Stickel, M., Lemke, D., Klaas, U., Kreysa, E. 1998, *ApJ*, 503, L109
- Haas, M., Müller, S.A.H., Chini, R., Meisenheimer, K., Klaas, U., Lemke, D., Kreysa, E., Camenzind, M. 2000, *AAP*, 354, 452
- Haas, M., et al. 2003, *AAP*, 402, 87
- Haas, M., Siebenmorgen, R., Schulz, B., Krügel, E., Chini, R. 2005, *AAP*, 442, L39
- Hao, L., et al. 2005, *ApJ*, 625, L75
- Heckman, T., Gonzalez-Delgado, R., Leitherer, C., Meurer, G.R., Krolik, J., Wilson, A.S., Koratkar, A., Kinney, A. 1997, *ApJ*, 482, 114
- Higdon, S.J.U., et al. 2004, *PASP*, 116, 975
- Hönig, S. F., Beckert, T., Ohnaka, K., & Weigelt, G. 2006, *AAP*, 452, 459
- Ho, L. C., Filippenko, A. V., Sargent, W. L. W., & Peng, C. Y. 1997, *ApJS*, 112, 391
- Ho, L. 2005, *ApJ*, 629, 680
- Houck, J.R., et al. 2004, *ApJs*, 154, 18
- Hughes, D.H., Robson, E.I., Dunlop, J.S., Gear, W.K. 1993, *MNRAS*, 263, 607
- Imanishi, M. 2003, *ApJ*, 599, 918
- Isaak, K.G., Priddey, R.S., McMahon, R.G., Omont, A., Peroux, C., Sharp, R.G., Withington, S. 2002, *MNRAS*, 329, 149
- Jester, S., et al. 2005, *AJ*, 130, 873
- Kaspi, S., et al. 2005, *ApJ*, 629, 61
- Kauffmann, G., et al. 2003, *MNRAS*, 346, 1055
- Kemper, F., Vriend, W. J., & Tielens, A. G. G. M. 2004, *ApJ*, 609, 826
- Kewley, L.J., Geller, M.J., Jansen, R.A. 2004, *AJ*, 127, 2002

- Kimura, H., Mann, I., Biesecker, D. A., & Jessberger, E. K. 2002, *Icarus*, 159, 529
- Kimura, H., Mann, I., & Jessberger, E. K. 2003, *ApJ*, 583, 314
- Klaas, U., et al., 2001, *AAP*, 379, 823
- Koenigl, A., Kartje, J.F. 1994, *ApJ*, 434, 446
- Kriss, G.A., et al. 1992, *BAAS*, 24, 751
- Jaffe, W., et al. 2004, *nature*, 429, 47
- Jester, S., et al. 2005, *AJ*, 130, 873 Jansen, R.A. 2004, *AJ*, 127, 2002
- Laor, A., & Draine, B. T. 1993, *ApJ*, 402, 441
- Laurent, O., Mirabel, I.F., Charmandaris, V., Gallais, P., Madden, S.C., Sauvage, M., Vigroux, L., Cesarsky, C. 2000, *AAP*, 359, 887
- Le Floch, E., Mirabel, I.F., Laurent, O., Charmandaris, V., Gallais, P., Sauvage, M., Vigroux, L., Cesarsky, C. 2001, *AAP*, 367, 487
- Lu, N., et al., 2003, *APJ*, 588, 199
- Lutz, D., Maiolino, R., Moorwood, A.F.M., Netzer, H., Wagner, S.J., Sturm, E., Genzel, R., 2002, *AAP*, 396, 439
- Lutz, D., Sturm, E., Genzel, R., Spoon, H.W.W., Moorwood, A.F.M., Netzer, H., Sternberg, A. 2003, *AAP*, 409, 867
- Lutz, D., Maiolino, R., Spoon, H. W. W., & Moorwood, A. F. M. 2004, *AAP*, 418, 465
- Lutz, D., Valiante, E., Sturm, E., Genzel, R., Tacconi, L.J., Lehnert, M.D., Sternberg, A., Baker, A.J. 2005, *ApJ*, 625, L83
- Maiolino, R., Marconi, A., Salvati, M., Risaliti, G., Severgnini, P., Oliva, E., La Franca, F., & Vanzi, L. 2001a, *AAP*, 365, 28
- Maiolino, R., Marconi, A., & Oliva, E. 2001b, *AAP*, 365, 37
- Maloney, P. 1999, *APSS*, 266, 207
- Maoz, D., Nagar, N. M., Falcke, H., & Wilson, A. S. 2005, *APJ*, 625, 699
- Marshall, J.A. 2007, *ApJ*, 670, 129M
- Mason, R.E., Geballe, T.R., Packham, C., Levenson, N.A., Elitzur, M., Fisher, R.S., Perlman, E. 2006, *ApJ*, 640, 612
- Mattila, K., Lemke, D., Haikala, L.K., Laureijs, R.J., Leger, A., Lehtinen, K., Leinert, C., Mezger, P.G. 1996, *AAP*, 315, L353

- Mattila, K., Lehtinen, K., Lemke, D., 1999, *AAP*, 342, 643
- Meeus, G., Waters, L. B. F. M., Bouwman, J., van den Ancker, M. E., Waelkens, C., & Malfait, K. 2001, *AAP*, 365, 476
- Nenkova, M., Ivezić, Ž., & Elitzur, M. 2002, *ApJL*, 570, L9
- Netzer, H., & Laor, A. 1993, *ApJL*, 404, L51
- Netzer, H., Shemmer, O., Maiolino, R., Oliva, E., Croom, S., Corbett, E., & di Fabrizio, L. 2004, *ApJ*, 614, 558
- Netzer, H., et al. 2006, *AAP*, 453, 525N
- Netzer, H., et al. 2007, *ApJ*, 666, 806N
- Neugebauer G., Miley, G.K., Soifer, B.T., Clegg, P.E. 1986, *ApJ*, 308, 815
- Norman, C., Scoville, N.Z. 1988, *ApJ*, 322, 124
- Oliva, E., Origlia, L., Maiolino, R., Moorwood, A.F.M., 1999, *AAP*, 350, 9
- Omont, A., Cox, P., Bertoldi, F., McMahon, R.G., Carilli, C., Isaak, K.G. 2001, *AAP*, 374, 371
- Packham, C., Radomski, J. T., Roche, P. F., Aitken, D. K., Perlman, E., Alonso-Herrero, A., Colina, L., & Telesco, C. M. 2005, *ApJL*, 618, L17
- Pier, E.A., Krolik, J.H. 1992, *ApJ*, 401, 99
- Pier, E.A., Antonucci, R., Hurt, T., Kriss, G., Krolik, J. 1994, *ApJ*, 428, 124
- Poggianti, B.M., Wu, H. 2000, *ApJ*, 529, 157
- Ptak, A., Terashima, Y., Ho, L.C., and Quataert, E. 2004, *ApJ*, 606, 173
- Raab, W. 2002, PhD-thesis, Ludwig-Maximilians-Universität, München
- Radomski, J. T., Piña, R. K., Packham, C., Telesco, C. M., De Buizer, J. M., Fisher, R. S., & Robinson, A. 2003, *ApJ*, 587, 117
- Risaliti, G., Maiolino, R., Salvati, M. 1999, *ApJ*, 522, 157
- Roche, P.F., Aitken, D.K., Smith, C.H., Ward, M.J. 1991, *MNRAS*, 248, 606
- Rowan-Robinson, M. 1995, *MNRAS*, 272, 737
- Sanders, D.B., Soifer, B.T., Elias, J.H., Madore, B.F., Matthews, K., Neugebauer, G., Scoville, N.Z. 1988, *ApJ*, 325, 74
- Sanders, D.B., Phinney, E.S., Neugebauer, G., Soifer, B.T., Matthews, K. 1989, *ApJ*, 347, 29
- Sanders, D.B., Mirabel, I.F. 1996, *ARAA*, 34, 749

- Schmidt, M., Green, R.F. 1983, *ApJ*, 269, 353
- Schweitzer, M. et al., 2006, *ApJ*, 649, 79
- Scoville, N.Z., Frayer, D.T., Schinnerer, E., Christopher, M. 2003, *ApJ*, 585, L105
- Siebenmorgen, R., Krügel, E., Spoon, H.W.W. 2004a, *AAP*, 414, 123
- Siebenmorgen, R., Freudling, W., Krügel, E., Haas, M. 2004b, *AAP*, 421, 129
- Siebenmorgen, R., Haas, M., Krügel, E., Schulz, B. 2005, *AAP*, 436, L5
- Siebenmorgen, R., & Efstathiou, A. 2005, *The Spectral Energy Distributions of Gas-Rich Galaxies: Confronting Models with Data*, 761, 245
- Siebenmorgen, R., et al. 2005, *astro-ph/0504263*
- Siegel, R., et al. 2002, *Wärmeübertragung durch Strahlung*, ISBN-10 3540527109, Springer Verlag, Berlin
- Spinoglio, L., Malkan, M.A. 1992, *ApJ*, 399, 504
- Spoon, H.W.W., Moorwood, A.F.M., Lutz, D., Tielens, A.G.G.M., Siebenmorgen, R., Keane, J.V. 2004a, *AAP*, 414, 873
- Spoon, H.W.W., et al. 2004b, *ApJS*, 154, 184
- Sturm, E., Lutz, D., Tran, D., Feuchtgruber, H., Genzel, R., Kunze, D., Moorwood, A.F.M., Thornley, M.D. 2000, *AAP*, 358, 481
- Sturm, E., Lutz, D., Verma, A., Netzer, H., Sternberg, A., Moorwood, A.F.M., Oliva, E., Genzel, R. 2002, *AAP*, 393, 821 (S02)
- Sturm, E., et al. 2005, *AAP*, 629, L21
- Sturm, E., et al. 2006, *APJ*, 642, 8
- Thornley, M.D., Förster Schreiber, N., Lutz, D., Genzel, R., Spoon, H.W.W., Kunze, D., Sternberg, A. 2000, *ApJ*, 539, 641
- Teplitz, H.I., et al. 2006, *ApJ*, 638, L1
- Tomono, D., Doi, Y., Usuda, T., & Nishimura, T. 2001, *ApJ*, 557, 637
- Tonry, J. L., Dressler, A., Blakeslee, J. P., Ajhar, E. A., Fletcher, A. B., Luppino, G. A., Metzger, M. R., & Moore, C. B. 2001, *ApJ*, 546, 681
- van Boekel et al. 2005, *A&A*, 437, 189V
- Veilleux, S., Goodrich, R.W., Hill, G.J. 1997, *ApJ*, 477, 631
- Veilleux, S. 2004, in *Proceedings of the Guillermo Haro Conference 2003, Multi-wavelength AGN surveys*, ed. R. Mújica & R. Maiolino, World Scientific, 205

- Veilleux, S., et al. 2006, APJ, 643, 707V
- Verma, A., Lutz, D., Sturm, E., Sternberg, A., Genzel, R., Vacca, W. 2003, AAP, 403, 829
- Verma, A., Chramandaris, V., Klaas, U., Lutz, D., Haas, M. 2005, Space Sci. Rev., 119, 355
- Verstraete, L., Puget, J.L., Falgarone, E., Drapatz, S., Wright, C.M., Timmermann, R. 1996, AAP, 315, L337
- Voit, G.M. 1992, MNRAS, 258, 841
- Walter, F., et al. 2003, Nature, 424, 406
- Weedman, D., et al. 2005, ApJ, 633, 706
- Werner, M. W., et al. 2004, APJS, 154, 1
- Weingartner, J.C. & Draine, B.T. 2001, ApJ, 548, 296
- Wooden, D. H., Harker, D. E., Woodward, C. E., Butner, H. M., Koike, C., Witteborn, F. C., & McMurtry, C. W. 1999, ApJ, 517, 1034
- Yan, L., et al. 2005, ApJ, 628, 604